NASA Reference Publication 1376
Volume III

Clouds and the Earth's Radiant Energy System (CERES) Algorithm Theoretical Basis Document

Volume III—Cloud Analyses and Determination of Improved Top of Atmosphere Fluxes (Subsystem 4)

CERES Science Team
Langley Research Center • Hampton, Virginia

National Aeronautics and Space Administration
Langley Research Center • Hampton, Virginia 23681-0001

December 1995

Available electronically at the following URL address: http://techreports.larc.nasa.gov/ltrs/ltrs.html

Printed copies available from the following:

NASA Center for AeroSpace Information
800 Elkridge Landing Road
Linthicum Heights, MD 21090-2934
(301) 621-0390

National Technical Information Service (NTIS)
5285 Port Royal Road
Springfield, VA 22161-2171
(703) 487-4650

Contents

Preface

The Release-1 CERES Algorithm Theoretical Basis Document (ATBD) is a compilation of the techniques and processes that constitute the prototype data analysis scheme for the Clouds and the Earth's Radiant Energy System (CERES), a key component of NASA's Mission to Planet Earth. The scientific bases for this project and the methodologies used in the data analysis system are also explained in the ATBD. The CERES ATBD comprises 11 subsystems of various sizes and complexities. The ATBD for each subsystem has been reviewed by three or four independently selected university, NASA, and NOAA scientists. In addition to the written reviews, each subsystem ATBD was reviewed during oral presentations given to a six-member scientific peer review panel at Goddard Space Flight Center during May 1994. Both sets of reviews, oral and written, determined that the CERES ATBD was sufficiently mature for use in providing archived Earth Observing System (EOS) data products. The CERES Science Team completed revisions of the ATBD to satisfy all reviewer comments. Because the Release-1 CERES ATBD will serve as the reference for all of the initial CERES data analysis algorithms and product generation, it is published here as a NASA Reference Publication.

Due to its extreme length, this NASA Reference Publication comprises four volumes that divide the CERES ATBD at natural break points between particular subsystems. These four volumes are

I: Overviews
- CERES Algorithm Overview
- Subsystem 0. CERES Data Processing System Objectives and Architecture

II: Geolocation, Calibration, and ERBE-Like Analyses
- Subsystem 1.0. Instrument Geolocate and Calibrate Earth Radiances
- Subsystem 2.0. ERBE-Like Inversion to Instantaneous TOA and Surface Fluxes
- Subsystem 3.0. ERBE-Like Averaging to Monthly TOA

III: Cloud Analyses and Determination of Improved Top of Atmosphere Fluxes
- Subsystem 4.0. Overview of Cloud Retrieval and Radiative Flux Inversion
- Subsystem 4.1. Imager Clear-Sky Determination and Cloud Detection
- Subsystem 4.2. Imager Cloud Height Determination
- Subsystem 4.3. Cloud Optical Property Retrieval
- Subsystem 4.4. Convolution of Imager Cloud Properties With CERES Footprint Point Spread Function
- Subsystem 4.5. CERES Inversion to Instantaneous TOA Fluxes
- Subsystem 4.6. Empirical Estimates of Shortwave and Longwave Surface Radiation Budget Involving CERES Measurements

IV: Determination of Surface and Atmosphere Fluxes and Temporally and Spatially Averaged Products
- Subsystem 5.0. Compute Surface and Atmospheric Fluxes
- Subsystem 6.0. Grid Single Satellite Fluxes and Clouds and Compute Spatial Averages
- Subsystem 7.0. Time Interpolation and Synoptic Flux Computation for Single and Multiple Satellites
- Subsystem 8.0. Monthly Regional, Zonal, and Global Radiation Fluxes and Cloud Properties
- Subsystem 9.0. Grid TOA and Surface Fluxes for Instantaneous Surface Product
- Subsystem 10.0. Monthly Regional TOA and Surface Radiation Budget
- Subsystem 11.0. Update Clear Reflectance, Temperature History (CHR)
- Subsystem 12.0. Regrid Humidity and Temperature Fields

The CERES Science Team serves as the editor for the entire document. A complete list of Science Team members is given below. Different groups of individuals prepared the various subsections that constitute the CERES ATBD. Thus, references to a particular subsection of the ATBD should specify

the subsection number, authors, and page numbers. Questions regarding the content of a given subsection should be directed to the appropriate first or second author. No attempt was made to make the overall document stylistically consistent.

The CERES Science Team is an international group led by 2 principal investigators and 19 coinvestigators. The team members and their institutions are listed below.

CERES Science Team

Bruce A. Wielicki, Interdisciplinary Principal Investigator
Bruce R. Barkstrom, Instrument Principal Investigator

Atmospheric Sciences Division
NASA Langley Research Center
Hampton, Virginia 23681-0001

Coinvestigators

Bryan A. Baum
Atmospheric Sciences Division
NASA Langley Research Center
Hampton, Virginia 23681-0001

Maurice Blackmon
Climate Research Division
NOAA Research Laboratory
Boulder, Colorado 80303

Robert D. Cess
Institute for Terrestrial & Planetary Atmospheres
Marine Sciences Research Center
State University of New York
Stony Brook, New York 11794-5000

Thomas P. Charlock
Atmospheric Sciences Division
NASA Langley Research Division
Hampton, Virginia 23681-0001

James A. Coakley
Oregon State University
Department of Atmospheric Sciences
Corvallis, Oregon 97331-2209

Dominique A. Crommelynck
Institute Royal Meteorologique
B-1180 Bruxelles
Belgium

Richard N. Green
Atmospheric Sciences Division
NASA Langley Research Center
Hampton, Virginia 23681-0001

Robert Kandel
Laboratoire de Meteorologie Dynamique
Ecole Polytechnique
91128 Palaiseau
France

Michael D. King
Goddard Space Flight Center
Greenbelt, Maryland 20771

Robert B. Lee III
Atmospheric Sciences Division
NASA Langley Research Center
Hampton, Virginia 23681-0001

A. James Miller
NOAA/NWS
5200 Auth Road
Camp Springs, Maryland 20233

Patrick Minnis
Atmospheric Sciences Division
NASA Langley Research Center
Hampton, Virginia 23681-0001

Veerabhadran Ramanathan
Scripps Institution of Oceanography
University of California-San Diego
La Jolla, California 92093-0239

David R. Randall
Colorado State University
Department of Atmospheric Science
Foothills Campus, Laporte Avenue
Fort Collins, Colorado 80523

G. Louis Smith
Atmospheric Sciences Division
NASA Langley Research Center
Hampton, Virginia 23681-0001

Larry L. Stowe
NOAA/NWS
5200 Auth Road
Camp Springs, Maryland 20233

Ronald M. Welch
South Dakota School of Mines and Technology
Institute of Atmospheric Sciences
Rapid City, South Dakota 57701-3995

Nomenclature

Acronyms

ADEOS	Advanced Earth Observing System
ADM	Angular Distribution Model
AIRS	Atmospheric Infrared Sounder (EOS-AM)
AMSU	Advanced Microwave Sounding Unit (EOS-PM)
APD	Aerosol Profile Data
APID	Application Identifier
ARESE	ARM Enhanced Shortwave Experiment
ARM	Atmospheric Radiation Measurement
ASOS	Automated Surface Observing Sites
ASTER	Advanced Spaceborne Thermal Emission and Reflection Radiometer
ASTEX	Atlantic Stratocumulus Transition Experiment
ASTR	Atmospheric Structures
ATBD	Algorithm Theoretical Basis Document
AVG	Monthly Regional, Average Radiative Fluxes and Clouds (CERES Archival Data Product)
AVHRR	Advanced Very High Resolution Radiometer
BDS	Bidirectional Scan (CERES Archival Data Product)
BRIE	Best Regional Integral Estimate
BSRN	Baseline Surface Radiation Network
BTD	Brightness Temperature Difference(s)
CCD	Charge Coupled Device
CCSDS	Consultative Committee for Space Data Systems
CEPEX	Central Equatorial Pacific Experiment
CERES	Clouds and the Earth’s Radiant Energy System
CID	Cloud Imager Data
CLAVR	Clouds from AVHRR
CLS	Constrained Least Squares
COPRS	Cloud Optical Property Retrieval System
CPR	Cloud Profiling Radar
CRH	Clear Reflectance, Temperature History (CERES Archival Data Product)
CRS	Single Satellite CERES Footprint, Radiative Fluxes and Clouds (CERES Archival Data Product)
DAAC	Distributed Active Archive Center
DAC	Digital-Analog Converter
DB	Database
DFD	Data Flow Diagram
DLF	Downward Longwave Flux

DMSP	Defense Meteorological Satellite Program
EADM	ERBE-Like Albedo Directional Model (CERES Input Data Product)
ECA	Earth Central Angle
ECLIPS	Experimental Cloud Lidar Pilot Study
ECMWF	European Centre for Medium-Range Weather Forecasts
EDDB	ERBE-Like Daily Data Base (CERES Archival Data Product)
EID9	ERBE-Like Internal Data Product 9 (CERES Internal Data Product)
EOS	Earth Observing System
EOSDIS	Earth Observing System Data Information System
EOS-AM	EOS Morning Crossing Mission
EOS-PM	EOS Afternoon Crossing Mission
ENSO	El Niño/Southern Oscillation
ENVISAT	Environmental Satellite
EPHANC	Ephemeris and Ancillary (CERES Input Data Product)
ERB	Earth Radiation Budget
ERBE	Earth Radiation Budget Experiment
ERBS	Earth Radiation Budget Satellite
ESA	European Space Agency
ES4	ERBE-Like S4 Data Product (CERES Archival Data Product)
ES4G	ERBE-Like S4G Data Product (CERES Archival Data Product)
ES8	ERBE-Like S8 Data Product (CERES Archival Data Product)
ES9	ERBE-Like S9 Data Product (CERES Archival Data Product)
FLOP	Floating Point Operation
FIRE	First ISCCP Regional Experiment
FIRE II IFO	First ISCCP Regional Experiment II Intensive Field Observations
FOV	Field of View
FSW	Hourly Gridded Single Satellite Fluxes and Clouds (CERES Archival Data Product)
FTM	Functional Test Model
GAC	Global Area Coverage (AVHRR data mode)
GAP	Gridded Atmospheric Product (CERES Input Data Product)
GCIP	GEWEX Continental-Phase International Project
GCM	General Circulation Model
GEBA	Global Energy Balance Archive
GEO	ISSCP Radiances (CERES Input Data Product)
GEWEX	Global Energy and Water Cycle Experiment
GLAS	Geoscience Laser Altimetry System
GMS	Geostationary Meteorological Satellite
GOES	Geostationary Operational Environmental Satellite
HBTM	Hybrid Bispectral Threshold Method

HIRS	High-Resolution Infrared Radiation Sounder
HIS	High-Resolution Interferometer Sounder
ICM	Internal Calibration Module
ICRCCM	Intercomparison of Radiation Codes in Climate Models
ID	Identification
IEEE	Institute of Electrical and Electronics Engineers
IES	Instrument Earth Scans (CERES Internal Data Product)
IFO	Intensive Field Observation
INSAT	Indian Satellite
IOP	Intensive Observing Period
IR	Infrared
IRIS	Infrared Interferometer Spectrometer
ISCCP	International Satellite Cloud Climatology Project
ISS	Integrated Sounding System
IWP	Ice Water Path
LAC	Local Area Coverage (AVHRR data mode)
LaRC	Langley Research Center
LBC	Laser Beam Ceilometer
LBTM	Layer Bispectral Threshold Method
Lidar	Light Detection and Ranging
LITE	Lidar In-Space Technology Experiment
Lowtran 7	Low-Resolution Transmittance (Radiative Transfer Code)
LW	Longwave
LWP	Liquid Water Path
LWRE	Longwave Radiant Excitance
MAM	Mirror Attenuator Mosaic
MC	Mostly Cloudy
MCR	Microwave Cloud Radiometer
METEOSAT	Meteorological Operational Satellite (European)
METSAT	Meteorological Satellite
MFLOP	Million FLOP
MIMR	Multifrequency Imaging Microwave Radiometer
MISR	Multiangle Imaging Spectroradiometer
MLE	Maximum Likelihood Estimate
MOA	Meteorology Ozone and Aerosol
MODIS	Moderate-Resolution Imaging Spectroradiometer
MSMR	Multispectral, multiresolution
MTSA	Monthly Time and Space Averaging
MWH	Microwave Humidity

MWP	Microwave Water Path
NASA	National Aeronautics and Space Administration
NCAR	National Center for Atmospheric Research
NESDIS	National Environmental Satellite, Data, and Information Service
NIR	Near Infrared
NMC	National Meteorological Center
NOAA	National Oceanic and Atmospheric Administration
NWP	Numerical Weather Prediction
OLR	Outgoing Longwave Radiation
OPD	Ozone Profile Data (CERES Input Data Product)
OV	Overcast
PC	Partly Cloudy
POLDER	Polarization of Directionality of Earth's Reflectances
PRT	Platinum Resistance Thermometer
PSF	Point Spread Function
PW	Precipitable Water
RAPS	Rotating Azimuth Plane Scan
RPM	Radiance Pairs Method
RTM	Radiometer Test Model
SAB	Sorting by Angular Bins
SAGE	Stratospheric Aerosol and Gas Experiment
SARB	Surface and Atmospheric Radiation Budget Working Group
SDCD	Solar Distance Correction and Declination
SFC	Hourly Gridded Single Satellite TOA and Surface Fluxes (CERES Archival Data Product)
SHEBA	Surface Heat Budget in the Arctic
SPECTRE	Spectral Radiance Experiment
SRB	Surface Radiation Budget
SRBAVG	Surface Radiation Budget Average (CERES Archival Data Product)
SSF	Single Satellite CERES Footprint TOA and Surface Fluxes, Clouds
SSMI	Special Sensor Microwave Imager
SST	Sea Surface Temperature
SURFMAP	Surface Properties and Maps (CERES Input Product)
SW	Shortwave
SWICS	Shortwave Internal Calibration Source
SWRE	Shortwave Radiant Excitance
SYN	Synoptic Radiative Fluxes and Clouds (CERES Archival Data Product)
SZA	Solar Zenith Angle
THIR	Temperature/Humidity Infrared Radiometer (Nimbus)

TIROS	Television Infrared Observation Satellite
TISA	Time Interpolation and Spatial Averaging Working Group
TMI	TRMM Microwave Imager
TOA	Top of the Atmosphere
TOGA	Tropical Ocean Global Atmosphere
TOMS	Total Ozone Mapping Spectrometer
TOVS	TIROS Operational Vertical Sounder
TRMM	Tropical Rainfall Measuring Mission
TSA	Time-Space Averaging
UAV	Unmanned Aerospace Vehicle
UT	Universal Time
UTC	Universal Time Code
VAS	VISSR Atmospheric Sounder (GOES)
VIRS	Visible Infrared Scanner
VISSR	Visible and Infrared Spin Scan Radiometer
WCRP	World Climate Research Program
WG	Working Group
Win	Window
WN	Window
WMO	World Meteorological Organization
ZAVG	Monthly Zonal and Global Average Radiative Fluxes and Clouds (CERES Archival Data Product)

Symbols

A	atmospheric absorptance
$B_\lambda(T)$	Planck function
C	cloud fractional area coverage
CF_2Cl_2	dichlorofluorocarbon
$CFCl_3$	trichlorofluorocarbon
CH_4	methane
CO_2	carbon dioxide
D	total number of days in the month
D_e	cloud particle equivalent diameter (for ice clouds)
E_o	solar constant or solar irradiance
F	flux
f	fraction
G_a	atmospheric greenhouse effect
g	cloud asymmetry parameter
H_2O	water vapor

I	radiance
i	scene type
m_i	imaginary refractive index
$\hat{N}$	angular momentum vector
N_2O	nitrous oxide
O_3	ozone
P	point spread function
p	pressure
Q_a	absorption efficiency
Q_e	extinction efficiency
Q_s	scattering efficiency
R	anisotropic reflectance factor
r_E	radius of the Earth
r_e	effective cloud droplet radius (for water clouds)
r_h	column-averaged relative humidity
S_o	summed solar incident SW flux
S_o'	integrated solar incident SW flux
T	temperature
T_B	blackbody temperature
t	time or transmittance
W_{liq}	liquid water path
w	precipitable water
$\hat{x}_o$	satellite position at t_o
x, y, z	satellite position vector components
$\dot{x}, \dot{y}, \dot{z}$	satellite velocity vector components
z	altitude
z_{top}	altitude at top of atmosphere
α	albedo or cone angle
β	cross-scan angle
γ	Earth central angle
γ_{at}	along-track angle
γ_{ct}	cross-track angle
δ	along-scan angle
ε	emittance
Θ	colatitude of satellite
θ	viewing zenith angle
θ_o	solar zenith angle
λ	wavelength
μ	viewing zenith angle cosine

μ_o	solar zenith angle cosine
ν	wave number
ρ	bidirectional reflectance
τ	optical depth
$\tau_{aer}(p)$	spectral optical depth profiles of aerosols
$\tau_{H_2O\lambda}(p)$	spectral optical depth profiles of water vapor
$\tau_{O_3}(p)$	spectral optical depth profiles of ozone
Φ	longitude of satellite
ϕ	azimuth angle
$\tilde{\omega}_o$	single-scattering albedo

Subscripts:

c	cloud
cb	cloud base
ce	cloud effective
cld	cloud
cs	clear sky
ct	cloud top
ice	ice water
lc	lower cloud
liq	liquid water
s	surface
uc	upper cloud
λ	spectral wavelength

Units

AU	astronomical unit
cm	centimeter
cm-sec^{-1}	centimeter per second
count	count
day	day, Julian date
deg	degree
deg-sec^{-1}	degree per second
DU	Dobson unit
erg-sec^{-1}	erg per second
fraction	fraction (range of 0–1)
g	gram
g-cm^{-2}	gram per square centimeter
g-g^{-1}	gram per gram
g-m^{-2}	gram per square meter

h	hour
hPa	hectopascal
K	Kelvin
kg	kilogram
kg-m^{-2}	kilogram per square meter
km	kilometer
km-sec^{-1}	kilometer per second
m	meter
mm	millimeter
µm	micrometer, micron
N/A	not applicable, none, unitless, dimensionless
ohm-cm^{-1}	ohm per centimeter
percent	percent (range of 0–100)
rad	radian
rad-sec^{-1}	radian per second
sec	second
sr^{-1}	per steradian
W	watt
W-m^{-2}	watt per square meter
W-$m^{-2}sr^{-1}$	watt per square meter per steradian
W-$m^{-2}sr^{-1}µm^{-1}$	watt per square meter per steradian per micrometer

CERES Top Level Data Flow Diagram

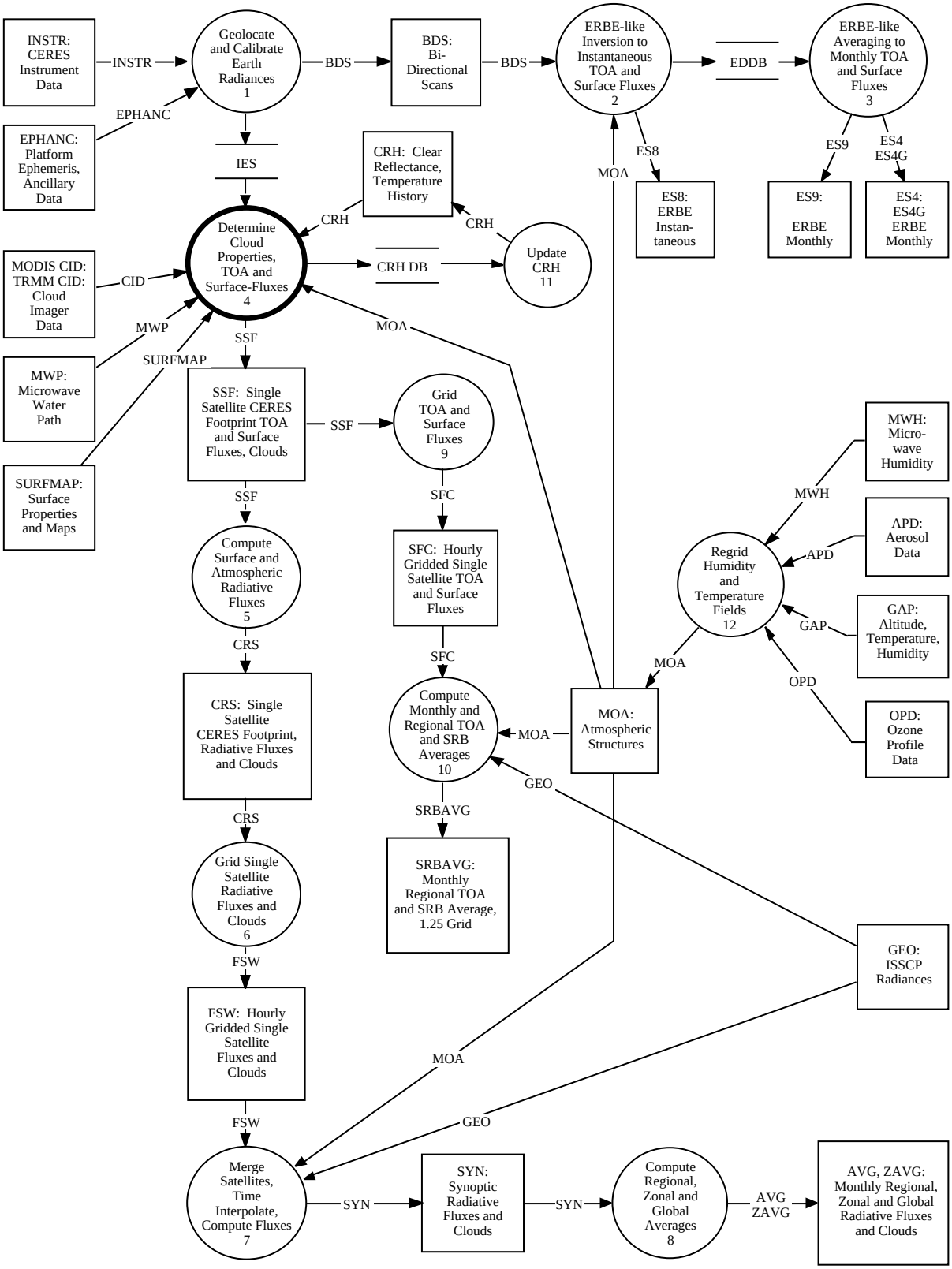

Subsystem 4.0 Top Level Data Flow Diagram

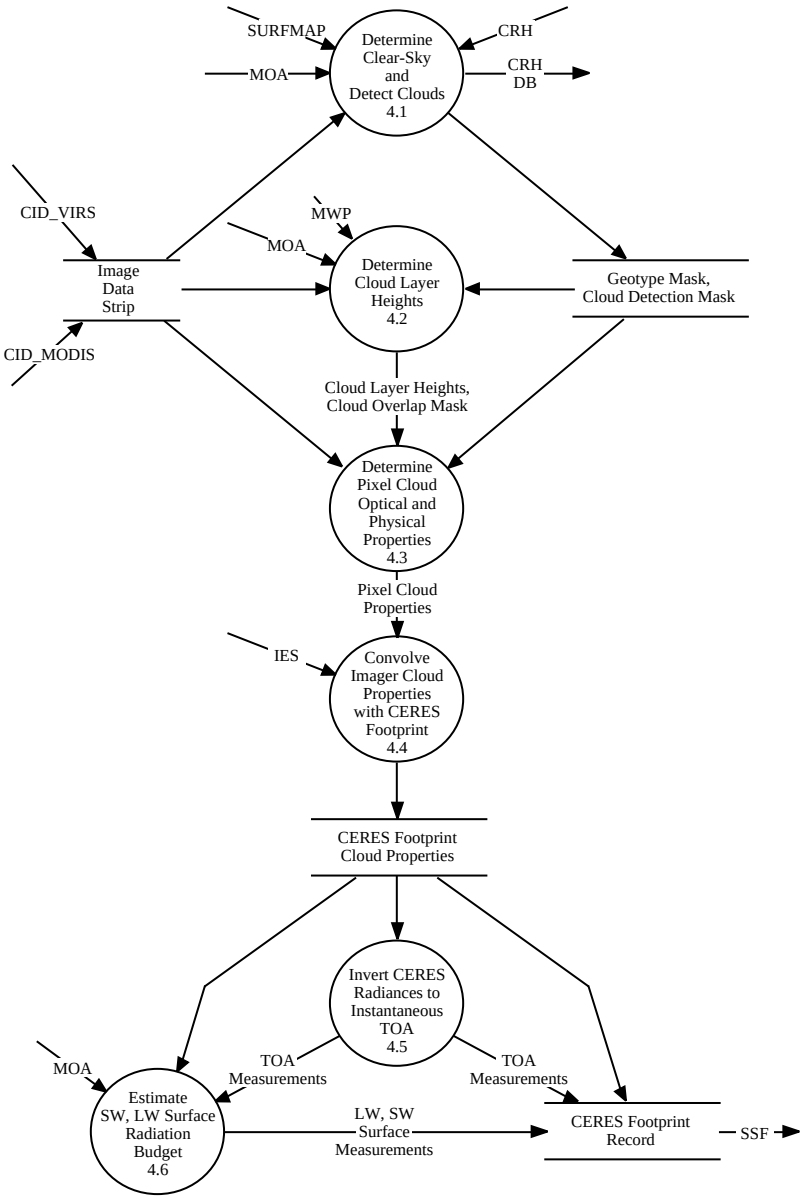

Clouds and the Earth's Radiant Energy System (CERES)

Algorithm Theoretical Basis Document

Imager Cloud Height Determination

(Subsystem 4.2)

CERES Science Team Cloud Retrieval Working Group

Bryan A. Baum[1]
Patrick Minnis[1]
James A. Coakley, Jr.[2]
Bruce A. Wielicki[1]

MODIS Science Team Cloud Retrieval Working Group

Paul Menzel[3]

Algorithm Implementation, Data Analysis, and Data Management

James Titlow[4]
Vasanth Tovinkere[4]
Pat Heck[5]
Shalini Mayor[5]

[1]Atmospheric Sciences Division, NASA Langley Research Center, Hampton, Virginia 23681-0001
[2]Department of Atmospheric Sciences, Oregon State University, Corvallis, Oregon 97331-2209
[3]Space Science and Engineering Center, University of Wisconsin, Madison, Wisconsin
[4]Science Applications International Corporation (SAIC), Hampton, Virginia 23666
[5]Analytical Services & Materials, Inc., Hampton, Virginia 23666

4.2. Imager Cloud Height Determination

4.2.1. Introduction

Section 4.1 discussed methodologies to provide two functions:

1. A global cloud mask
2. Scene classification using automated artificial intelligence schemes

Additionally, a scheme was outlined to update the clear-sky values for all five AVHRR channels depending on the results of the cloud-masking process. This section discusses the next two steps in the cloud-retrieval process, namely detection of cloud layers and determination of cloud-top pressure for each layer present. Several approaches are examined for use in the Version 1 CERES (Clouds and the Earth's Radiant Energy System) cloud-retrieval algorithm, such as spatial coherence (Coakley and Bretherton, 1982), multispectral techniques such as the layered bispectral threshold method (LBTM; Minnis et al., 1993), and artificial intelligence methods such as the fuzzy logic expert system approach. Additionally, the CO_2 slicing method will be used to determine mid- to high-level cloud-top pressures. A strength of spatial coherence and CO_2 slicing techniques is that they both work with infrared (IR) narrowband channels (at wavelengths between 11 and 15 μm) and thus are applied the same for both daytime and nighttime viewing conditions. The spatial coherence technique was designed to work for retrieval of low clouds, such as stratus and stratocumulus. Section 4.2.2 discusses the framework for the spatial-coherence algorithm. The LBTM daytime multispectral methods are discussed in section 4.2.3, the CO_2 slicing technique is outlined in section 4.2.4, and the fuzzy logic classifier in 4.2.5. The CERES Version 1 approach to inferring cloud-top pressures under conditions involving overlapping cloud layers is briefly outlined in section 4.2.5.

4.2.2. The Spatial Coherence Method

4.2.2.1. Identification of Cloud Layers from Satellite Imagery Data

Everyday observations of clouds suggest that many cloud systems form well-defined layers. Surveys of satellite imagery data for the global oceans suggest that as many as 20 to 30% of all 250-km scale regions contain single cloud layers. At smaller observational scales (60 km), the isolation of single cloud layers may be as high as 50% (Coakley and Baldwin, 1984). Observations for the First ISCCP Regional Experiment (FIRE) II Cirrus Intensive Field Observations (IFO) suggest that as many as 50% of all 100-km scale regions are either single-layered or cloud-free (Lin and Coakley, 1993). Although cloud systems are often presumed to obey the physical relationships associated with a plane-parallel, homogeneous cloud, as is the case in ISCCP (International Satellite Cloud Climatology Project), clearly layered cloud systems might be expected to exhibit such behavior more closely than would more complex cloud systems. Because of their pervasiveness and to the relative abundance of theoretical tools that can be used to analyze them, layered cloud systems deserve special attention in observations of the earth's cloud systems. Effective optical properties of layered cloud systems should generally be more readily measurable than the macrophysical and microphysical properties of individual clouds. Changes in clouds brought about by changes in the climate system might well be noted first in the properties of layered clouds.

Experience with imagery data during the 1980's leads to the conclusion that layered cloud systems are relatively easy to identify. Here the spatial-coherence method is described as one approach to identifying the layers. The spatial-coherence method uses the pixel-to-pixel variability in emitted radiances to identify pixels that appear to be overcast by clouds that form a layer. Optical properties of cloud layers can be deduced from the overcast pixels. Various degrees of quality control can be applied to the analysis to ensure that the pixels so identified are indeed overcast. The increase in quality, however, is at the

expense of the number of such systems that meet the criteria of being part of a well-defined layer. The algorithm will be applied to groups of pixels that have a similar surface type (e.g., water).

4.2.2.2. Historical Perspective

In the early 1980's, as is the case today, the favored approach for obtaining cloud properties from satellite observations was the application of thresholds to imagery data (Minnis and Harrison, 1984; Rossow et al., 1985; Rossow and Garder, 1993). Although multispectral, clustering methods were also used to attempt an automated identification of cloud structures, the final estimate of cloud properties was still derived assuming that each of the imagery pixels belonging to a certain cluster was completely covered by the cloud system represented by the cluster (Debois et al., 1982). Everyday experience, however, leads to expectations that the occurrence of broken clouds on scales that are smaller or comparable to the spatial resolution typical of imagers (i.e. ~4 to 8 km) is rather common. Furthermore, when the breaks occur, it is unlikely that the clouds align themselves to fall exactly within the footprint of an imager pixel. This type of spatial sampling problem leads to the conclusion that the errors associated with threshold estimates of cloud cover may be sizable, as early work on threshold methods foretold (Shenk and Salomonson, 1972) and recent work confirms (Wielicki and Parker, 1992; Chang and Coakley, 1993).

In anticipation of these errors, a number of methods were proposed to obtain the fractional coverage within imager fields of view. Platt (1983) proposed a modified version of the visible-infrared bispectral method introduced by Reynolds and Vonder Haar (1977). The method used plane-parallel radiative transfer theory to identify fields of view that were overcast with clouds having a given liquid water or ice water column amount from those that contained broken clouds. The method has been extended and refined by Minnis and Harrison (1984) and by Minnis et al. (1993a, b). Arking and Childs (1985) adopted a similar scheme but added radiances observed at 3.7 μm to allow for effects caused by droplet size in the plane-parallel radiative-transfer calculations. A third approach, the spatial-coherence method (Coakley and Bretherton, 1982), relied on the observation that many of the global cloud systems come in layers and that these layers extend over tens of kilometers, maintaining a fairly constant emission temperature over these scales. Where the region being observed is cloud-free or where it is overcast, the emitted radiances achieve a high degree of spatial uniformity at the pixel scale. Where the clouds are present but fail to completely cover the imager pixels, the emitted radiances vary erratically from pixel to pixel. While the spatial-coherence method explicitly seeks to identify the cloud layers, the retrieval of cloud properties employed in the bispectral and multispectral schemes relied on the assumption that the clouds being observed were part of a layer. The challenge is to develop an algorithm that identifies layers when present.

The spatial-coherence method identifies layers by identifying the portions of the region that exhibit a high degree of local uniformity in the emitted radiances. The purpose of this section is to outline a relatively simple approach to solving this problem. The solution is both a generalization and simplification of the earlier approaches (Coakley and Bretherton, 1982; Coakley and Baldwin, 1984). In the description given here, the method depends primarily on a single parameter—the difference in radiances expected for cloud-free and overcast fields of view. The dependence of the retrieved properties, namely the radiances associated with cloud-free and overcast portions of the region, is relatively insensitive to the choice of this parameter.

4.2.2.3. Theory Behind the Spatial-Coherence Method

The starting point for spatial-coherence analysis is the model of a well-defined, single-layered system of clouds over a relatively uniform background. What is meant by the term "well-defined" and

"relatively uniform" will be explained below. The emitted radiance observed by a radiometer viewing such a system is given by

$$I = (1 - C)I_{cs} + C(\varepsilon_{cld}I_{cld} + t_{cld}I_{cs}) \tag{4.2-1}$$

where I is the emitted radiance, C is the fractional cloud cover for the field of view, I_{cs} is the radiance associated with the cloud-free portion of the field of view, i.e. the radiance observed when $C = 0$. ε_{cld} is the mean effective emissivity associated with the cloud layer, t_{cld} is the mean transmissivity, and I_{cld} is the radiance that would be observed for overcast regions, i.e. $C = 1$, if the clouds were black at the wavelength of observation. In (4.2-1), the radiance is assumed to be at a infrared (IR) window wavelength so that downward emission above the cloud can be neglected. Likewise, the surface is assumed to be black at the wavelength of observation so that all radiation incident on the surface is absorbed, especially that emitted downward by the cloud. No radiation is reflected by the surface.

Over relatively small regions, i.e. ~100 km × 100 km to 500 km × 500 km scale, the emission of the clear-sky background, I_{cs}, and the height of the cloud layer, and therefore I_{cld}, are assumed to have little variance. That is, the effects of variations in the thermal emissions associated with the clear-sky background and the height of the cloud layer are small when compared with effects caused by variations in the fractional cloud cover and the cloud optical properties. If these conditions are met, the background is said to be relatively uniform and the layer is said to be well-defined. From (4.2-1), the variance of the radiances under such conditions is given by

$$(I - \bar{I})^2 = [(C - \bar{C})I_{cs} + (C\varepsilon_{cld} - \overline{C\varepsilon_{cld}})I_{cld} + (Ct_{cld} - \overline{Ct_{cld}})I_{cs}]^2 \tag{4.2-2}$$

The variances of emitted radiances over small areas spanning several imager pixels is the key to identifying the portions of a region that are cloud-free or overcast by clouds in a well-defined layer. Clearly, the variance becomes zero when the mean cloud cover in a region approaches zero. If the mean cloud cover is zero, then, of course, the fractional cover in every pixel i is also zero, i.e. $C = \bar{C} = 0$. Where the clouds become sufficiently extensive so that several imager pixels are overcast then, for analogous reasons, the variance approaches zero because $C = \bar{C} = 1$. Often when cloud systems become sufficiently extensive that they cover several imager pixels, they also become opaque. A notable exception, of course, is cirrus. For opaque, overcast clouds the variance again becomes zero because $t^i_{cld} = \bar{t}_{cld} = 0$ and $\varepsilon^i_{cld} = \bar{\varepsilon}_{cld} = \varepsilon_{cldmax}$, where t_{cld} is the cloud transmissivity and ε_{cldmax} is the emissivity that the clouds obtain when they become opaque, i.e $\varepsilon_{cldmax} = 1 - r_{cldmax}$, where r_{cldmax} is the reflectivity. To simplify notation, I_{cld} will be used to represent $\varepsilon_{cldmax}I_{cld}$ in the remainder of the text. It will be understood that I_{cld} is taken to be the emission observed for pixels overcast by opaque clouds. When pixels become overcast with opaque clouds, the variance in emitted radiances also becomes zero. When pixels become overcast by semitransparent clouds, like cirrus, pixel-to-pixel variations in the cloud optical properties, i.e. ε_{cld} and t_{cld}, prevent the variance from dropping to zero.

Because clouds appear to vary incoherently on the ~1 km × 1 km scale available to current satellite imagers, (4.2-2) indicates that variances in the emitted radiances for regions that are covered by several imager pixels will be nonzero when the region contains broken cloud. The variability will be caused partly by differences in the fractional cloud cover from pixel to pixel and partly by variations in the average cloud optical properties from pixel to pixel. The spatial-coherence method identifies pixels that are overcast by layered clouds where the clouds become opaque and pixels that are cloud-free by relying on the near-zero variances in emitted radiances for localized collections, or clusters, of the pixels. Collections of pixels that are partly covered by clouds or are overcast by clouds that are semitransparent invariably exhibit relatively larger variances.

It would appear that a simple threshold on the variance of emitted radiances would suffice to identify pixels that are overcast layered cloud systems. To a first approximation, the application of a simple threshold suffices; however, although fractional cloud cover and cloud optical properties tend to vary

incoherently on the ~1 km × 1 km scale, they can at times conspire to produce near-zero variances in emitted radiances while only partly covering a collection of pixels. Regular arrays of clouds arising from regular patterns of convection or mesoscale circulations will produce such instances. These conditions appear to be met only rarely. As a guard against these relatively rare occurrences, the spatial-coherence method relies not only on the low variances in the emitted radiances observed for cloud-free and opaque-overcast regions, but also on the clustering in the radiance domain of the pixels identified as cloud-free and overcast. The clustering must occur within a region that is, on average, rarely overcast or cloud-free, i.e. regions with scales of ~250 km × 250 km.

4.2.2.4. Spatial Considerations

4.2.2.4.1. Local scale, 4 km × 4 km to 8 km × 8 km. In the spatial-coherence method, the variability of the radiances is usually calculated for small arrays of adjacent pixels. Typically 2 × 2 (scan line × scan spot) pixel arrays are used for 4 km × 4 km AVHRR Global Area Coverage (GAC) data. The variability within each array is called the local variability. In the case of the 2 × 2 arrays of GAC pixels, the local variability is associated with 8 km × 8 km portions of the region. The size of the array over which the variability is calculated is not critical. It is reasonable to select a scale between 4 km × 4 km and 8 km × 8 km for the variance scale because the cloud-free and overcast portions of 250 km × 250 km regions are often several times the 4 km × 4 km to 8 km × 8 km scales. If the local standard deviations of the emitted radiances are plotted as a function of the local means for the pixel arrays covering a 250 km × 250 km region, an arch plot, typical of the spatial-coherence method, results (see Fig. 4.2-1). The figure shows the local means and standard deviations of the emitted 11-μm radiances for a 250 km × 250 km region over the Atlantic Ocean. The data points are from 4 × 4 arrays of 1 km × 1 km AVHRR observations collected during the 1992 Atlantic Stratocumulus-Transition Experiment (ASTEX). Figure 4.2-1 shows an arch that is typical of a single-layered system of marine stratocumulus. Radiances of 11 μm at the foot of the arch near 96 $mWm^{-2}sr^{-1}cm$ are associated with the cloud-free background. Radiances at the foot near 81 $mWm^{-2}sr^{-1}cm$ are associated with overcast pixels. In Figure 4.2-1, each point represents a 4 km × 4 km portion of the 250 km × 250 km region. There are approximately 1000 points in the plot. Every other 4 km × 4 km sample has been skipped.

For comparison, Figure 4.2-2a shows the same observations with the region divided to form 8 × 8 arrays of the 1 km × 1 km pixels. Each point in the figure now represents an 8 km × 8 km portion of the region. Again there are about a 1000 points in the figure. The similarity in radiances of the overcast and cloud-free feet with those in Figure 4.2-1 illustrate the lack of sensitivity to spatial scale. Figure 4.2-2b shows the same observations again but in this case the region was divided to form 2 × 2 arrays of 4 km × 4 km pixels. The 4 km × 4 km radiances were obtained by taking the corresponding averages of the 1-km radiances. As in Figure 4.2-2a, each point represents an 8 km × 8 km portion of the 250 km × 250 km scale region. The results in Figure 4.2-2b are like those obtained with 4 km × 4 km AVHRR GAC data. Although the radiances associated with the cloud-free and overcast feet differ little from those shown in Figures 4.2-1 and 4.2-2a, the arch in Figure 4.2-2b appears to be less well-defined than those in Figures 4.2-1 and 4.2-2a. The loss in clarity is produced by points dropping from the body of the arch towards the abscissa. This change in arch structure is consistent with the concept that clouds, when broken, populate adjacent 1 km × 1 km scale pixels incoherently. Because of this incoherence and the relative lack of sensitivity of the derived cloud-free and overcast radiances to the size of the array used, there appears to be some advantage to using large arrays of small pixels when possible rather than 2 × 2 arrays as has been used traditionally.

4.2.2.4.2. Frame scale, 250 km × 250 km. Like the size of the array used to calculate the local variance, the size of the region for which the spatial-coherence analysis is performed is not critical. The scale is arbitrarily chosen using the following guidelines. The region must be sufficiently large that cloud-free and overcast pixels occur relatively frequently. Furthermore, the spatial-coherence method uses a clustering method to distinguish between low local variances in the emitted radiances that

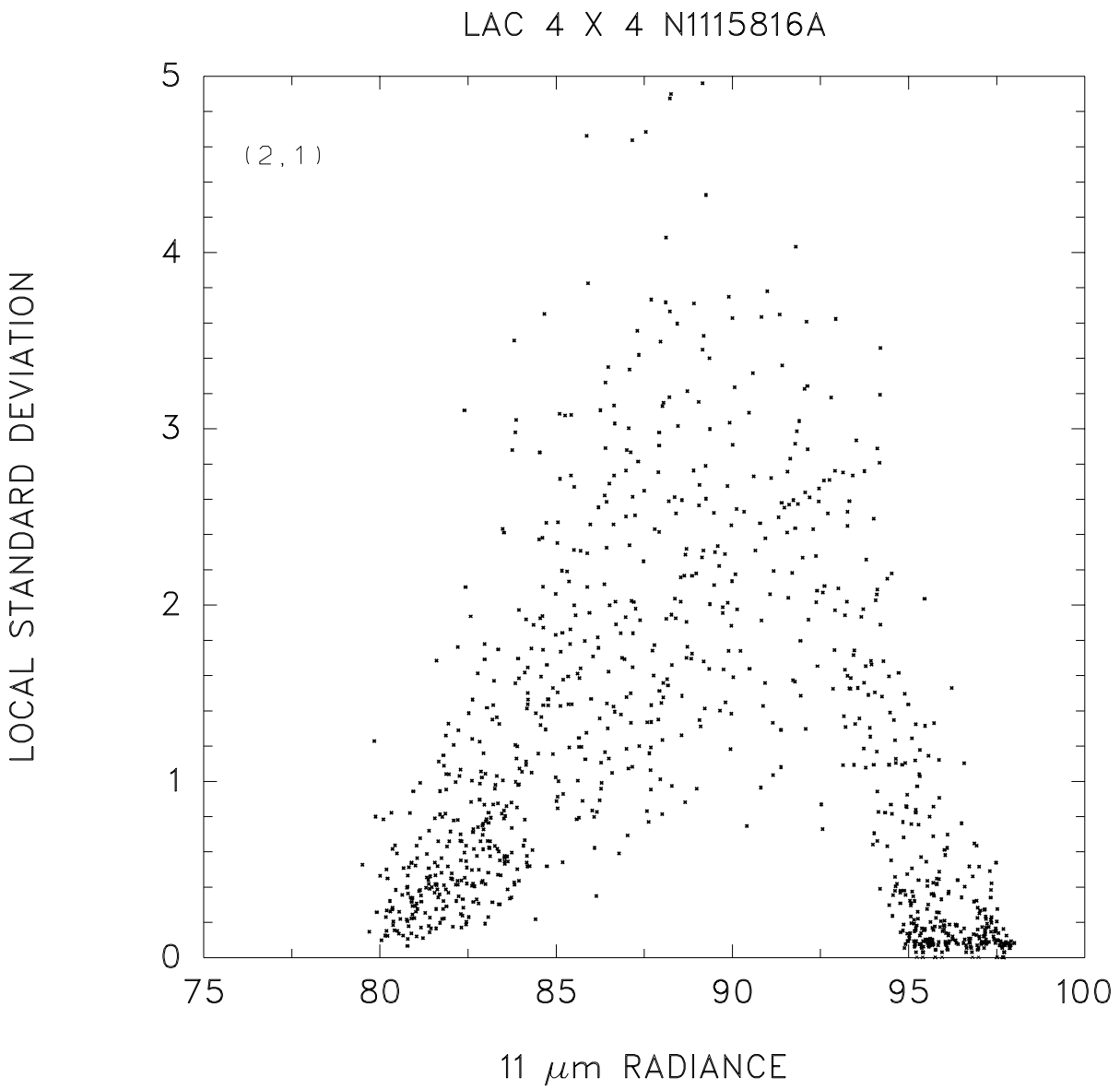

Figure 4.2-1. Local means and standard deviations for 250 km × 250 km region of the North Atlantic. Each point in the figure represents a 4 × 4 array of pixels constructed from 1-km AVHRR data. Each point represents a 4 km × 4 km portion of the 250 km × 250 km region. There are approximately 1000 points in the figure. These points were obtained by skipping every other 4 × 4 pixel array.

indicate cloud-free or overcast pixels from those that occur when pixels contain a repetitious pattern of broken clouds. Consequently, the region must be sufficiently large that it contains a substantial number of pixel arrays, i.e. ~1000 pixel arrays. It must be large enough that simple tests can be constructed to identify clustering within relatively narrow ranges of the emitted radiances against the null hypothesis that the radiances were randomly and uniformly distributed among the partly cloudy pixels. At the same time the region cannot be too large because variations of the radiances associated with cloud-free and overcast portions of the regions must remain small compared with the variability caused by variations in cloud cover and cloud optical properties. Experience with the spatial-coherence method has indicated that the 250 km × 250 km scale seems to satisfy these conditions. The 250 km × 250 km regions are termed frames in this analysis.

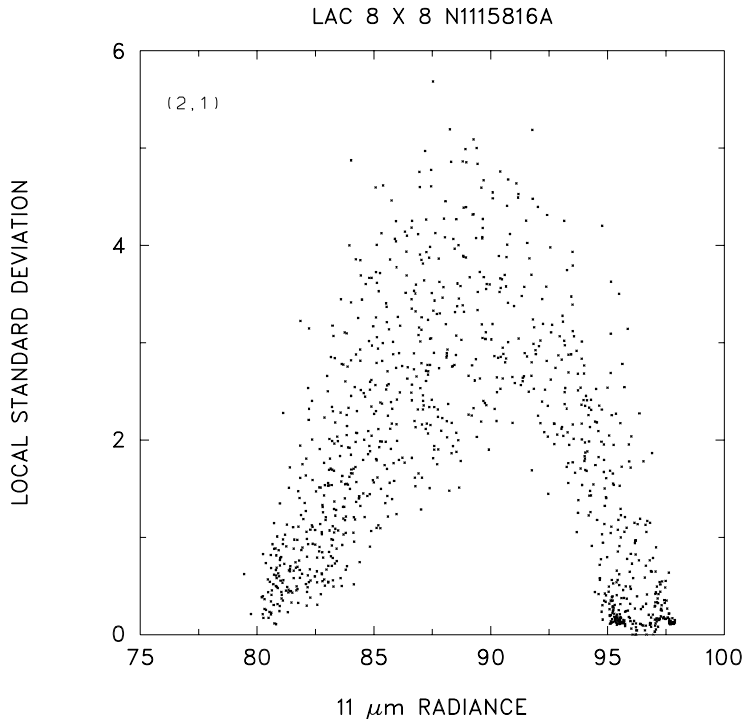

Figure 4.2-2a. Same as figure 1, but each point represents an 8×8 array of 1-km pixels, thereby representing an 8 km $\times$ 8 km portion of the 250 km $\times$ 250 km region. There are approximately 1000 points in the image. All 8×8 pixel arrays were used.

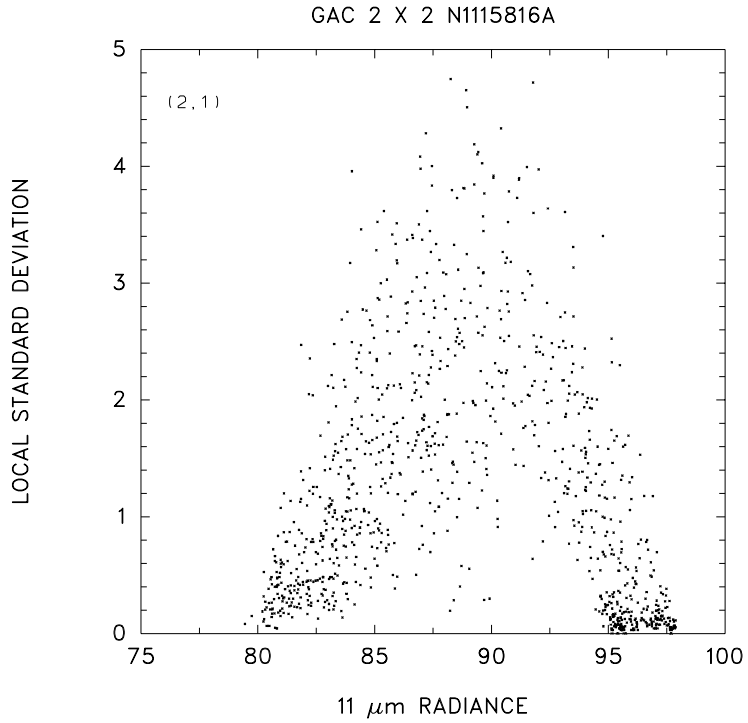

Figure 4.2-2b. Same as Figure 2a, but each point represents an 2×2 array of 4-km pixels.

4.2.2.4.3. Subframe scale, 50 km × 50 km. Once pixels within a 250 km × 250 km frame have been identified as being overcast or cloud-free, they are mapped to smaller subframes of ~50 km × 50 km that constitute the larger frame. The size of the smaller subframe is again immaterial. It is chosen to be sufficiently large to contain a relatively large number of pixels (~10^2) so that percentiles can be relied upon to be stable estimators of the range of radiances encountered in the subframes. Mapping the pixels to the subframes allows the construction of geographic gradients in the cloud-free background and overcast-opaque cloud radiative properties within the 250 km × 250 km frames. It also helps to isolate single-layered systems, for which simple plane-parallel theory applies, from more complex systems, for which suitable theories have yet to be developed.

4.2.2.5. Mathematics of Spatial Coherence Cluster Analysis

4.2.2.5.1. 250 km × 250 km frame scale analysis. This section addresses the problem of identifying which points in the arch diagram are associated with the feet of the arches (i.e. which are associated with cloud-free radiances); which are associated with overcast radiances for opaque, layered clouds; and which are associated with the body of the arch and thus with pixels that are either partly cloud covered or may be overcast with semitransparent clouds. The observations shown in Figure 4.2-3 will be used to illustrate the method for identifying the points that belong to the feet. The observations are for a 250 km × 250 km frame over the Atlantic Ocean. Like those in Figure 4.2-1, they were taken during the 1992 ASTEX experiment. Each point in the figure represents a 4 km × 4 km portion of the 250 km × 250 km scale frame. The observations indicate that the frame contains low-level and upper-level cloud layers. Because there are few pixels in the body of the arches associated with these layers, most of the pixels in this case are filled by either low-level or upper-level overcast cloud layers, or the pixels are cloud-free. Cases in which few pixels contain what appear to be broken clouds are rare (cf. Fig. 4.2-1).

It should be noted at the outset that the procedures presented here are somewhat arbitrary. The procedures are clearly not optimal in that they do not make use of any statistical description of how cloud systems actually populate imager pixels. Such a description would, for example, explain the different appearances of the arches shown in Figure 4.2-2. How broken cloud systems populate imager-scale pixels remains a subject of investigation. Nevertheless, while not optimal, the procedures presented here were designed with numerical efficiency and effectiveness in mind.

The identification of cloud-free and overcast fields of view involves the identification of pixel arrays exhibiting uniform emission. The first step is to decide on the magnitude of variability that will be allowed before a pixel array will be identified as containing broken clouds. There is, of course, a small but finite probability that pixel arrays containing broken cloud will also exhibit low spatial variability in emitted radiances. Subframes that are cloud-free or overcast by opaque clouds from a single layer cannot avoid exhibiting locally uniform emission. The locally uniform emission that is to be identified with a cloud layer or with cloud-free frames must exhibit emission within a narrow range of radiances, and the range over which the radiances are to be clustered must be defined.

The determination of the maximum standard deviation allowed for points in the feet of the arch and also for the range of radiances over which the points in a single foot are allowed to span is made by considering the effect of the variability in the radiances on the uncertainty in the cloud cover estimated from the spatial-coherence method. For a single-layered system of opaque clouds, (4.2-1) becomes

$$I = (1 - C)I_{cs} + CI_{cld} \tag{4.2-3}$$

The cloud cover is obtained by inverting (4.2-3). The uncertainty in the estimated cloud cover is thus given by

$$\Delta C = \sqrt{\frac{(1 - C)^2 \Delta I_{cs}^2 + C^2 \Delta I_{cld}^2}{(I_{cs} - I_{cld})}} \tag{4.2-4}$$

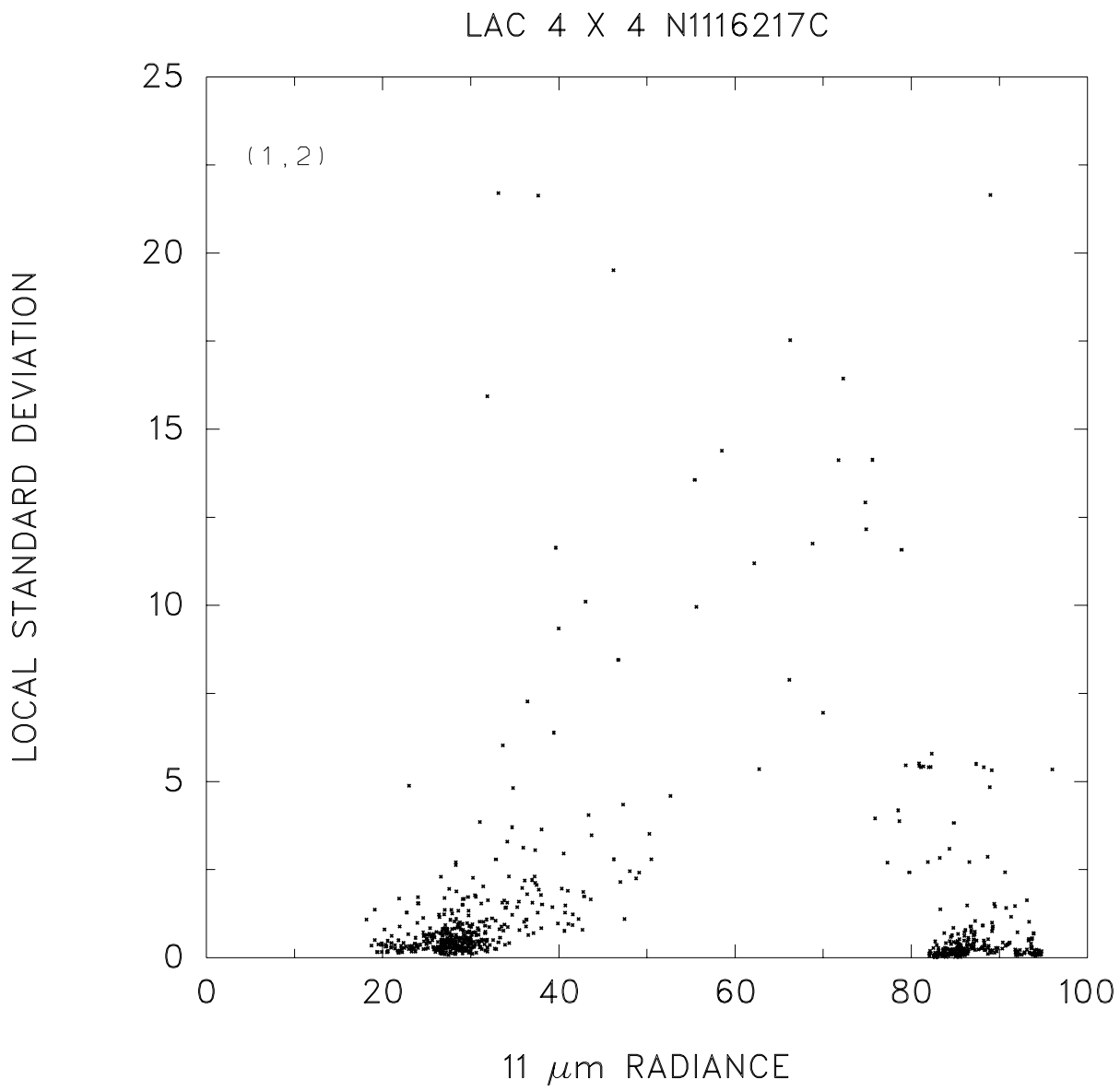

Figure 4.2-3. Same as Figure 1, but for a two-layered system.

The standard deviations of the radiances, ΔI_{cs} for the cloud-free and ΔI_{cld} for the overcast pixels, are taken to estimate the uncertainties in these radiances. Whether for overcast frames, (C = 1) or for cloud-free frames (C = 0), the uncertainty in the cloud cover associated with an array of pixels is given by

$$\Delta C = \frac{\sigma}{I_{cs} - I_{cld}} \tag{4.2-5}$$

where σ is the standard deviation of the radiances for the array. If χ is taken to be an upper limit to the uncertainty in cloud cover to be tolerated, then in order for an array to be part of an arch foot, its standard deviation must satisfy

$$\sigma \leq \chi(I_{cs} - I_{cld}) \tag{4.2-6}$$

Of course, there is no prior knowledge of (I_{cs} − I_{cld}). Examination of spatial-coherence results for oceans spanning the globe and differences between ninetieth and tenth percentiles of the emitted

radiances observed for ~250 km × 250 km frames over the globe suggests that ($I_{cs} - I_{cld}$) is the value associated with low-level marine stratocumulus. For 11-μm radiances this value ($I_{cs} - I_{cld\ low\text{-}level}$) appears to be about 20 $mWm^{-2}sr^{-1}cm$. Due to the larger variability of the cloud-free background, over land ($I_{cs} - I_{cld\ low\text{-}level}$) ~ 60 $mWm^{-2}sr^{-1}cm$ is used. The smallest value of the cutoff is taken to be

$$\sigma_{cutoff} \le \chi(I_{cs} - I_{cld\ low\text{-}level}) \tag{4.2-7}$$

where σ is the smallest value of the cutoff and the acceptable uncertainty in the cloud cover is taken to be χ = 0.03. As discussed below, the results of spatial-coherence analysis are insensitive to the actual choice of σ_{cutoff}.

The cutoff given in (4.2-7) is used for identifying pixels that are either cloud-free or overcast by ***low-level*** clouds. Obviously, for mid- and upper-level clouds the same equation applies with suitable values of $I_{cld\ mid\text{-}level}$ and $I_{cld\ upper\text{-}level}$ replacing $I_{cld\ low\text{-}level}$. For constant uncertainty in the fractional cloud cover, χ, these changes indicate that the allowable cutoff in the standard deviation can grow as ($I_{cs} - I_{cld}$) grows. This growth in σ_{cutoff} is implemented as follows: because I_{cs} is generally not known and is to be produced by the retrieval, the algorithm begins by replacing I_{cs} with the 90th percentile of the 11-μm radiances (I_{90}) for the frame of interest. The cutoff associated with a particular value of the array mean intensity I is assumed to be

$$\sigma_{cutoff}(I) \le \chi \mathrm{INTEGER}\left(\frac{I_{90} - I}{\gamma}\right) \tag{4.2-8}$$

where γ = ($I_{cs} - I_{cld\ low\text{-}level}$), which is taken to be 20 $mWm^{-2}sr^{-1}cm$ over oceans and 60 $mWm^{-2}sr^{-1}cm$ over land and INTEGER(x) is the integer value of x with the condition that INTEGER(x) ≥ 1.

In order to determine whether the points that survive the cutoff are clustered, as they appear to be in a foot, some method of measuring the number of points per unit radiance interval is required. The simplest measure is that given by the number of pixels per unit radiance interval. The intervals into which the radiances are divided are given by (4.2-8), i.e.

$$\Delta I = \chi \mathrm{INTEGER}\left(\frac{I_{90} - I}{\gamma}\right) \tag{4.2-9}$$

Figure 4.2-4a shows the distribution of radiances for the pixel arrays shown in Figure 4.2-3 and Figure 4.2-4b shows the distribution of radiances for the arrays that survive the standard deviation cutoff given by (4.2-8) for the radiance intervals given by (4.2-9). Note the following: first, the presence of the layers is revealed by peaks in the distribution of 11-μm radiances. Such peaks are uncommon. The norm is that the majority of pixels are partly cloud covered and so the radiances are randomly distributed over their range (Chang and Coakley, 1993). Second, note the shift in the width of the radiance intervals used in Figs. 4.2-4a and 4.2-4b. The intervals in Figure 4.2-4b at low values of the 11-μm radiance are larger than those used in Figure 4.2-4a. The shift is given by (4.2-9).

Clearly, the interval width used to determine the density of pixel-scale radiances will ultimately influence the uncertainty in the estimated cloud cover. The choice of the interval width is arbitrary. The interval width must be large enough that the number of pixels with radiances that fall within any given interval, were the radiances to be distributed uniformly over the range of radiances, is expected to be sufficiently large, i.e. 10. At the same time the interval must be sufficiently small that the distribution of radiances within a scene is approximated sufficiently well by the numbers of pixels in the various radiance intervals. That is, the intervals should be sufficiently small that a foot representing either the cloud-free background or an overcast layer is represented by arrays spanning several adjacent intervals.

In Figure 4.2-4b, each point that survived the cutoff was given equal weight. Clearly, points with smaller standard deviations are likely to have less cloud contamination for the cloud-free foot, or fewer

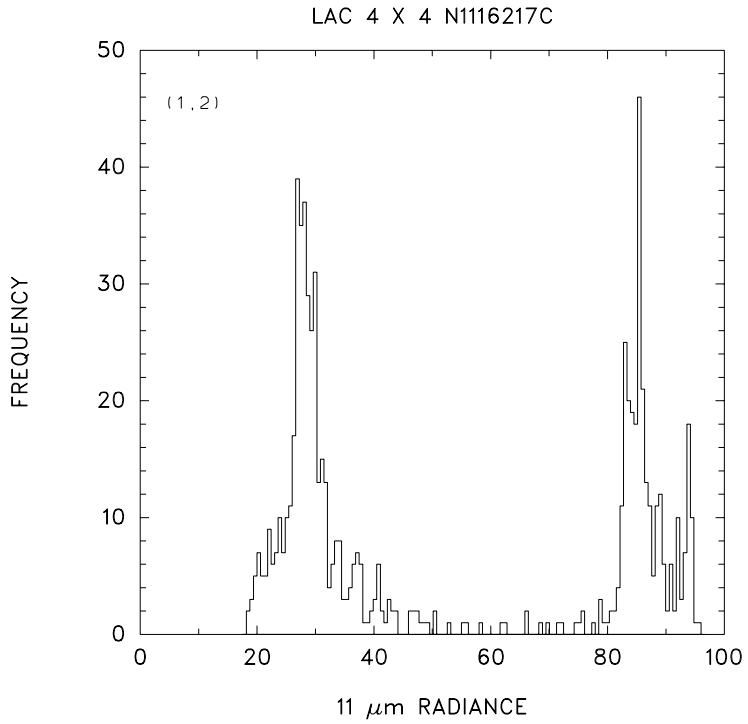

Figure 4.2-4a. Distribution of radiances for the observations shown in Figure 4.2-3.

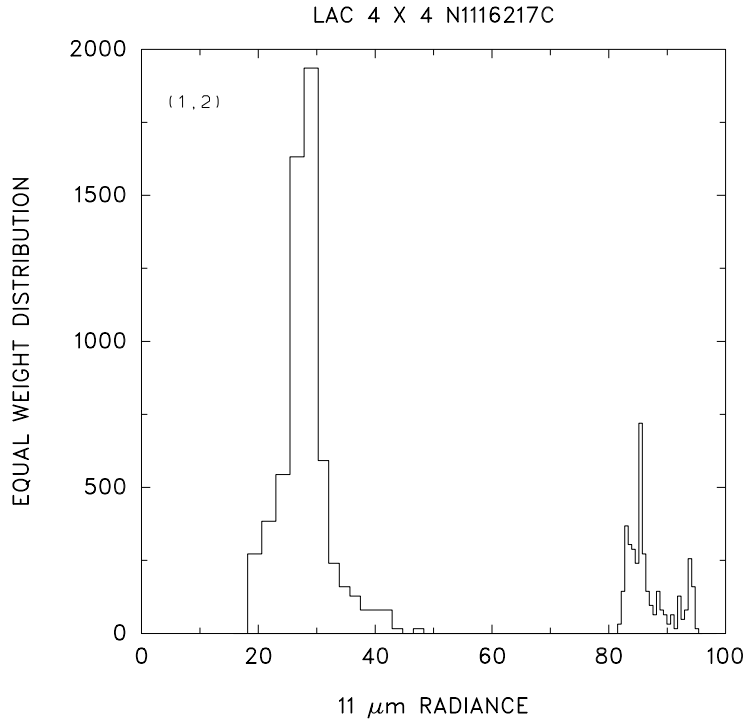

Figure 4.2-4b. Distribution of radiances for pixel arrays satisfying the cutoff in standard deviation given by Equation 4.2-8 for the radiance intervals given by Equation 4.2-9.

breaks in the clouds for the overcast foot than do points with larger standard deviations. Points with smaller standard deviations thus deserve more weight than those with larger standard deviations when estimating the radiance to be associated with the foot of an arch. By taking the radiances associated with each array to be uniformly distributed a new distribution function is created, $\rho(I)$, in which the contribution from a pixel array is approximately given by

$$\Delta\rho(I) = \frac{M\Delta I}{3\sigma} \tag{4.2-10}$$

where ΔI is the width of the interval associated with radiance I, I is the mean radiance of the array, M is the number of pixels in the pixel array, σ is the standard deviation of the radiances for the array, and 3σ approximates the relationship between the standard deviation of a uniform distribution and its domain. The allocation of contributions in each intensity interval are made symmetrically about the interval associated with the mean intensity, i.e. the interval itself, i, its nearest neighbor intervals, $i + 1$ and $i - 1$, and its next nearest neighbor intervals, $i + 2$ and $i - 2$, etc. within the range of the intensities associated with the pixel array. The new distribution $\rho(I)$ obtained by summing the contributions for all arrays in each of the radiance intervals is illustrated in Figure 4.2-5. The peaks of the distribution are clearly associated with the feet of the arches in Figure 4.2-3.

The next step involves determining the location and width of the peaks. The distribution is searched for local maxima. Once a maximum is found, the points in the interval and those on either side of the peak are used to calculate a mean and standard deviation of the radiances associated with the peak. The calculations are begun using the interval containing the peak, i, and the intervals on either side, $i + 1$ and $i - 1$. A second standard deviation of the radiances is calculated using the two adjacent intervals, $i + 2$ and $i - 2$, on either side of the original three-interval group. If the second estimate of the standard deviation is within 20% of the first, i.e. $\sigma_1 \geq 0.8\sigma_2$, then the width of the peak is taken to be given by the three intervals of the original group. For comparison, a Gaussian distribution gives $\sigma_1 \geq 0.74\sigma_2$ where σ_1 is the estimate of the standard deviation using the domain within one standard deviation of the mean and σ_2 is the estimate of the standard deviation using the domain within two standard deviations of the mean. If the condition is not met by the two estimates of the standard deviation, then the interval is expanded to the five-interval group and the next two adjacent intervals are added and a new standard deviation for the seven interval group is calculated and compared with that of the five interval group. This process is repeated until either the standard deviations for the two ranges agree within 20%, or in expanding the interval a peak in the $\rho(I)$ distribution is encountered that has a higher density of points, i.e. larger $\rho(I)/\Delta I$ than that of the original group. If the latter case is true, the original peak is dropped from further consideration and the test is transferred to the new, denser peak. In Figure 4.2-5 the peaks of $\rho(I)$ and their associated widths are indicated by dashed lines.

Once the peaks are located and their widths determined, neighboring peaks are examined to determine whether they overlap each other. The domain of a peak is taken to be the radiance intervals that lie within three standard deviations of the mean radiance associated with arrays forming the peak. If the domains of two peaks overlap, then the peaks are combined and the mean radiance and new standard deviation associated with the combined peak are calculated based on the arrays with mean radiances falling within the two standard deviation test intervals for the two separate peaks.

Once overlapping peaks are combined, they are tested for a minimum number of pixels. As as can be seen in Figure 4.2-4b, some pixel arrays exhibit locally uniform emission, like that exhibited by the points in the feet of the arch, but are not themselves part of a foot. Experience has shown that such points are eliminated by demanding that the foot of the arch must contain at least 20 pixels. As is shown in the Appendix, this minimum number of pixels can be explained through manipulation of an analog model in which the criterion is that the points associated with the foot of an arch must exhibit a tightly clustered distribution of radiances. Arrays that appear to satisfy the local uniformity condition but are not in the foot of an arch are randomly scattered over the range of emitted radiances observed for the

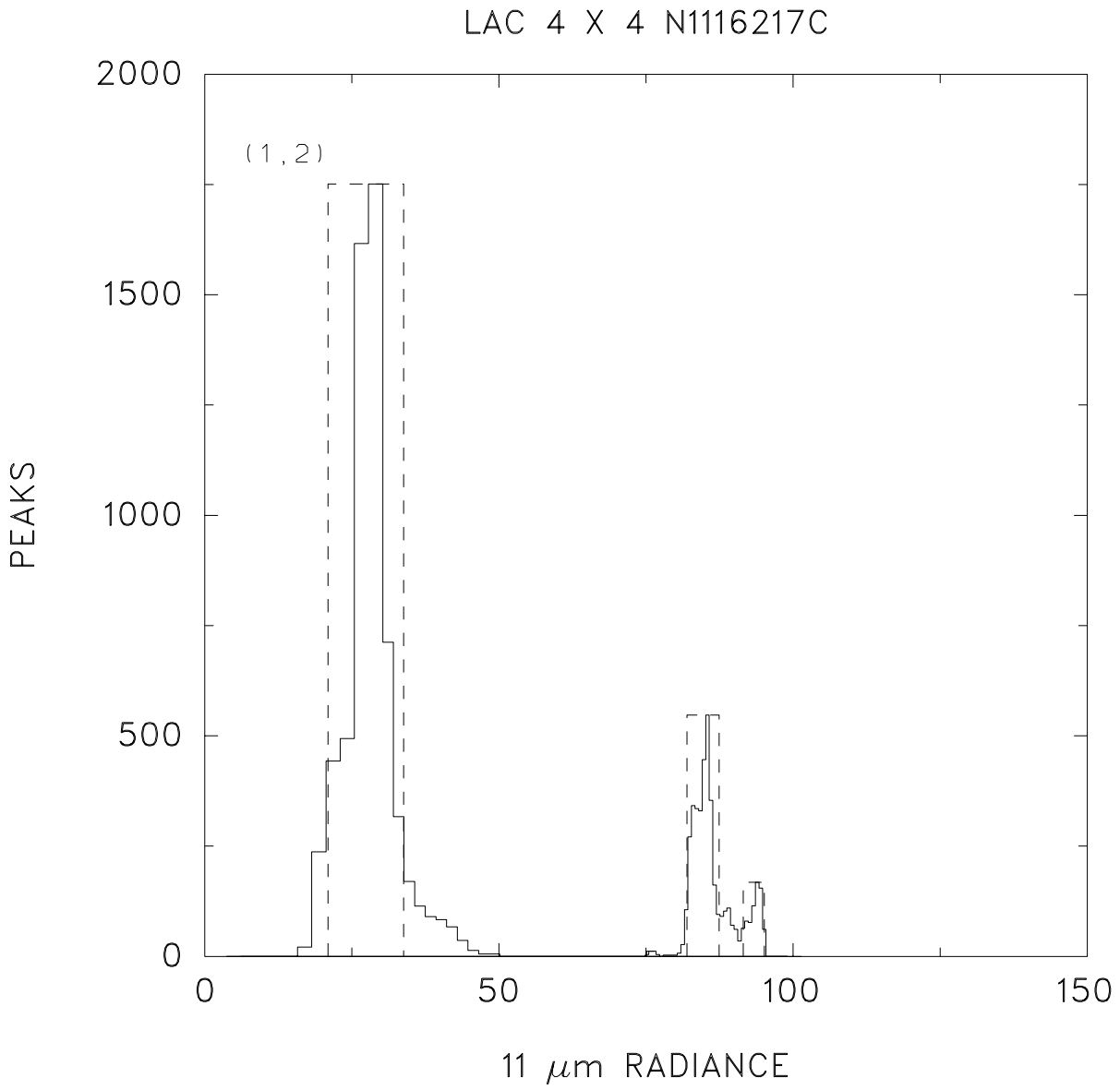

Figure 4.2-5. ρ(*I*) distribution for observations shown in Figure 3. The dashed lines indicate the radiance domains associated with the two layers and the cloud-free background.

frame. They fail to cluster around a specific radiance value as happens in the case of a foot. Experience with the spatial-coherence method indicates that employing this minimum number of pixels proved to be sufficient to eliminate the points that survived the uniformity cutoff but were not part of an arch foot in all but a few percent of the cases analyzed. In Figure 4.2-6, pixel arrays that were identified as being in the feet of the arches in Figure 4.2-3 are indicated by large dots; those that do not belong to a foot are indicated by small dots. Figure 4.2-6a shows the effect of the variable cutoff. The cutoff in the standard deviation is larger for the upper-level cloud deck (lower 11-μm emission). The figure also shows that the random pixel arrays exhibiting standard deviations similar in value to those in the feet have been eliminated. Figure 4.2-6b shows a scatter plot of 0.63-μm reflectivities and 11-μm radiances. Not surprisingly, the pixels identified as being cloud-free and overcast have bispectral properties that would be expected of cloud-free and overcast pixels. As discussed below, multispectral consistency checks might be developed to confirm the results obtained through spatial coherence analysis.

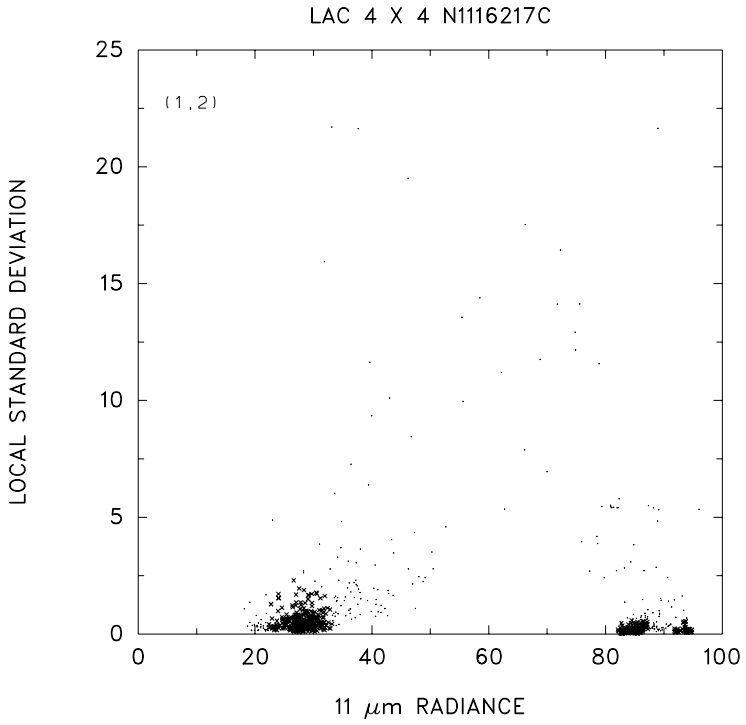

Figure 4.2-6a. Same as Figure 3, but pixel arrays identified as being cloud-free or overcast by clouds in a well-defined layer are indicated by large dots. Pixel arrays with broken or semitransparent clouds are indicated by small dots.

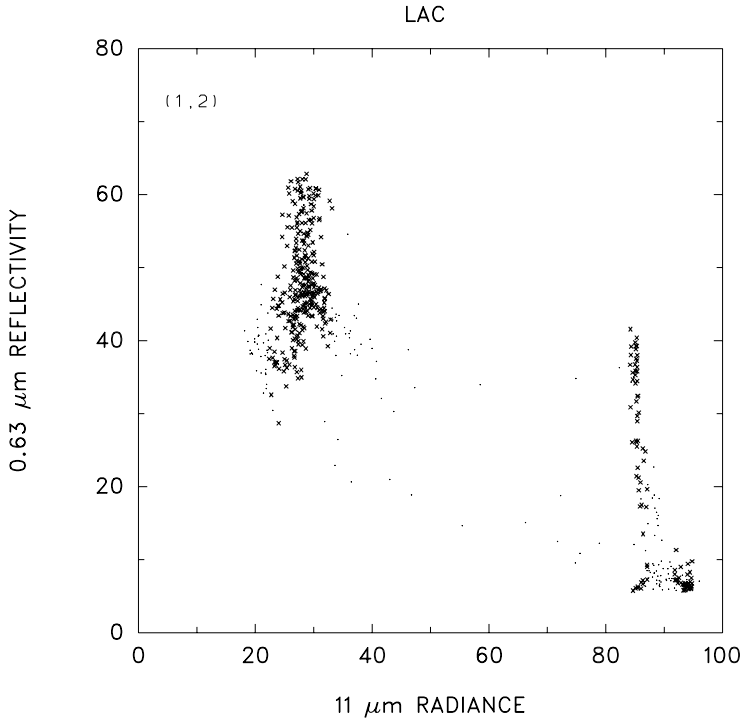

Figure 4.2-6b. 0.63- and 11-µm radiances for the observations shown in Figure 6a.

The variables used in the identification of pixels exhibiting locally uniform emission were

1. The difference between the radiances expected for cloud-free and overcast fields of view, $\gamma = (I_{cs} - I_{cld\ low\text{-}level})$,
2. The 90^{th} percentile of the emitted radiances, which was used in place of the cloud-free radiance to obtain σ_{cutoff}
3. The two-standard-deviation test used to determine the width of a peak in the $\rho(I)$ distribution
4. The use of three standard deviations to represent the domain of an isolated peak

Clearly, the choices for these parameters, while not without reason, were arbitrary. Fortunately, numerous arch feet obtained for 250 km × 250 km scale frames contain contributions from many pixel arrays and these arrays are often tightly clustered in the radiance domain. The outcome of the foot identification, namely the mean and standard deviation of the radiances for the pixels associated with the foot, is relatively insensitive to the variables chosen. The results differ little if γ is halved or doubled, if the 95^{th} or 85^{th} percentile is used in place of the 90^{th}, or if three standard deviations rather than two are used to determine the width of a $\rho(I)$ distribution peak and two standard deviations used to represent its domain.

4.2.2.5.2. 50 km × 50 km subframe scale analysis. As noted above, once identified on the 250 km × 250 km scale, the locations of the pixel arrays identified as being overcast and cloud-free are mapped to smaller regions of ~50 km × 50 km, or subframes. This mapping retains information on gradients in the radiative properties of cloud-free and overcast pixels across the 250 km × 250 km frame and better isolates, when possible, single-layered systems. Often on this smaller scale, however, no pixels are found to be either overcast or cloud-free. So, even though a single-layer system may span a 250 km × 250 km frame, it cannot be clearly identified as a single-layered system on the basis of the spatial structure of the 11-μm radiances found in some of the 50 km × 50 km scale subframes that make up the larger frame. This problem is illustrated in Figures 4.2-7 through 4.2-9. The figures show that although overcast pixels for a given cloud layer may not reside in a particular 250 km × 250 km frame, they often reside in surrounding frames. The finding suggests that when evidence for a layer is missing in one frame, surrounding frames should be examined for the missing evidence. While the example uses observations for the 250 km × 250 km scale, but clearly inferences made based on observations over a domain become more reliable as the size of the domain decreases.

Figure 4.2-7 shows means and standard deviations of 11-μm radiances and figure 4.2-8 shows the relationship of 0.63-μm reflectivities and 11-μm radiances for a 250 km × 250 km frame that, on the basis of the 0.63- and 11-μm scatter plot, contains two distinct layers. The spatial-coherence analysis in this case fails to identify either of the layers. Figures 4.2-8 and 4.2-9 show observations for the 250 km × 250 km scale frame shown in Figure 4.2-7 as well as for the surrounding 250 km × 250 km scale frames. The incipient layered structures not found in Figure 4.2-7 are now revealed in the surrounding frames. Coakley and Baldwin (1984) proposed analyzing the properties in mesoscale-sized regions called "subframes." They used 16 × 16 arrays of 4 km × 4 km AVHRR pixels, or a ~64 km × 64 km region for a subframe. If the subframe contained overcast pixels, or if the nearest neighbor subframes contained overcast pixels that explained the range of the emitted radiances, as defined by the 10^{th} and 90^{th} percentiles of the 11-μm radiances in the subframe of interest, then the subframe was taken to contain the layer. "Explaining" the range of radiances meant satisfying the following conditions:

$$(I_{cld} - 2\Delta I_{cld}) < I_{10} \tag{4.2-11}$$

and

$$I_{cld} + 2\Delta I_{cld} > I_{90} \tag{4.2-12}$$

where I_{cld} and ΔI_{cld} are the means and standard deviations associated with the overcast pixels in the frame surrounding the subframe in question. Values of the radiances are geographically interpolated to

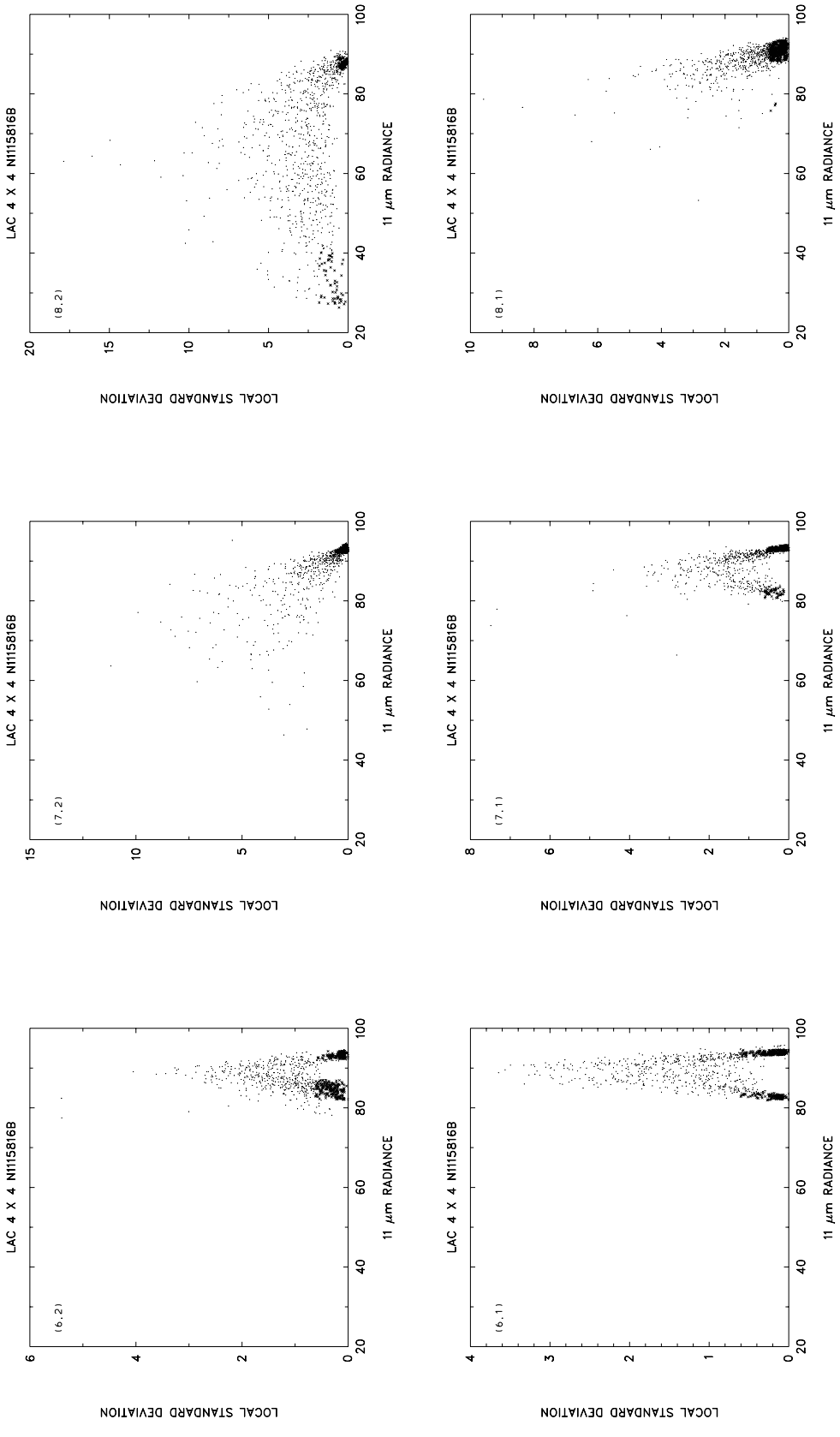

Figure 4.2-7. 3×2 array of adjacent 250-km scale frames. Each point represents a 4×4 array of 1-km AVHRR pixels. Large dots represent points found to be either overcast by layered clouds or cloud-free. The geographic orientation of the arrays are indicated by the (x,y) coordinates in the upper left corner of each frame. Frame $(m + 1, l + 1)$ is the frame immediately to the west and north of frame (m,l).

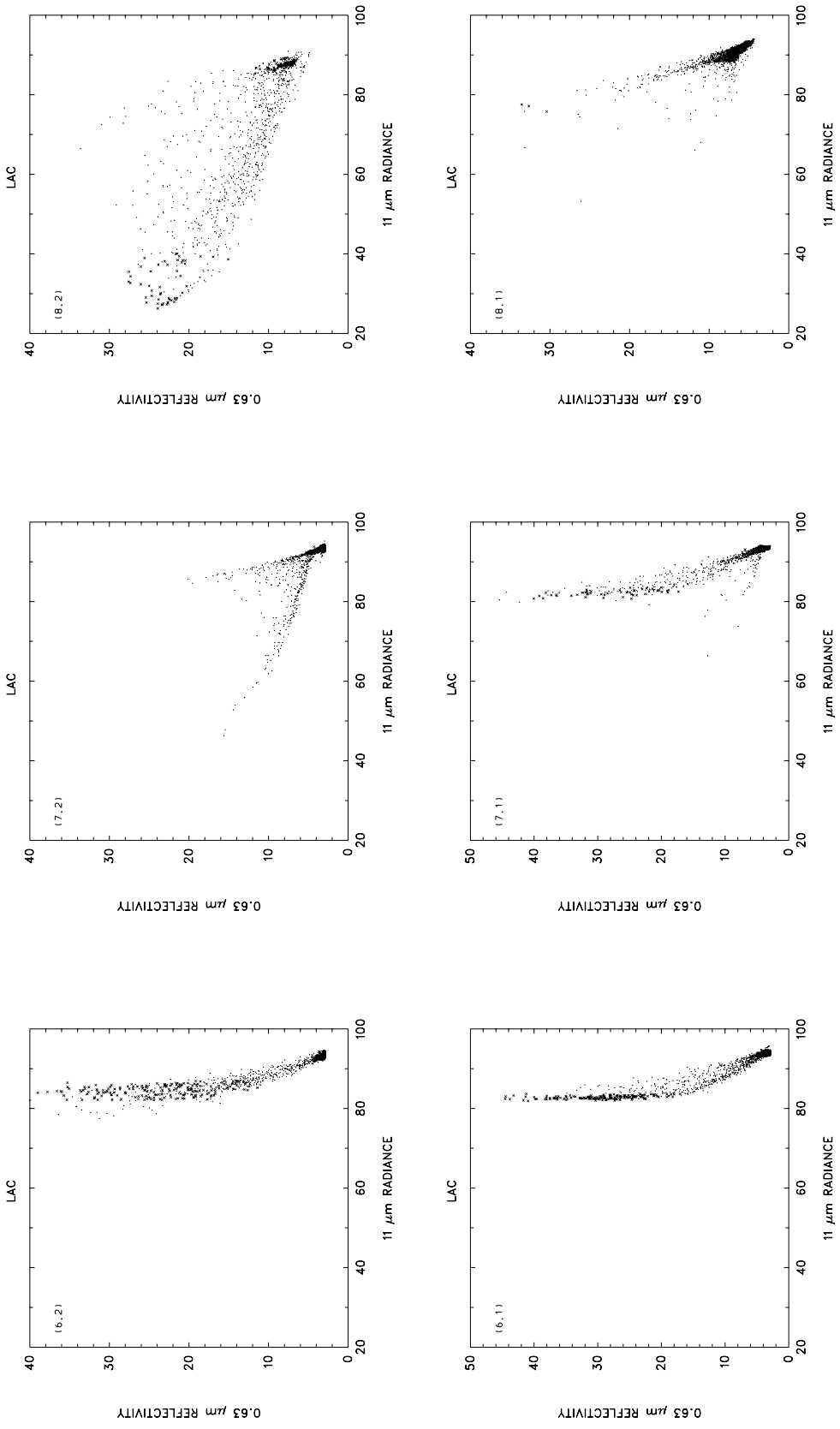

Figure 4.2-8. Same as Figure 7, but for 0.63- and 11-μm radiances.

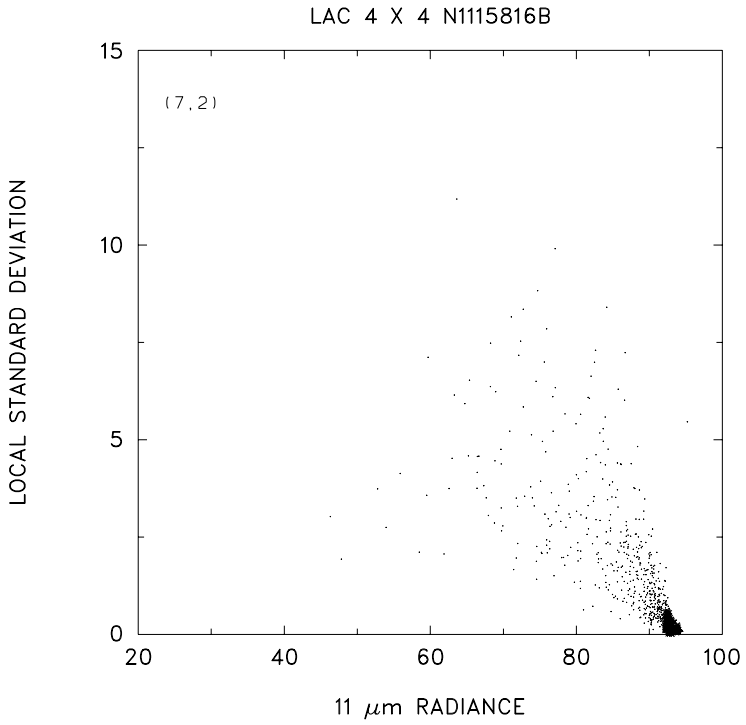

Figure 4.2-9a. Same as Figure 6a, but different two-layered system.

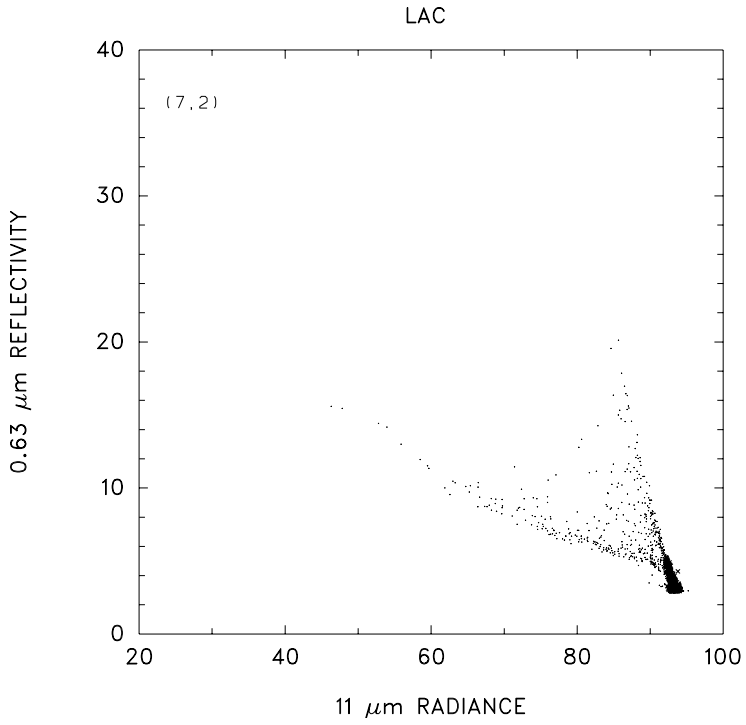

Figure 4.2-9b. 0.63- and 11-µm radiances for the observations shown in Figure 9a.

form estimates of the mean and standard deviation that would be achieved by overcast pixels in the subframe of interest were overcast pixels present.

Coakley and Baldwin (1984) followed a two-step procedure in implementing this search and interpolation of overcast radiances. First, all overcast pixels in a region containing the frame and the surrounding subframes (see Fig. 4.2-10) were classified into layers. The classification routine follows the same algorithm as that used to determine the feet of the arch with the exception that the range of 11-μm radiances was divided into equal intervals, ΔI, as opposed to variable-width intervals following (4.2-9). Up to three cloud layers were allowed. If more layers appeared to be present in the frame, then the layers that were nearest each other, $|I_{cld1} - I_{cld2}|$ = *minimum value*, were combined into one layer with the properties of the layer calculated to be the average of the properties for the contributing layers. In the averaging, each layer in each subframe was given equal weight. Once the layers in the frame were classified, the range of radiances in a particular subframe was examined to determine whether layers identified in the frame but not in the subframe were needed to explain the range. If so, the nearest neighbor subframes were searched for the overcast pixels associated with the appropriate layers. If overcast pixels were found in the surrounding subframes, then the radiances associated with the overcast pixels were geographically interpolated to the subframe of interest as discussed in Coakley and Baldwin (1984).

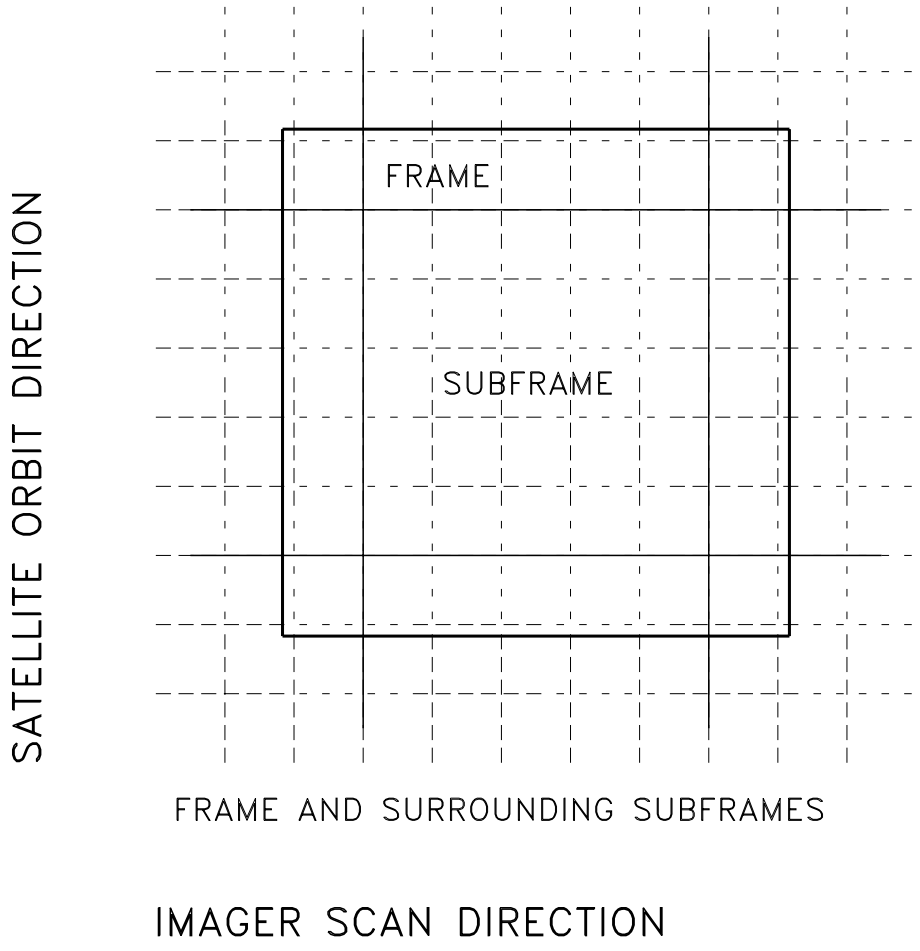

Figure 4.2-10. 50-km scale subframes and 250-km scale frames used in spatial coherence analysis. Each subframe represents the imager pixels mapped into a CERES footprint. Overcast and cloud-free 11-μm radiances for all subframes in a frame and its surrounding subframes are classified (as described in the text) to determine the layered structure of clouds for the subframes constituting the frame.

The extent to which this interpolation strategy would have to be implemented is unclear. Experience with the spatial-coherence method indicates that a substantial portion (somewhere between 30 and 60%) of all layers on the subframe scale are interpolated, even though the search for missing layers is limited to nearest neighbor 50 km × 50 km subframes. How far the search for missing layers can be extended, whether 50 or 100 km or further, has not been explored.

4.2.2.6. Uncertainties

This section discusses the uncertainties in the properties of the overcast pixels identified as being part of a well-defined cloud layer. In the following section, uncertainties arising through errors in layer identification, e.g. identifying a layer that doesn't exist or failing to identify a layer that does exist, are discussed.

The uncertainties associated with an identified layer are defined in terms of the standard deviations of the 11-μm radiances, $\Delta I_{cld,}$ obtained for the pixels identified as being overcast by opaque cloud. The standard deviation is used as a measure of the uncertainty in the retrieved layer properties. Included in this measure would be effects caused by gradients within the frame. Of course, because the probability is low that pixels overcast by opaque cloud will uniformly distribute themselves over a frame that is not itself overcast, the probability is likewise low that the standard deviation of radiances for the overcast pixels represents the range of layer properties within the frame.

As was noted in the introduction, a well-defined layer is by definition one for which the uncertainty in the properties, as indicated by the standard deviation of the 11-μm radiances for the overcast pixels, is small compared with the variability in the radiances that would result from variations in fractional cloud cover. Thus a well-defined layer has the property that $\Delta I_{cld} \ll I_{cs} - I_{cld}$. Clearly, this condition can be satisfied within rather arbitrary limits. The application of arbitrarily strict criteria will, of course, arbitrarily limit the population of well-defined layers. The degree to which various criteria affect the population of layers identified as being well-defined remains to be established. As a rule of thumb, however, requiring that the parameter given by

$$\xi = \frac{\sqrt{\Delta I_{cs}^2 + \Delta I_{cld}^2}}{I_{cs} - I_{cld}} \leq 0.1 \qquad (4.2\text{-}13)$$

would provide reasonably well-defined layers.

As discussed in the next section, cases exist in which layers may be identified as being present when in fact they are not. For example, the clouds in a layer congregate in regular arrays so that the observed emission satisfies the condition of low, local standard deviation, but the pixels are only partly cloud covered. Such occurrences appear to be rare. Nevertheless, they can probably be largely eliminated by demanding that the number of pixels identified as overcast and part of a well-defined layer must exceed a certain fraction of the area viewed, say 10%. This criteria is meant to apply only to those ~50 km × 50 km subframes that contain overcast pixels, not those for which layer information must be interpolated as described in Section 4.2.2.5.2. Interpolated properties are presumed to have the quality of the properties from which the interpolated values were obtained. Clouds can form regular arrays, but these arrays are fostered by mesoscale circulations which by their nature break down on the 100- to 200-km scale. The extent to which limiting the identification of well-defined layers by such a criteria and the likely dependence of such a criteria on spatial scales has not been explored.

4.2.2.7. Practical Considerations

Not all cloud systems are layered. Some layered cloud systems, like cirrus, rarely achieve optical depths that allow them to be detected as a layer by the spatial-coherence method. Systems of opaque layered clouds can also be everywhere broken so that nowhere do they extend to form overcast clouds over several imager pixels, thereby avoiding identification by the spatial-coherence method. Coastlines

and background heterogeneity over land areas may mask the presence of layers. This section outlines the limitations inherent in the spatial-coherence method and suggests strategies for dealing with them.

4.2.2.7.1 Limitations in Applying Spatial Coherence.

4.2.2.7.1.a. Errors caused by incorrect identification of cloud layers. Clouds don't always form opaque layers that span several imager pixels. Even if the clouds were in such a layered system, they would not give rise to the local uniformity in the emitted radiances that would allow detection by the spatial-coherence method. The variance in emitted radiances, as given by (4.2-2) for a single-layered system, could be relatively high. In the case of cirrus, even when the layer is extensive so that numerous pixels are overcast, the pixel-to-pixel variation in emissivity and transmissivity gives rise to large local variances in emitted radiances. Opaque, low-level clouds may form a layer in which the clouds are nowhere extensive enough to cover several adjacent imager pixels. An example of such a situation was shown in Figure 4.2-7.

There are three strategies for dealing with situations like those shown in Figure 4.2-7. The first, proposed by Coakley and Baldwin (1984), is to seek evidence for the presence of a well-defined layer in neighboring frames. That approach was discussed in Section 4.2.2.5.2. The second is to use relationships among various wavelengths. It constitutes an alternative to the spatial coherence method and is discussed in the subsequent section. The third is to use two-dimensional texture analyses to detect the presence of the separate systems. That approach likewise represents an alternative.

4.2.2.7.1.b. Errors caused by heterogeneous backgrounds. Land is a more heterogeneous background than oceans. As noted earlier, the identification of layers over land uses a cutoff in the standard deviation of the pixel arrays for land scenes that is three times the value used for ocean scenes. The increase in background heterogeneity over land, of course, diminishes the ability to identify well-defined layers. Nevertheless, experience with retrievals performed for the 1992 FIRE II IFO over the central U.S. indicates that the use of the higher cutoff provides satisfactory results (Lin and Coakley, 1993).

Contrasts between land and water at coastlines, of course, must be dealt with by separating the analysis for the land and water portions of the scene. Pixel arrays that include the coastline should not be used in the identification of the layer. Indeed, as the results in Figures 4.2-1 and 4.2-2 indicate, limited sampling over a 250 km $\times$ 250 km frame appears to provide overcast and cloud-free identifications that are indistinguishable from those obtained using all pixel arrays. Consequently, a perimeter of arrays bracketing coastlines can be safely ignored in the identification of cloud layers. Such a strategy, however, has yet to be implemented.

4.2.2.8. Proposal for Validation

Well-defined layers seemed to be readily identified by eye, but obtaining the properties of well-defined layers, even from instrumented surface sites and aircraft is difficult and not a well-posed problem. Consequently, finding evidence that a particular remote sensing technique produces a useful characterization of cloud systems is likewise difficult.

Two strategies for validation have already been proposed. Perhaps the best approach would be to use active aircraft or space-borne lidars to identify layers simultaneously with the information being retrieved from imagery data. The vertical sounding of the atmosphere with lidars often reveals layered structures. When clouds are thin and diffuse, it is difficult to assign a height to the layer; nevertheless, for optically thick clouds, the soundings produce what appear to be layers with reasonably well-defined altitudes.

A weakness of lidar retrievals is that they are typically limited to the nadir track of the aircraft or orbiting platform. The flight path will occasionally miss layered structures that are revealed through the two-dimensional sampling available to imagers. Consequently, comparisons between lidar cloud

boundaries and imager inferences of layered structure must be made on the basis of representative ensembles of cases, as opposed to a case-by-case basis. An opportunity for such comparisons is forthcoming with the LITE mission in September 1994 (McCormick et al., 1993).

The second strategy for validation proposed earlier was to demand that inferences of layered structure based on the spatial-coherence method be verified by independent inferences based on the relationships between radiances at various wavelengths. For example, Figure 4.2-6a clearly shows a two-layered structure as deduced from spatial-coherence analysis, and the visible-IR relationship shown in Figure 4.2-6b produces a consistent multiwavelength interpretation. Of course, such confirmation is bound to work for simple, layered cloud systems, i.e. when there is little overlap between the two systems in the frame of interest. When there is overlap, as may be the case in frame [2,1] of Figures 4.2-11 and 4.2-12, visible-IR observations will not necessarily provide the desired confirmation. Use of other multiwavelength emissions may alleviate some of the problems. Emission at 8 and 13 μm might reveal the branches associated with two-layered systems not revealed in the visible-IR scatter plots. Nevertheless, observations of thermal emission will capture only the highest and lowest layers present and not detected by the spatial coherence method, and they will miss intervening layers. As with lidar observations, the multispectral observations can be used to provide confirmation in a certain fraction of the cases, but not all cases.

Surveys with the spatial-coherence method suggest that single-layered cloud systems can be isolated on the ~50 km × 50 km scale approximately 50% of the time. Of the remaining 50%, many of these systems are two-layered systems that should be amenable to confirmation through multispectral approaches and lidar soundings. Complex cloud systems, i.e. those that defy description in terms of layered structure, appear to constitute only 15 to 25% of the observations at the 50 km × 50 km scale.

4.2.2.9. Quality Control

As was noted in an earlier section, arbitrary levels of quality control may be applied to the spatial-coherence identification of layered cloud systems. The quality of the layer indentifications may be measured in terms of the confidence limits with which the radiances associated with the layer might be specified. The rule-of-thumb criteria noted earlier, as given by (4.2-11) and (4.2-12), combined with the demand that a reasonable number of overcast pixels reside in the frame, say at least 10%, produces an acceptable number of layered systems when layers interpolated from adjacent subframe layers are counted. A requirement is that the adjacent subframe layers satisfy the conditions of (4.2-11) and (4.2-12). As noted earlier, tradeoffs between numbers of samples and uncertainties in layer definitions have not been studied.

The second approach to quality control is to demand that the layers identified through spatial-coherence analysis also be revealed in the relationships among various wavelengths. Perhaps the most revealing set of wavelengths for such confirmation would be 8 and 13 μm. Again, methods for identifying multiple layer structure on the basis of the relationships between various wavelengths have yet to be developed.

4.2.2.10. Numerical and Programming Considerations

The application of the spatial-coherence method for identifying layered structure places several requirements on the structure of the imager data stream. First, as was noted in Section 4.2.2.5.1, the identification of overcast pixels is performed on 250 km × 250 km scale frames. Second, because 50 km × 50 km subframes may lack overcast pixels for any of the layers present, some means are required for interpolating layer properties from one subframe to the next. Interpolation among nearest neighbor subframes each of order 50 km × 50 km scale was suggested. This frame and subframe scale analysis suggests a nested structure for the data stream as illustrated in Figure 4.2-10.

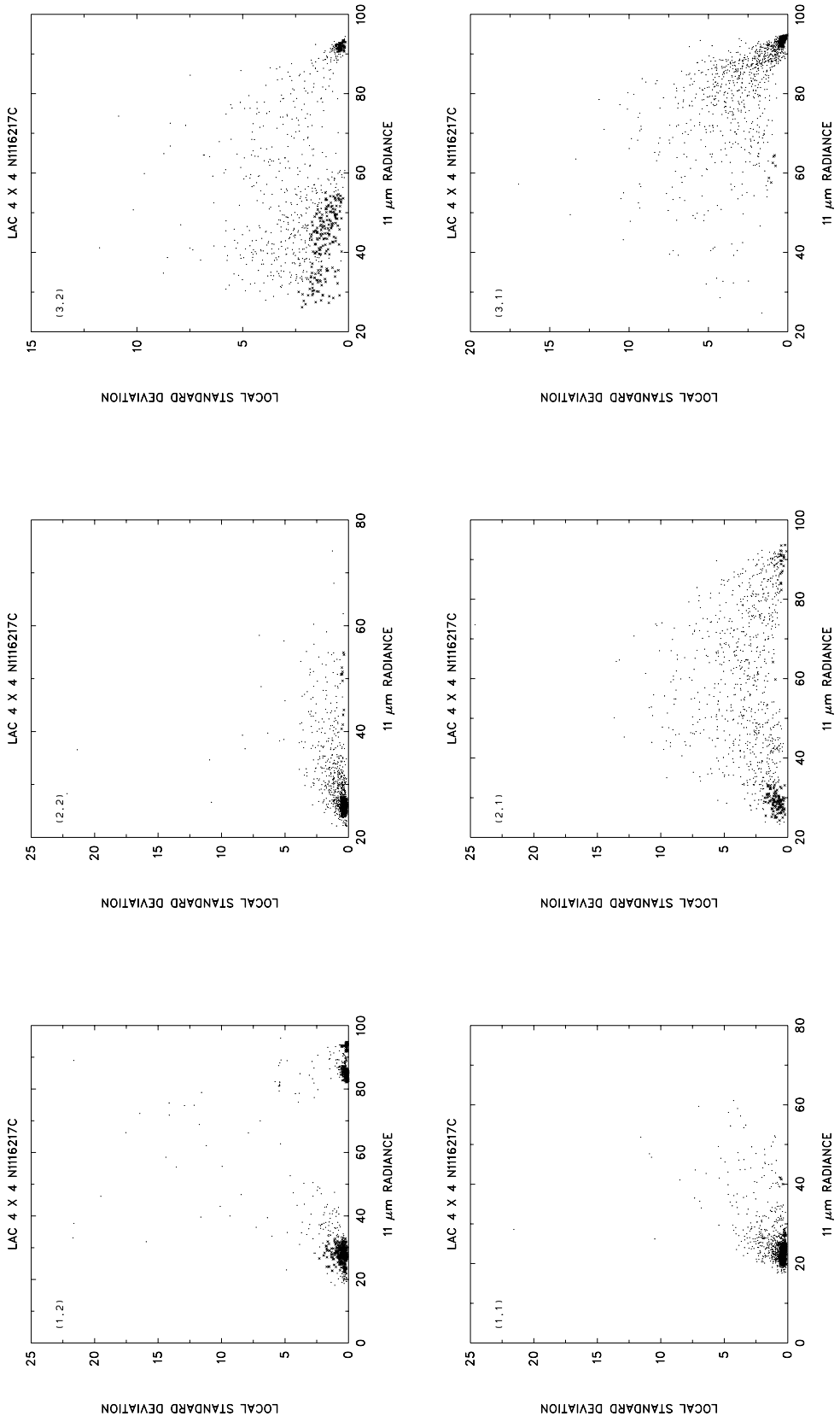

Figure 4.2-11. Same as Figure 7, except for different system.

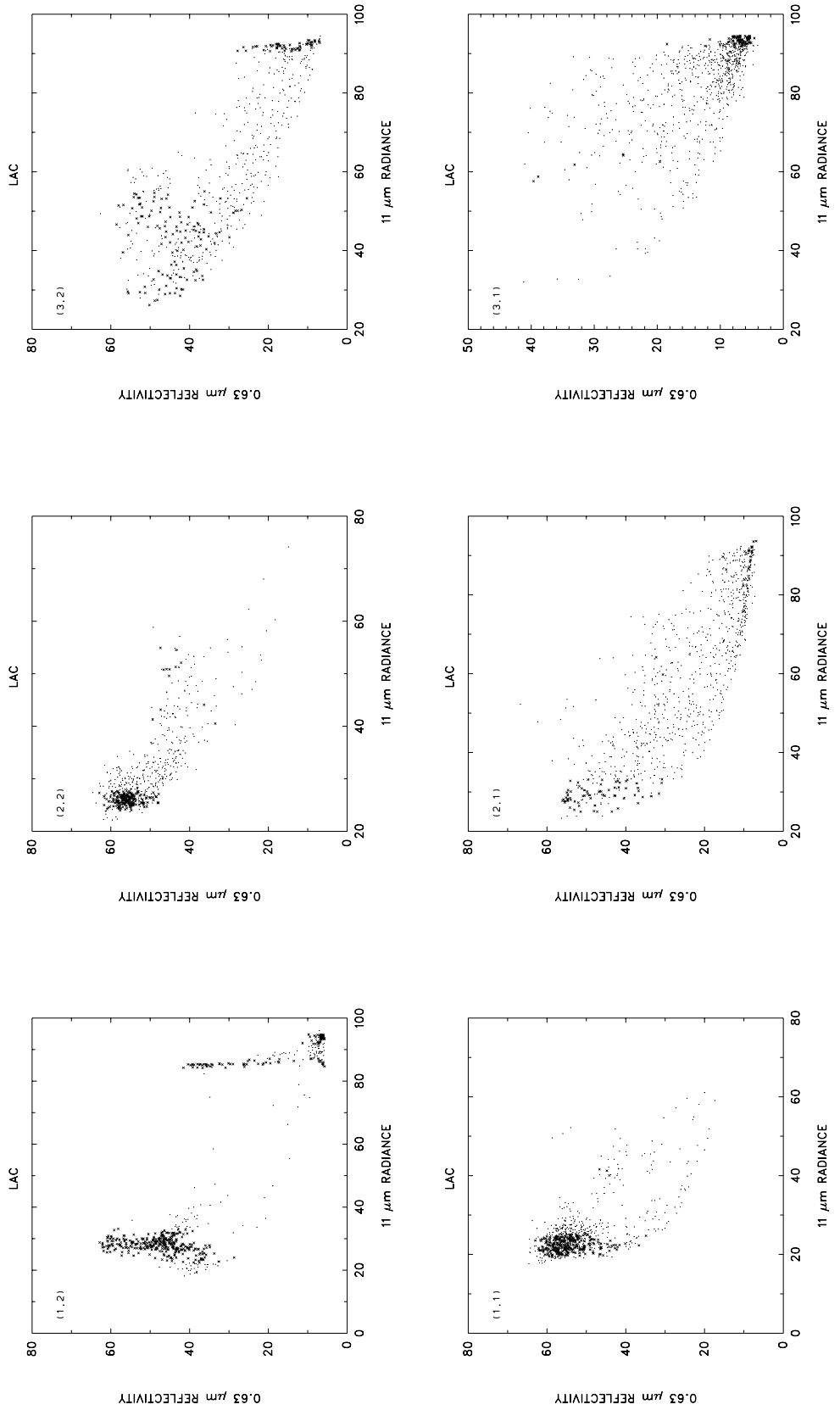

Figure 4.2-12. Same as Figure 11, but for 0.63- and 11-µm radiances.

The spatial coherence identification of layers would be undertaken as follows:

1. Overcast and cloud-free pixels would be identified in each 250 km × 250 km scale frame.

2. Overcast pixels within a frame and its surrounding 50 km × 50 km scale subframes would be classified to identify the overcast pixels with the various well-defined layers and assign the overcast pixels to specific layers.

3. Layers within the subframes constituting a frame would be determined on the basis of the layer identification of the overcast pixels within the subframe and its surrounding subframes.

These steps dictate the following structure. Spatial-coherence analysis is performed on imager scan lines sufficient to form a 250 km × 250 km scale frame. The analysis is performed for all 250 km × 250 km scale frames across the scan. Pixel radiances and layer identifications is retained in memory for a set of imager scan lines sufficient to form two adjacent sets of frames, i.e. 500 km × 500 km along the orbital track. In addition, 50 km × 50 km subframe scale layer properties are retained from the analysis of scan lines analyzed just prior to those currently in memory. Once the frame scale analysis is complete, the subframe scale analysis can begin with the first subframe of the scan lines residing in memory and end with the set of subframes that complete the first 250 km × 250 km scale frames spanned by the scan lines residing in memory. The results of the analysis for the subframes making up these 250 km × 250 km scale frames can be scrolled out of memory with the last set retained for the subsequent analysis of the subframes constituting the next 250 km × 250 km block of scan lines. New scan lines are read into memory forming a new 250 km × 250 km scale block and the spatial coherence analysis is applied to these new scan lines. The process is repeated.

Numerical efficiency has, to some extent, been addressed in the design proposed for the analysis. The design uses a uniform distribution to characterize the distribution of radiances within a spatial-coherence pixel array. This choice was intentional. It reduces numerical burdens incurred by using other distributions, such as Gaussian. It also is easier to implement than using the actual distribution of the pixel scale radiances. There is no point in resorting to the actual distribution of the pixel radiances, because, in order to identify clustering, the density of pixel-scale radiances must be measured and the measure used is somewhat arbitrary. Fortunately, as was noted earlier, the natural clustering of points about a well-defined range of emitted radiances forms a robust feature that can be readily characterized by any number of methods. The outcome, namely the means and standard deviations of the radiances associated with overcast pixels, will be relatively insensitive to the method used to identify clusters of locally uniform emitted radiances. The strategy proposed here is thought to be a simple, efficient, and effective means of seeking those results.

4.2.3. Multispectral Approaches

A second strategy for identifying layers missed by spatial-coherence analysis is to use multispectral histogram methods. Figure 4.2-7 clearly showed branches in the visible-infrared scatter plots associated with distinct layers, both of which were missed by the spatial-coherence method. Similar branches are observed at night for emission at 3.7 and 11 μm (Coakley, 1983). Fitting procedures, like those developed by Lin and Coakley (1993) for the multispectral analysis of single-layered systems might be generalized to identify branches associated with distinct layers. Alternatively, a variation of the hybrid bispectral threshold method (HBTM) of Minnis and Harrison (1984) and Minnis et al. (1987) or the layered bispectral threshold method (LBTM; Minnis et al., 1993) could be used to analyze such systems. A second set of multiregion, multilayer observations are shown in Figures 4.2-11 and 4.2-12. Here the upper-level system is clearly defined in frame [2,1], but there is no indication of lower-level systems that are prevalent nearby in frames [1,2] and [3,2]. Without additional logic, the HBTM or LBTM may divide the system shown in [2,1] into three distinct layers with predefined properties: high, middle and low. Thus, this multispectral approach may place multiple layers where only single layers exist. Some

simple modifications to the LBTM, however, can eliminate much of the ambiguity associated with single and overlapping layers.

4.2.3.1. Daytime Methodology

The LBTM is similar to the ISCCP algorithm in that it compares the 11-μm temperature T and reflectance ρ for each pixel to simple thresholds to determine if a pixel is cloudy or not. Instead of retrieving a visible optical depth τ and cloud temperature T_{cld} for each cloudy pixel, the LBTM groups some pixels together before deriving T_{cld} and τ. The LBTM nominally divides a visible-infrared histogram into three layers defined by hypothetical cloud temperatures at 2 and 6 km. Low clouds are those below 2 km, mid-level clouds are between 2 and 6 km, and high clouds are those above 6 km. When no τ- and T_{cld}-solutions are possible for a nominal pixel grouping (discussed below), the LBTM attempts to reach a solution for a group of pixels by adding other pixels to the group until a solution is obtained. The LBTM also computes the mean layer cloud temperature T_k and optical depth τ_k as well as their respective standard deviations σ_{Tk} and σ_{tk} where k =1, 3 from low to high. Other differences between the two methods include ice-crystal reflectance models for high clouds, bidirectional reflectance models for clear scenes, and a parameterization of the Earth-atmosphere system reflectance.

The reflectance is parameterized in terms of τ, the cloud altitude, clear-sky reflectance ρ_{cs}, the cloud particle size, the solar zenith angle θ_o, the viewing zenith angle θ, and the relative azimuth angle ψ. The 11-μm emittance is a function of τ, μ (= $cos\,\theta$), and the difference between the clear-sky temperature T_{cs} and the cloud temperature T_{cld}. For liquid water clouds, it is assumed that the cloud consists of spherical droplets having an effective radius of 10 μm. Ice clouds are assumed to be composed of randomly oriented hexagonal ice crystals representing a cirrostratus size distribution (Takano and Liou, 1989). The ice model is used for $T_{cld} < 253$K and the water-droplet model is applied for warmer cloud temperatures. The parameterizations of reflectance and emittance are detailed in section 4.3.

Given the relationships between cloud reflectance and emittance, it is possible to define the variation of ρ and T for a given value of T_{cld}. The variation in brightness temperature for a given value of τ or ρ is

$$T_\varepsilon = T_\varepsilon(\rho, T_{cld}) = B^{-1}\{\varepsilon(\rho)B(T_{cld}) + [1-\varepsilon(\rho)]B(T_{cs})\} \quad (4.2\text{-}14)$$

where T_ε is a model-defined emittance-dependent brightness temperature and B is the Planck function. The emittance ε and ρ are computed from the emittance and reflectance parameterizations at various values of τ. Thus, a value of T_ε corresponding to a cloud having T_{cld} can be defined for any given reflectance and microphysical model.

Figure 4.2-13 shows an AVHRR visible-infrared histogram for an area over the southwestern tropical Pacific. The numbers plotted in the histogram represent the number of occurrences of the particular T-ρ pair. The AVHRR 11-μm sensor is channel 4, so the brightness temperatures are indicated with the subscript 4. As currently formulated, the LBTM histogram is divided into five areas: clear, low cloud, middle cloud, high cloud, and dark pixel or stratospheric cloud. The clear area incorporates all pixels having $T > T_{cs} - \Delta T$ and $\rho \le \rho_t$ where ρ_t is the reflectance threshold value and the cloud threshold difference ΔT has values of 6 K over land and 3 K over water. The clear-sky visible threshold reflectance is ρ_t as defined by Minnis et al. (1987). All other pixels are assumed to be overcast. Low-cloud pixels are all those having values of $\rho > \rho_t$ and $T > T_\varepsilon(\rho, T_{12})$. The temperature T_{12} corresponds to an altitude of 2 km. Similarly, the high-cloud pixels are those having $T \le T_\varepsilon(\rho, T_{23})$, where T_{23} corresponds to 6-km height. All nonclear pixels with temperatures and reflectances between the low- and high-cloud pixels are middle-cloud pixels. An upper boundary, $T_\varepsilon(\rho, T_p)$, is computed to correspond to the tropopause temperature T_p minus 2 K. The 2K subtraction accounts for uncertainty in the tropopause temperature. These cloud-layer boundaries are shown as the solid curves in Figure 4.2-13 and labeled as P_{12}, P_{23},

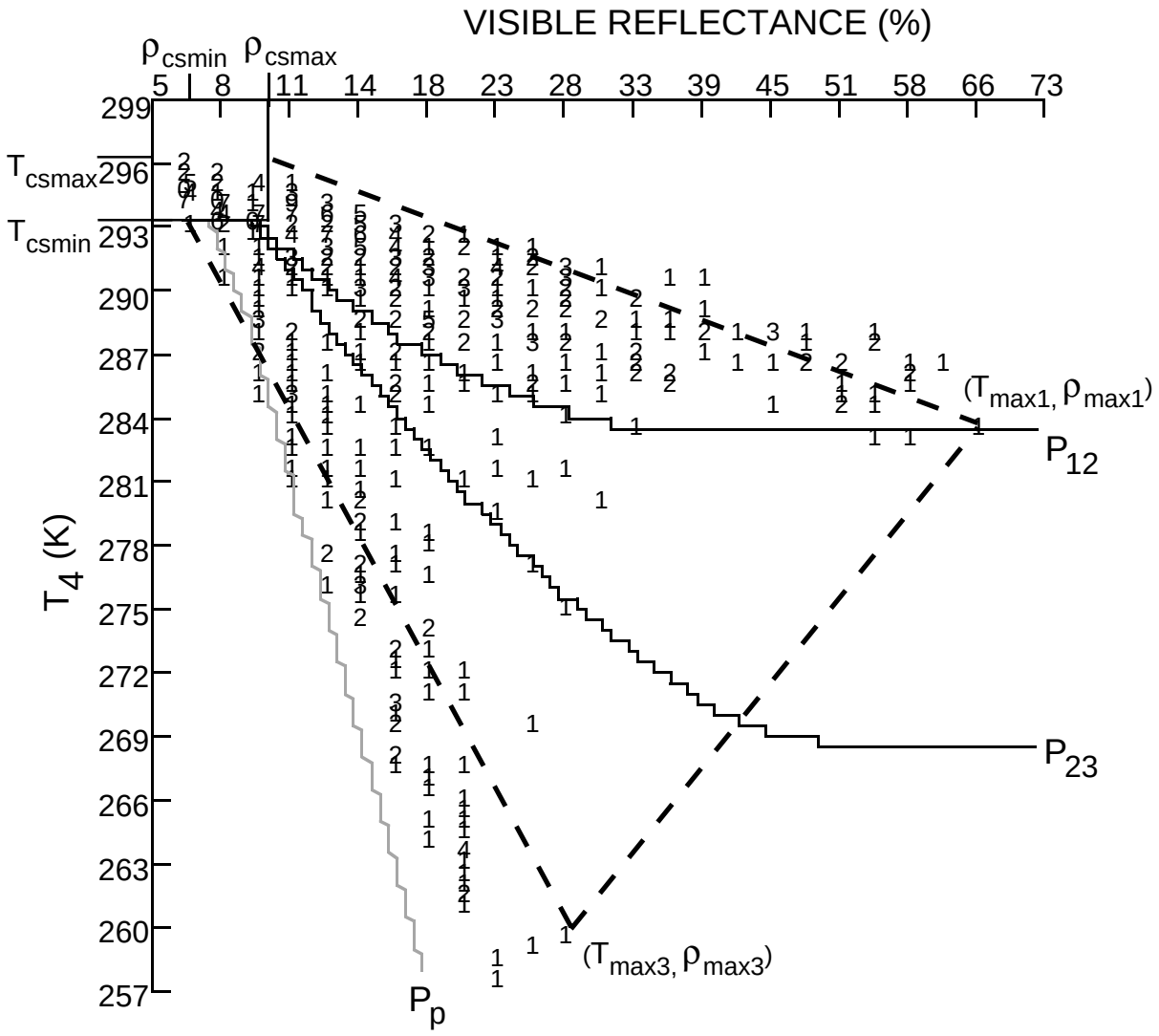

Figure 4.2-13. AVHRR VIS-IR histogram over 17.4°S at 153.3°E at 5.9 UTC, January 18, 1993.

and P_p. Pixels that are darker and colder than the respective reflectances and temperatures defining P_p are designated dark cloud pixels. These pixels are treated in a special manner described below.

The number of pixels in a scene assigned to a given layer, N_k, is

$$N_k = \sum_{ij} n(T_i, \rho_j) \tag{4.2-15}$$

Here, n is the number of pixels having T_i and ρ_j and the limits i and j are defined only for layer k. The temperatures in a given layer are averaged for each visible reflectance. Thus, for ρ_j,

$$T_{kj} = B^{-1}\left[\sum_i \frac{B(T_i)n(T_i, \rho_j)}{N_{kj}}\right] \tag{4.2-16}$$

where

$$N_{kj} = \sum_i n(T_i, \rho_j) \tag{4.2-17}$$

The emittance, $\varepsilon_j = \varepsilon(\rho_j)$ is computed for each reflectance. The value of T_{kj} is substituted for T_ε in (4.2-14) and used with the emittance to solve for $T_{cld}(kj)$. The pressure in the middle of the layer is used in the reflectance parameterization to compute Rayleigh scattering for all clouds in the layer.

If ρ_j is in the dark-pixel area of the histogram, ε_j is indeterminate. It is assumed that dark pixels result from shadowing effects, other finite cloud effects, variations in ρ_{cs}, and inadequacies in the microphysical scattering models. When dark pixels are encountered, high-cloud pixels having greater reflectances are included in the calculation of T_{kj} to raise the mean, combined reflectance to a value of $\rho > \rho_{cs}$ so that ε can be computed. If there are no low- or middle-cloud pixels having $\tau > 1$, then high- or middle-layer pixels having the same temperature as the dark pixels are included in the summation. The summation continues with the next greatest visible reflectance until the mean reflectance is greater than ρ_{cs}. Pixels having temperatures lower than the coldest dim pixels are included in the summation only if the mean value of ρ remains in the dark-pixel area of the histogram. If the summation process does not result in a nondark mean value of ρ, it is assumed that the dark pixels are clear, but shadowed.

If the initial value of $T_{cld}(kj)$ for any kj is less than T_p, then the summation process used for the dark pixels is invoked until $T_{cld}(kj) \geq T_p$. If this condition cannot be satisfied for the data, then it is assumed that the cloud is located at the tropopause. The mean emittance and optical depths are then adjusted to force this solution. Finally, the average temperature for layer k is

$$T_k = B^{-1}\left\{\sum_j \frac{B[T_{cld}(kj)]N_{kj}}{N_k}\right\} \tag{4.2-18}$$

where T_j is the mean temperature for each ρ_j. The standard deviation σ_{Tk} is computed in the standard fashion using the values of T_j. In the exceptions noted above, the index and values of ρ_j are adjusted to reflect the change in summation. No pixel values are ever used twice.

The LBTM cloud-layer definitions, used to associate altitude with the cloud classifications given by surface observers, provide a convenient way to vertically slice up the troposphere. Clouds do not necessarily fall exactly into those altitude ranges, so a cloud deck may straddle the layer boundaries giving the appearance of two layers. Furthermore, high and low layers may overlap and produce radiance pairs that appear to be in the middle layer. To minimize misdetection and to find distinct layers, the following modifications are applied to the LBTM. This procedure is applicable to scenes with horizontal dimensions of 50 km or greater.

To find distinct layers, it is assumed that there is an envelope of temperatures and reflectances that bound the pixels belonging to a given layer. This envelope must account for the variations in both the clear-sky radiances in the scene and the cloud height within the layer. The variations in T_{cs} and ρ_{cs} can be represented by the extreme values. The clear-sky extremes are defined as the coldest and warmest clear temperatures, T_{csmin} and T_{csmax}, respectively, and the smallest and greatest clear-sky reflectances, ρ_{csmin} and ρ_{csmax}, respectively. The respective temperature and reflectance for the brightest pixel in a given layer are T_{maxk} and ρ_{maxk}. The histogram is searched for layers beginning with the highest layer containing an observation. Pixel values falling to the cold and dim side of the line defined by (T_{csmax}, ρ_{csmax}) and (T_{max3}, ρ_{max3}) can be explained by clouds in the high layer. If no pixels are observed on the warm and bright side of this line, then it may be concluded that there is probably only one distinct layer present. This layer is defined by T_{cldk} and σ_{Tk}.

If there are pixels on the warm, bright side then the same process is repeated for the next level down. For midlevel clouds, the line would be given by (T_{csmax}, ρ_{csmax}) and (T_{max2}, ρ_{max2}). If there are low clouds derived from the LBTM and there are pixels warmer and brighter than this new line, then it is concluded that there is a distinct layer of low clouds. These low clouds may be scattered cumulus or a deck of stratus or stratocumulus. If no pixels are observed to the warm, bright side of this line, it is likely that there is a distinct midlevel deck in the scene.

This algorithm is based on the dependence of reflectance and emittance on cloud optical depth. Emittance increases toward unity at a greater rate than reflectance approaches its asymptotic value. This feature produces the curvature seen in the coldest, dimmest pixels in Figures 4.2-8, 4.2-9, and 4.2-12. For a given cloud deck, there will be a spread in the observed temperature for a given reflectance because of the variations in T_{cs}, T_{cld}, and the particle sizes in the cloud. Pixels between the dimmest, coldest curve and the straight line defined above can also be explained by pixels that are partially filled with the upper cloud or by overlap between some lower cloud and the upper cloud. It is necessary to have lower clouds to obtain pixels on the warm, bright side of that line. In other words, the high cloud cannot be that reflective and still be that warm.

To distinguish overlapped pixels from those belonging to a single deck, a similar analysis is applied using lines between the extreme cloud values. Given the presence of both low and high clouds and pixels that fall in the middle layer, it is possible to determine if some of the midlevel pixels are actually overlapped or represent a distinct layer. A line is drawn between (T_{max3}, ρ_{max3}) and (T_{max1}, ρ_{max1}). If there are midlevel pixels to the cold, bright side of this line, then it is highly probable that there is a distinct midlevel deck. Otherwise, the midlevel clouds are probably overlapped high and low clouds.

This process is illustrated in Figure 4.2-13 for data similar to that seen in Figure 4.2-9b. The LBTM found three cloud layers in this histogram. The line extending from (T_{csmin}, ρ_{csmin}) to (T = 259K, ρ = 0.28) indicates that there must be clouds lower than the high-cloud deck. Similarly, the line from (T_{csmax}, ρ_{csmax}) to (T = 284K, ρ = 0.66) indicates a distinct low layer. The lack of pixels brighter than those defined by the line (T = 259K, ρ = 0.28) – (T = 284K, ρ = 0.66) suggests that the pixels in the middle layer do not form a distinct layer. Instead, they are formed by the overlap of the high and low layers.

If there are two layers in adjacent levels or if there is only one distinct layer *k*, but there are some pixels in layer *k–1*, then the cloud temperatures are compared to determine if they are part of the same cloud deck. As in the spatial coherence method, the cloud deck is allowed to have a finite thickness or altitude range. This permitted layer range ΔT_{lcld} varies with height because, in a given system, high cloud tops tend to vary over a greater vertical range than low clouds and retrieved high cloud altitudes are subject to more error than low clouds. Marine boundary layer cloud heights, for example, can be determined to within a few hundred meters (e.g., Minnis et al., 1992), while the typical instantaneous error in the derived thin cirrus heights is ~±1 km (e.g., Minnis et al., 1993). For low clouds, i.e., $T_{cld} >$ 280K, ΔT_{lcld} = 2 K. For high clouds, i.e., $T_{cld} <$ 220 K, ΔT_{lcld} = 6 K. In between these extremes,

$$\Delta T_{lcld} = 2 + 0.67(280 - T_{cld}) \tag{4.2-19}$$

The allowed temperature range bounds the layer values. Thus, if $2\sigma_{Tk} > \Delta T_{lcld}$, then the layer is too diffuse to be designated as a distinct layer. If, however, $2\sigma_{Tk}$ and $2\sigma_{Tk-1}$ are both less than ΔT_{lcld}, then it may be possible to combine the layers. The layers are combined if $T_{k-1} < T_k + 2\sigma_{Tk}$ or if $T_k > T_{k-1} - 2\sigma_{Tk-1}$ and the resulting standard deviation is less than $0.5\Delta T_{lcld}$.

Application of this process to the scatter plots in Figure 4.2-8 would yield single low-level decks for [1,1] and [2,1], and low and high decks with overlapped pixels for the remaining plots. In Figure 4.2-12, the technique would identify a low and a high deck for [1,1], a mid and high deck for [1,2], a low deck for [1,3], a mid and high deck for [2,10] a high deck for [2,2], and possibly a high deck for [2,3]. The high layers in [1,3], [2,2], and [2,3], the midlayers in [2,2] and [2,3] and the low layer in [2,3] may be too diffuse to pass the layer bounds test although they would pass the simple linear tests. Some layering of the high clouds in [1,3], [2,2], and [3,3] may be detectable with a greater vertical resolution of layers rather than the three used here. However, these scenes may contain convective clouds in various stages of development so that no extensive layers exist. Figure 4.2-14 shows an example of a diffuse situation over the tropical Pacific. The low-mid, mid-high, tropopause, and clear boundaries are drawn to illustrate how the histogram is sliced for a convective case. Application of the technique would yield only one distinct cloud layer in the middle levels with T_2 = 278.6 K. The high layer would not satisfy the

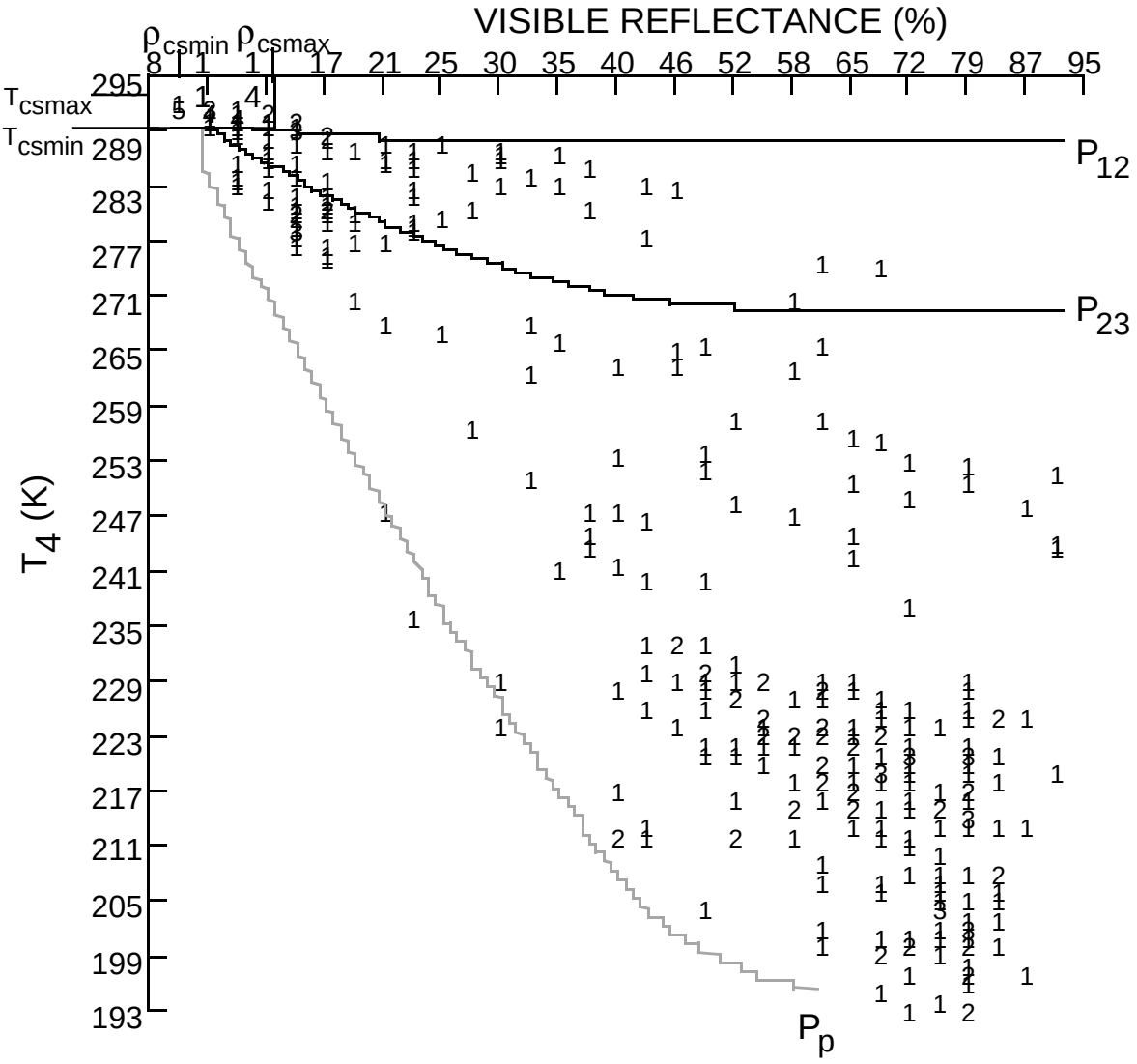

Figure 4.2-14. AVHRR VIS-IR histogram over 10.7°S at 143.2°E at 5.9 UTC, January 18, 1993.

temperature range rules. Some low-cloud pixels near the clear boundary would not constitute a layer because they fall to the cold, dim side of the mid-cloud ρ_{max} line.

For scenes containing more than one layer, it is possible to estimate which pixels are overlapped and which belong to a single layer. Given T_k and σ_{Tk} for layer k, the pixels that belong to the layer are those enveloped by the two curves defined by the model calculations of T and ρ for a range of optical depths. The computations use (T_{csmax}, ρ_{csmax}) for the clear conditions and $T_k + 2\sigma_{Tk}$ as the cloud temperature to determine the curve for the warm side of the cloud deck and (T_{csmin}, ρ_{csmin}) for the clear conditions and $T_k - 2\sigma_{Tk}$ as the cloud temperature to determine the cold curve. Pixels having values of T and ρ between those two curves are assigned to the layer. Figure 4.2-15 shows an example of a three-layer case. The boundary lines are shown as before with a crude approximation of the envelopes for each layer. The envelope overlap near the clear boundaries is typical, but will be somewhat diminished when the actual calculations are applied. The T and ρ for each pixel in the envelope overlap are compared to the central curve of the envelopes. This central curve is defined by T_k and (T_{cs}, ρ_{cs}). The pixel is assigned to the layer for which the difference between T and $T_k(\rho)$ is minimal. The pixels that fall between the envelopes are considered to be overlapped pixels.

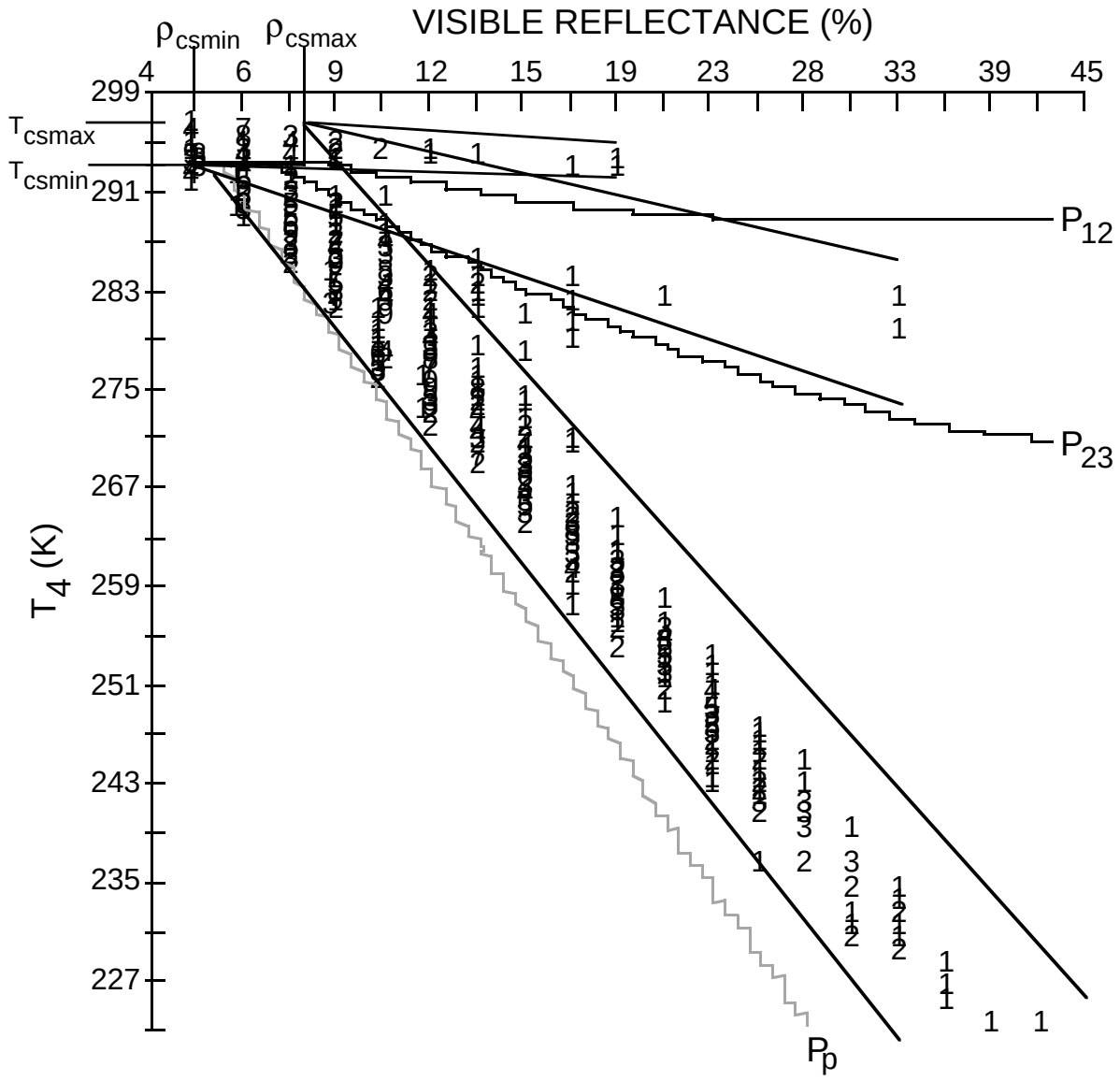

Figure 4.2-15. AVHRR VIS-IR histogram over 13.3°S at 149.4°E at 5.9 UTC, January 18, 1993.

This approach to cloud layering can detect more cloud layers than the spatial-coherence technique. It cannot detect three layers unless the reflectance of the middle layer exceeds that of either the low or high layer. The increased detectability may raise the level of uncertainty in the cloud layer properties. This bispectral approach is currently under development and will be altered to accommodate additional layers. The allowed layer temperature range, interpretation of the overlapped pixels, and techniques for defining the range in clear-sky temperature and reflectance are among the issues that are being examined.

4.2.3.2. Nighttime Layer Pressure Retrieval

At night, a different approach is needed. Figure 4.2-16a shows T_4 and the AVHRR channel 3 (3.7 μm) brightness temperatures T_3 for a layer of altostratus clouds over an area in the tropical Pacific. The value of T_{cs4} is ~293K. The brightness temperature differences $BTD_{3\text{-}4}$ for channels 3 and 4, plotted

against T_4 in Figure 4.2-16b, are more informative. For a given value of T_{cld}, $BTD_{3\text{-}4}$ increases as the optical depth increases up to a value of $\tau \sim 4$. As τ continues to increase, $BTD_{3\text{-}4}$ decreases rapidly until it is less than the clear-sky value. Thus, whenever $BTD_{3\text{-}4}$ for cloudy pixels is less than the clear value, a nearly opaque cloud is indicated. The variation in $BTD_{3\text{-}4}$ arises from variations in T_{cs}, T_{cld}, and particle size. If there is a cluster of nearly opaque pixels around a given value of T_4, it is highly probable that a layer exists at T_4. The methods for determining these layers are the same as prescribed for the daytime case. The low, middle, and high boundaries are established for an optically thick cloud (e.g., $T_{12} = T[z = 2\ km]$ for all values of T_3). The values of T_k and σ_{Tk} are computed using only the pixels having $BTD_{3\text{-}4}$ less than the clear-sky value. The same criteria applied during the daytime are used at night for defining a layer and combining adjacent layers. In the case of Figure 4.2-16b, a layer would be determined at ~258K.

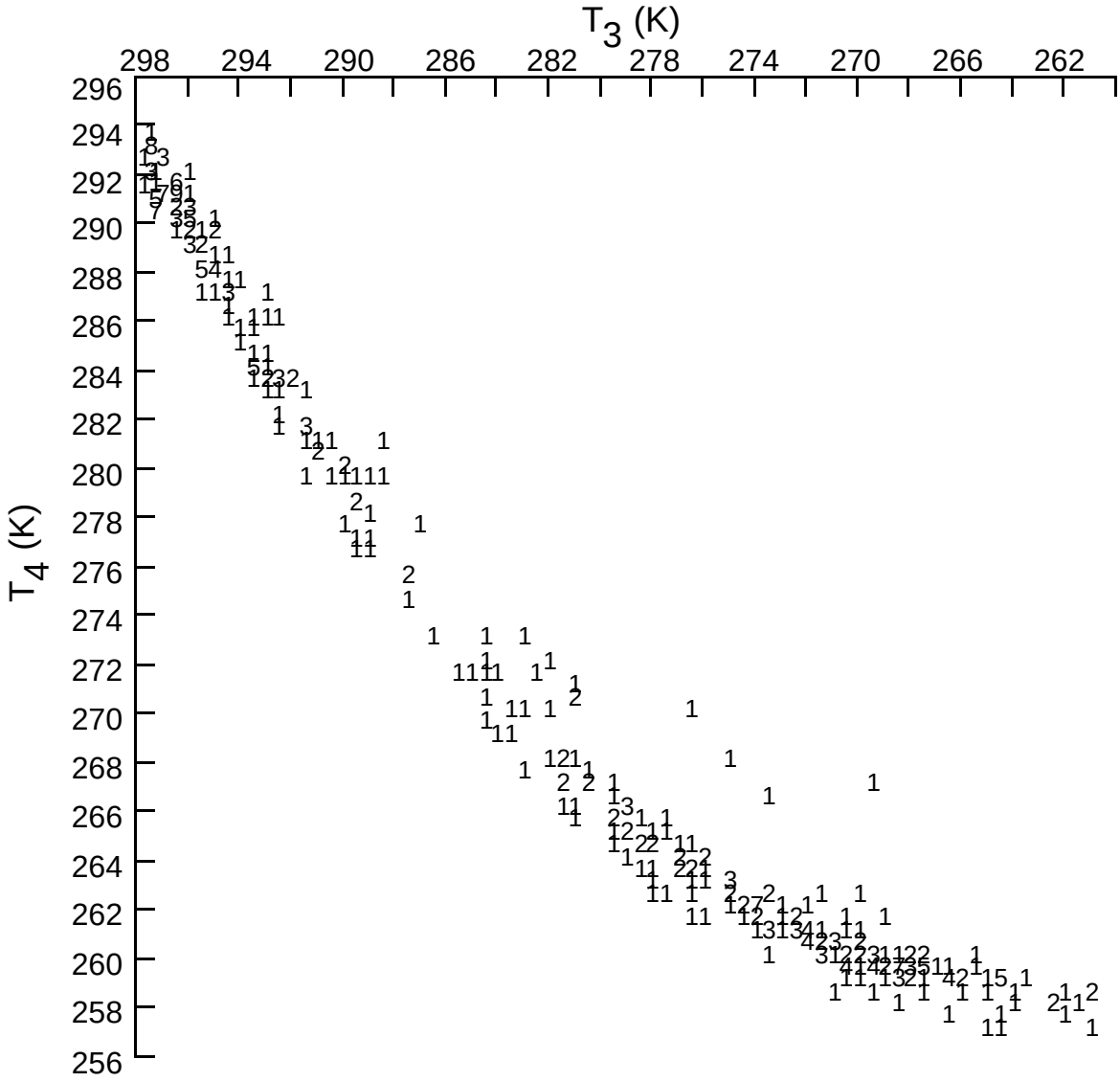

Figure 4.2-16a. AVHRR NIR-IR histogram over 5.9°S at 133.6°E at 18.8 UTC, January 26, 1993.

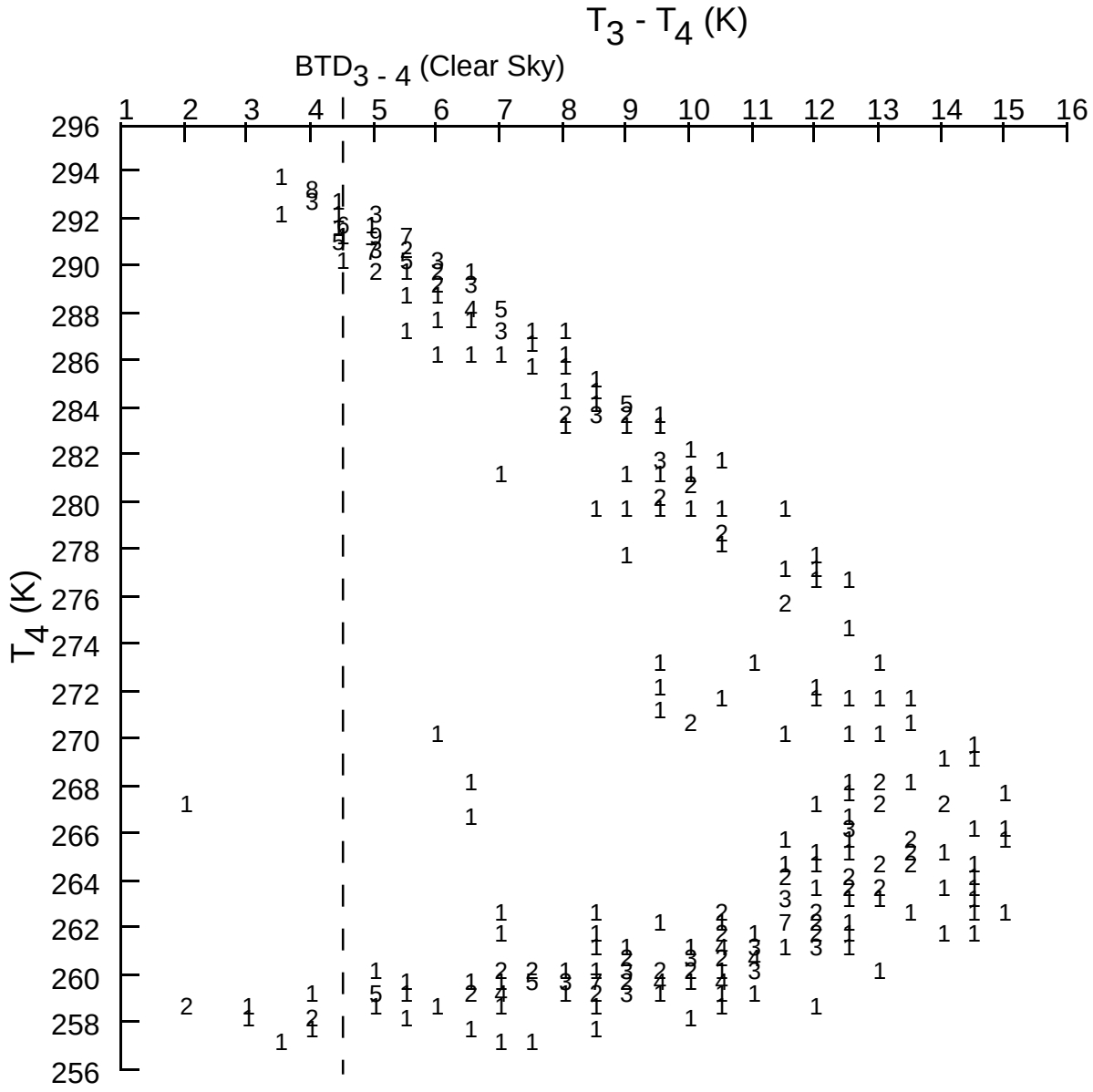

Figure 4.2-16b. AVHRR BTD-IR histogram over 5.9°S at 133.6°E at 18.8 UTC, January 26, 1993.

A layer analysis of the histogram in Figure 4.2-17 would yield a layer near 221 K. The solid line in Figure 4.2-17 corresponds to a parameterization calculation of $BTD_{3\text{-}4}$ using a cirrostratus microphysical model, T_{cs4} = 293.5K, and T_{cld} = 221K (see section 4.3 for details). The model fit is consistent with a single layer of clouds having relatively uniform particle sizes. The more complex histogram in Figure 4.2-18 is typical of a two- or three-layer system. The clear portion of the scene is at approximately 291 K; a distinct middle layer is found at 273 K, and a diffuse high layer is found near 228 K. An additional low layer may be at ~288 K. This combination of clear, single-layer, and overlapping layers would probably only yield a single layer at ~273 K. The high-cloud layer would be too diffuse to pass the temperature range tests using T_{cs} as the background temperature. Because most of the high-cloud pixels are probably overlapping middle-cloud pixels, the background temperature should be the middle-cloud temperature. The result would be a high cloud at ~228 K.

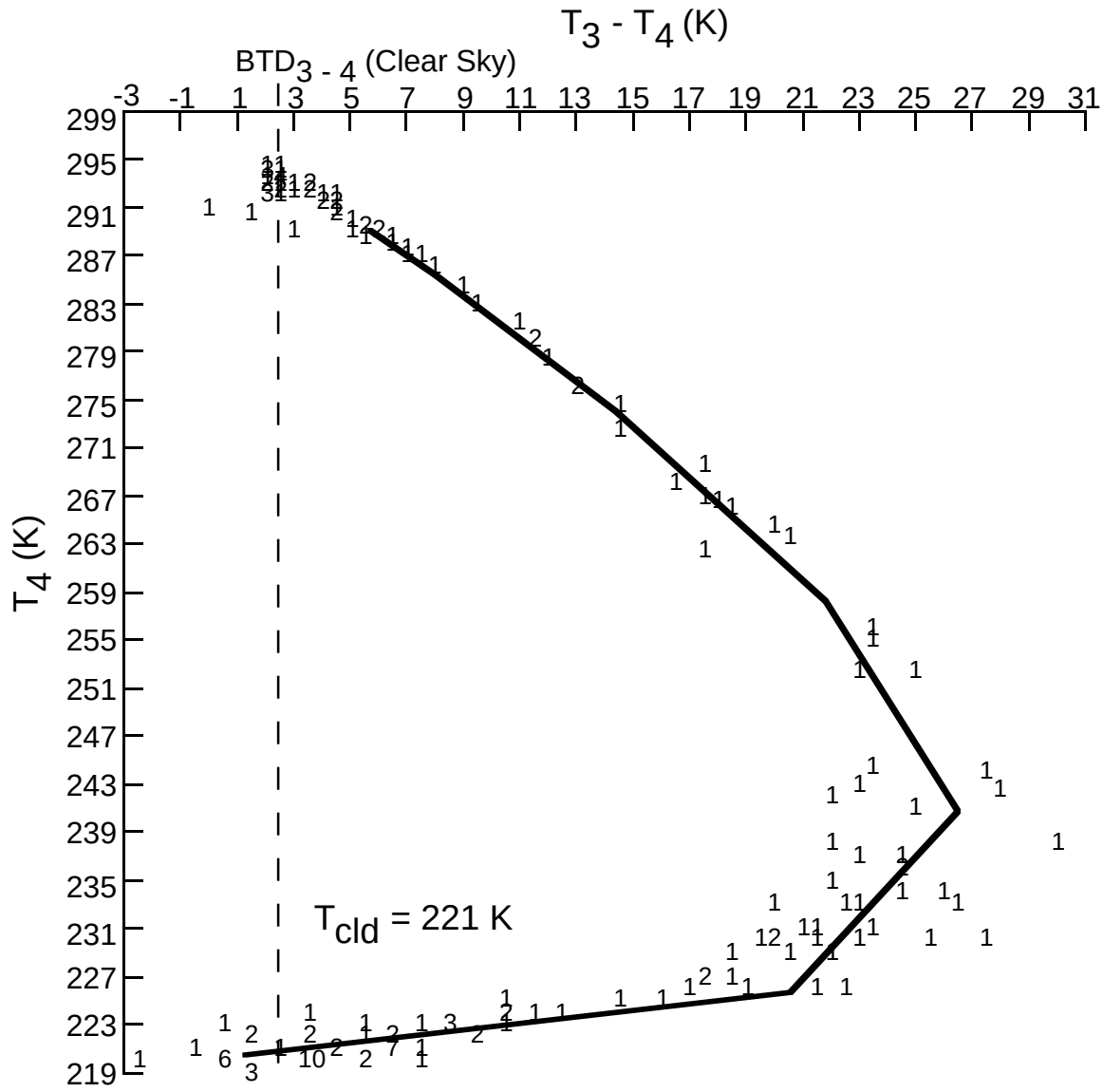

Figure 4.2-17. AVHRR BTD-IR histogram over 7.1°S at 171.3°E at 16.3 UTC, January 30, 1993.

The examples shown here suggest that layers can be identified at night using a bispectral histogram approach. This method is currently under development. Issues that are being addressed include the detection of overlapped pixels, the determination of the appropriate background temperature, prescription of layer envelopes based on assumptions about particle size, detection of layers with no opaque pixels, and the determination of layers in overlapped conditions.

4.2.3.3. Practical Considerations

For CERES, the LBTM histogram will be divided into six areas: clear, low (surface to 700 hPa), lower middle (700–500 hPa), upper middle (500–300 hPa), and high (<300 hPa), and the dark pixel area. The CERES LBTM will require the input variables: clear-sky radiances and their standard deviations for each channel, vertical profiles of temperature, surface type, pixel radiances, surface elevation, and ozone optical depth at 0.65 μm. The output comprises the number of distinct layers, the means and standard deviations for τ_k and T_k, and an index indicating whether it is overlapped or not. The methodologies described in this section will be validated using several different approaches. The layer cloud

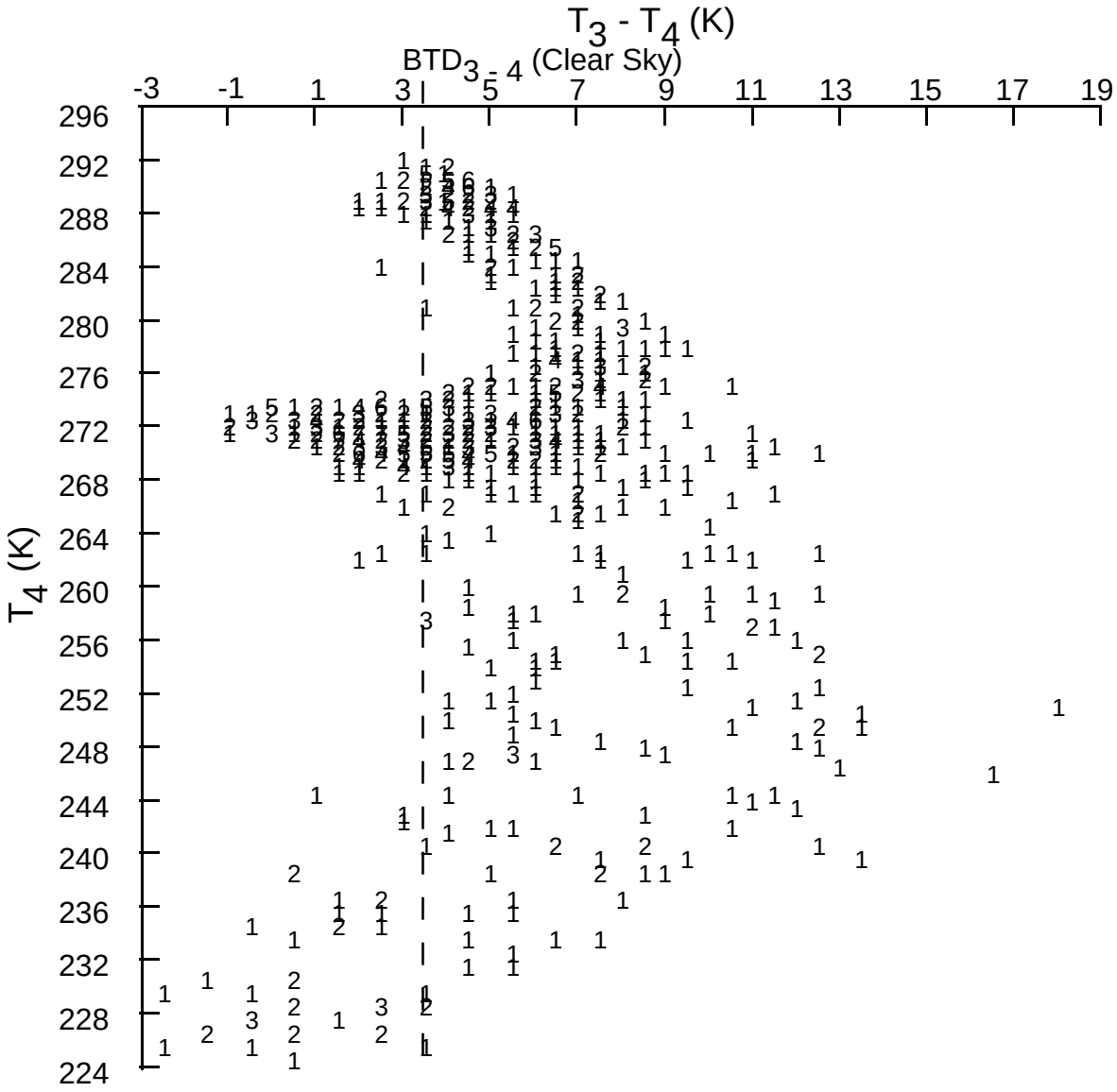

Figure 4.2-18. AVHRR BTD-IR histogram over 4.3°S at 134.7°E at 18.8 UTC, January 26, 1993.

properties will be compared to those derived from the other satellite-retrieval methods to determine how much additional information can be gained by applying this methodology. Aircraft and surface lidar and radar data will be used to verify the detection of layers and their altitude determination. These validation efforts will use historical FIRE and ECLIPS datasets as well as active remote sensing data from ARM and future FIRE observations. Such field data taken over a wide variety of cloud types are essential for verification and development of these layer-detection techniques.

4.2.4. The CO_2 Slicing Method

4.2.4.1. Introduction

The CO_2 slicing methods (e.g., McCleese and Wilson, 1976; Smith and Platt, 1978; Chahine, 1974) have been shown to provide an accurate means of inferring cirrus cloud altitude from passive infrared radiance measurements. The methods take advantage of the fact that each of the sounding channels within the 15-μm CO_2 band have varying opacity to CO_2, thereby causing each channel to be sensitive

to a different layer in the atmosphere. The techniques have been shown to be effective for single-layered, nonblack, mid- to high-level clouds such as cirrus, but are generally applied operationally to any given cloud occurrence. The algorithms are most accurate for clouds that occur in a single, well-defined layer, or for multilayered cloud cases in which the uppermost cloud layer is nearly black. The derived cloud pressure is expected to be near cloud center for optically thin clouds (those with extinction optical depths less than 1). The cloud pressure is expected to decrease to cloud top for more nearly opaque cloud when the extinction optical depth is greater than 1.

This algorithm calculates cloud top pressure, p_{cld}, and effective cloud amount, εC (emittance ε times cloud fraction C), given one or more pairs of 15-μm narrowband radiances. The method relies upon having significant pressure level differences between the peaks of the weighting functions for a given pair of channels. The algorithm specification includes suggested strategies for handling:

1. Temperature inversions (ambiguity in p_{cld})
2. Lack of sensitivity in the weighting functions
3. Consistency in multichannel retrievals
4. Various problems relating to instrument noise, transmission function errors, and input data errors

This algorithm has been applied to data from the High Resolution Infrared Radiation Sounder (HIRS/2, henceforth HIRS for simplicity) (Wylie and Menzel, 1989; Menzel et al., 1992; Wylie et al., 1994), the Geostationary Operational Environmental Satellite (GOES) VISSR (Visible Infrared Spin Scan Radiometer) Atmospheric Sounder (VAS) (e.g. Menzel et al., 1983), and most recently to the High Resolution Interferometer Sounder (HIS) (Smith and Frey, 1990). The Moderate Resolution Imaging Spectroradiometer (MODIS) (King et al., 1992) under development for the Earth Observing System (EOS) has four channels in the 15-μm region that are similar to the HIRS channels. The central wavenumbers and other characteristics of the appropriate channels for the HIRS and MODIS instruments are provided in Table 1. Error analyses based upon the CO_2 slicing method have been reported by Wielicki and Coakley (1981), Menzel et al. (1992), and Baum and Wielicki (1994). Sources of error for this algorithm will be discussed in greater detail later in this document. Retrieval errors will arise from instrument noise, errors in temperature and humidity profiles, errors in the clear-sky radiance, geometrically thick but optically thin clouds, radiative transfer calculation assumptions, and the presence of more than one cloud layer in the field-of-view (FOV).

4.2.4.2. Basic Equations and Derivations

The clear-sky spectral radiance $I_{cs}(\nu^i, p_s)$ for a black surface (surface emissivity, $\varepsilon_s^i = 1$, i is channel number) is given by

$$I_{cs}(\nu^i, p_s) = B(\nu^i, T_s)t(\nu^i, p_s) + \int_{P_s}^{0} \frac{dt(\nu^i, p)}{dlnp} B[\nu^i, T(p)]dlnp \qquad (4.2\text{-}20)$$

where $B(\nu^i, T)$ is the Planck radiance at temperature T, ν^i is the wavenumber of channel i, $t(\nu^i, p)$ is the transmission from atmospheric pressure level p to the satellite at $p = 0$, and the subscripts s and cs denote surface and clear-sky, respectively. If the cloud is opaque (cloud emissivity, $\varepsilon_{cld}^i = 1$) at wavenumber ν^i and completely fills the FOV, the radiance for an overcast black cloud (ob) at pressure level p_{cld} is given by

$$I_{ob}(\nu^i, p_{cld}) = B(\nu^i, T_{cld})t(\nu^i, p_{cld}) + \int_{p_{cld}}^{0} \frac{dt(\nu^i, p)}{dlnp} B[\nu^i, T(p)]dlnp \qquad (4.2\text{-}21)$$

Table 4.2-1. HIRS and Anticipated MODIS Channels, Central Wavelengths, Principal Absorbing Components, and Approximate Pressure Level Corresponding to the Peak in the Individual Channel Weighting Functions; Central Wavelengths and Weighting Function Peaks May Change Slightly for Each Instrument.

Instrument	Channel number	Central wavelength, μm	Principal absorbing component	Approximate peak in weighting function, hPa
HIRS	4	14.21	CO_2	300
HIRS	5	13.95	CO_2	500
HIRS	6	13.66	CO_2; H_2O	750
HIRS	7	13.34	CO_2; H_2O	900
HIRS	8	11.10	H_2O	Surface
MODIS	31	11.03	H_2O	Surface
MODIS	32	12.02	H_2O	Surface
MODIS	33	13.335	CO_2; H_2O	900
MODIS	34	13.635	CO_2; H_2O	750
MODIS	35	13.935	CO_2	500
MODIS	36	14.235	CO_2	300

The theoretical upwelling radiance I for a partially cloud-filled FOV is given by

$$I(\nu^i, p_{cld}, \varepsilon^i_{cld} C) = I_{cs}(\nu^i, p_s) + \varepsilon^i_{cld} C[I_{ob}(\nu^i, p_c) - I_{cs}(\nu^i, p_s)] \quad (4.2\text{-}22)$$

In this formulation, the cloud emittance ε^i_{cld} of channel i is multiplied by the cloud fractional coverage C, and the quantity $\varepsilon^i_{cld} C$ is referred to as the effective cloud amount or effective cloud emittance in the literature.

4.2.4.2.1. Transmittance functions. The calculation of the transmission functions used to generate the theoretical upwelling radiances are based on a model developed by McMillin and Fleming (1976) and used by Weinreb et al. (1981) for HIRS transmittance calculations. Eyre and Woolf (1988) developed a newer model primarily for work with microwave channels. When the Eyre and Woolf (1988) model was tested on HIRS channels, it was found to have poor accuracy for channels with strong water vapor absorption. This shortcoming was addressed in the model reported by Eyre (1991), which improves the treatment of water vapor and has the added benefit of providing code that is much easier to vectorize than the model used by Weinreb et al. (1981). The model currently used is based on Eyre (1991) with code developed initially by Woolf (personal communication, 1993).

For HIRS analysis, the transmittance model is evaluated at 40 discrete pressure levels (0.1, 0.2, 0.5, 1, 1.5, 2, 3, 4, 5, 7, 10, 15, 20, 25, 30, 50, 60, 70, 85, 100, 115, 135, 150, 200, 250, 300, 350, 400, 430, 475, 500, 470, 620, 670, 700, 780, 850, 920, 950, and 1000 hPa). For a midlatitude spring/fall temperature profile shown in Figure 4.2-19a, transmittance profiles for HIRS 15-μm channels 4 through 7 are shown in Figure 4.2-19b. Channels 4 and 5 have extremely low transmittances at the surface, showing that these channels are relatively insensitive to errors in clear-sky temperature. Channels 6 and 7 have

transmittances greater than 10% near the surface and are more sensitive to surface temperature than channels 4 or 5. Weighting functions for HIRS channels 4 through 8 are shown in Figure 4.2-20.

For MODIS 15-μm radiometric data analysis, it is anticipated that the transmission model will be discretized at 50-hPa increments in the troposphere, and have an additional surface term for cases in which the surface pressure is greater than 1000 hPa. There has been some discussion as to whether 25-hPa pressure increments will be necessary.

4.2.4.3. Radiance Ratio Method

Cloud-top pressure may be determined using the radiance ratio method, as discussed in Smith and Platt (1978), Wylie and Menzel (1989), Smith and Frey (1990), Menzel et al. (1983), and Wielicki and Coakley (1981). The change in radiance at a particular wavenumber caused by the presence of cloud is called the cloud signal. In the radiance-ratio method, a ratio is taken of the cloud signals for two channels spaced closely in wavenumber. For two spectral channels at wavenumbers ν^i and ν^j that are looking at the same FOV, the ratio for a single cloud layer is derived as

$$G(p_{cld}) = \frac{I_{meas}(\nu^i) - I_{cs}(\nu^i)}{I_{meas}(\nu^j) - I_{cs}(\nu^j)} = \frac{I_{ob}(\nu^i, p_{cld}) - I_{cs}(\nu^i, p_{cs})}{I_{ob}(\nu^j, p_{cld}) - I_{cs}(\nu^j, p_{cs})} \tag{4.2-23}$$

where G is the ratio of cloud signal for two different channels and I_{meas} (ν^i) and I_{meas} (ν^j) denote the measured radiance of channels i and j. We make the assumption that the emittances are the same for both channels. The function G is independent of both cloud opacity and effective cloud amount. However, G is dependent on the weighting function of the two channels, the cloud height, and the atmospheric temperature profile.

4.2.4.4. Root-mean-square (RMS) Method

The implementation of the rms method requires a knowledge of temperature and humidity profiles. The rms radiance difference I_{rms} for N channels (Chahine, 1974; Wielicki and Coakley, 1981) is determined from

$$I_{rms}(p_{cld}, \varepsilon^i_{cld}C) = \left\{ \sum_1^N [I^i_{meas}\ (\nu^i) - I^i(\nu^i, p_{cld}, \varepsilon^i_{cld}C)]^2 \right\}^{1/2} \tag{4.2-24}$$

where I_{rms} is the rms radiance and $I^i(\nu^i, p_{cld}, \varepsilon_{cld}{}^iC)$ is determined from (4.2-22). For multilayer cloudiness, the retrieved cloud pressure errors will be the result of using a clear-sky radiance instead of the radiance of a lower cloud layer to compute the theoretical upwelling radiances when more than one cloud layer is present in an FOV. The atmosphere between 200 and 950 hPa is divided into 25-hPa intervals for the rms calculations. Thus, the derived cloud pressure will correspond to the rms minimum at a predefined interval.

The rms method, as stated in (4.2-25), has no provision for weighting the cloud signal from the various channels. The cloud signal for any particular channel increases with surface transmission so that the largest cloud signal will be recorded for the channel whose weighting function peaks closest to the surface, and the smallest cloud signal for the channel whose weighting function peaks farthest from the surface. The rms method as currently applied tends to weight the results toward the channels with greater transmittance.

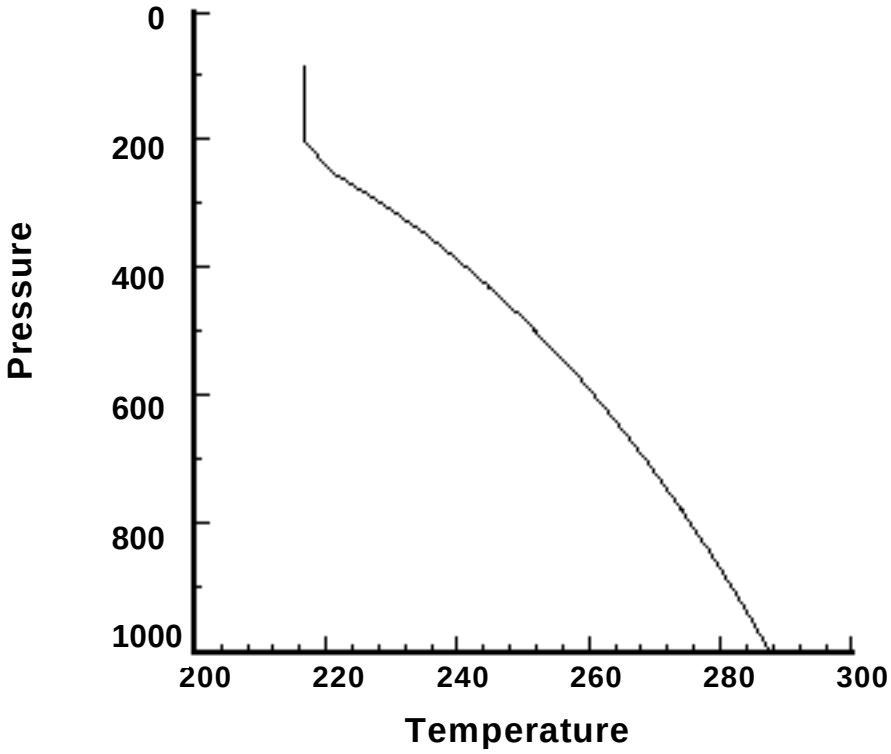

(a) Average midlatitude temperature profile.

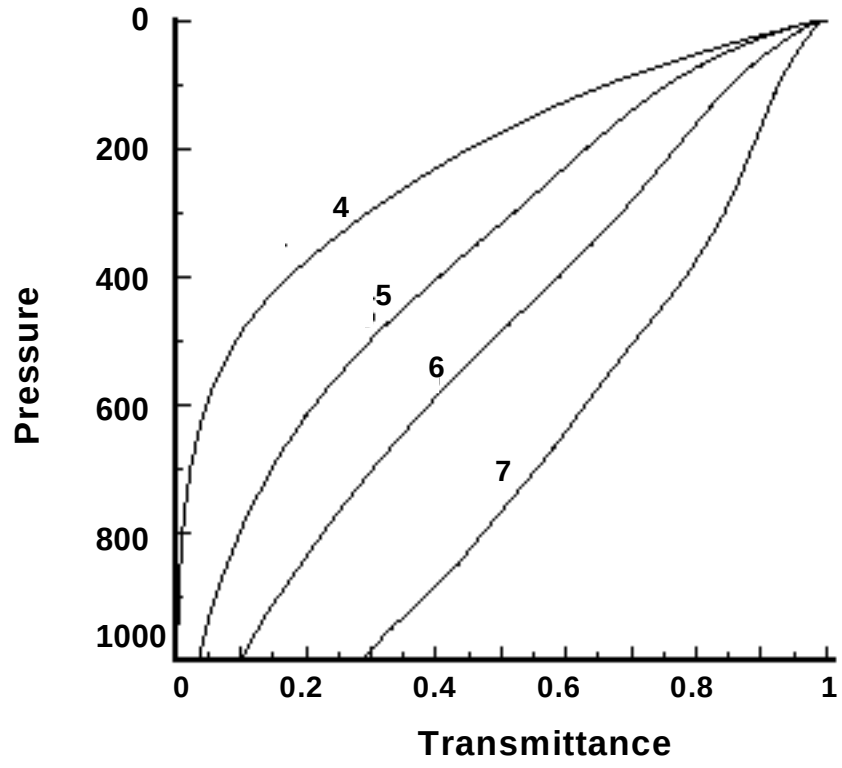

(b) NOAA-11 HIRS transmittances for channels 4, 5, 6, and 7.

Figure 4.2-19. Temperature and transmittance profiles.

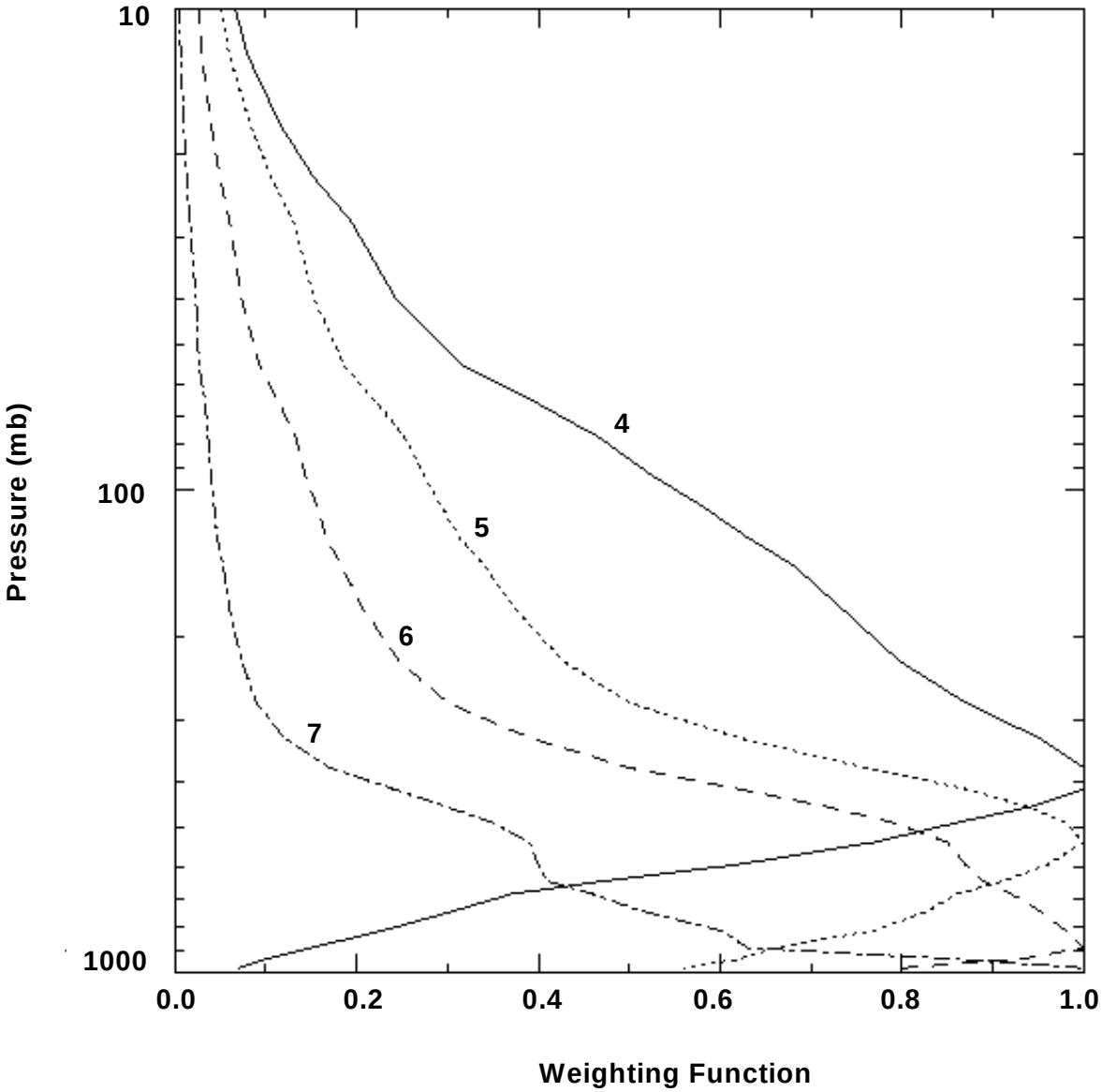

Figure 4.2-20. NOAA-11 HIRS weighting function *dt/d ln P* for channels 4, 5, 6, and 7 for nadir viewing conditions.

4.2.4.5. Calculation of Effective Emittance

Once a cloud height has been determined, an effective cloud amount (also referred to as effective emittance) can be evaluated from the infrared window channel data (usually 11 μm). For a single-level cirrus layer, the effective emittance is derived by rearranging (4.2-23):

$$\varepsilon C = \frac{I(\nu^i, p_c) - I_{cs}(\nu^i, p_s)}{I_{ob}(\nu^i, p_c) - I_{cs}(\nu^i, p_s)} \tag{4.2-25}$$

When the effective emittance is less than unity, the sensor may be observing broken cloud ($C < 1$; $\varepsilon_{cld} = 1$), overcast transmissive cloud ($C = 1$; $\varepsilon_{cld} < 1$), or broken transmissive cloud ($C < 1$; $\varepsilon_{cld} < 1$). With a HIRS FOV of ~18 km at nadir, it is not reasonable to assume that the cloud completely covers the field of view except for large scale synoptic regimes. For the MODIS 1 km × 1 km pixel size, we can assume that high clouds fill the field of view ($C = 1$) so that we obtain a direct estimate of ε using (4.2-30)

or (4.2-31). For the large HIRS footprint, C is determined from AVHRR higher resolution data, assuming $C = 1$ for the AVHRR pixel.

4.2.4.6. Estimation of Clear-Sky Radiance

To calculate the G function for the single cloud-layer case, an estimate must be determined for the representative clear-sky radiance appropriate for the FOV. Clear-sky radiance/brightness temperature estimates are to be used from the CRH ancillary data set.

4.2.4.7. Error Estimates for Cloud Property Retrieval

Retrieval errors will arise from instrument noise, errors in temperature and humidity profiles, errors in the clear-sky radiance, geometrically thick but optically thin clouds, radiative transfer calculation assumptions, and the presence of more than one cloud layer in the FOV. Because all of these issues have been reported in the literature, a brief summary will be presented here.

4.2.4.7.1. Errors associated with the assumption of constant emissivity. Spectrally close channels are used to minimize differences in the real and imaginary parts of the index of refraction for ice crystals and water droplets. Calculations by Jacobowitz (1970) indicate that negligible errors occur for the CO_2 channels between 13.3 and 14.2 μm for water and/or ice cloud determinations. This phenomenon is not deemed to be an error source in the CO_2 slicing algorithm.

4.2.4.7.2. Errors associated with the assumption of a thin cloud layer. The CO_2 slicing algorithm assumes that all of the radiative effects of the cloud occur as if the cloud were a thin layer at a single temperature. This makes the mathematics tractable. If the methodology to calculate radiative properties of a nonopaque cloud were to include a cloud term where the cloud has finite depth, then knowledge of the vertical structure of the cloud would be required. There are an infinite variety of combinations of cloud depths and vertical combinations that could produce the same integrated radiative signature; a unique solution is not possible. Any initial assumption of cloud structure biases the cloud top and bottom solution derived in the radiative transfer formulation.

Wielicki and Coakley (1981) discussed the consequences of the thin-layer cloud approximation. They concluded that the algorithm solution for cloud-top pressure would be near the center of the cloud for thin clouds and near the top of the cloud for opaque clouds. For an optically thick cloud, the equation would yield the correct cloud-top pressure. For an optically thin cloud, however, the radiative effects of the cloud are forced into one layer. This is similar to a center of mass concept. The algorithm solution will be close to the radiative center of the cloud. The retrieved cloud-top pressure is somewhere between the cloud top and its center, varying with the density of the cloud.

Cirrus height errors are also discussed in Wylie and Menzel (1989), where comparisons were made to cloud tops measured by lidars and by the stereo parallax observed from the images of two satellites at two different viewing angles. In the lidar comparison, the VAS-inferred cloud-top pressure over an observation area was compared to the highest lidar observation in the same area. The clouds had to be radiatively thin for the lidars to see through to the tops without complete signal attenuation. Definition of a single cloud top was often difficult within a cloud layer; the lidar heights varied considerably (by more than 50 hPa) from one cloud element to another in the same cloud layer. On the average, the VAS P_{cld} was found to be approximately 70 hPa larger (lower cloud altitude) than the lidar-derived cloud-top heights. The CO_2 slicing algorithm was sensing the mean height; the VAS heights were comparable to the lidar cloud-top heights to within half the cloud thickness. In the comparisons to stereo parallax measurements for thin transmissive clouds, the VAS heights showed little bias. It was often difficult to measure parallax for thin transmissive clouds, as they appeared fuzzy with poorly defined boundaries in the images. Because the image of the clouds is more indicative of the center of the diffuse cloud mass than its outer boundaries, the parallax method is sensitive to the radiative center of mass rather than the

physical tops of these clouds. Thus, in these intercomparisons of actual measurements, the retrieved P_{cld} values were found to be within the accuracy suggested by theoretical considerations.

4.2.4.7.3. Errors associated with the assumption of a lower cloud layer. McCleese and Wilson (1976) have shown that the retrieved cloud height for the case of multiple cloud layers is a weighted average of the cloud heights actually present. They performed numerical simulations of cloud configurations for the Nimbus-5 sounding channels. However, no quantitative information was provided to aid in estimating the errors in cloud pressure retrieval one should expect for common multilevel cloud situations, like cirrus over stratus. Menzel et al. (1992) presented an error analysis performed for the GOES VAS. The errors in high-cloud pressure retrieval associated with the presence of a lower cloud layer were found to result in a maximum error in retrieved upper-cloud pressure of approximately 100 hPa. The GOES VAS has three CO_2 sounding channels that are similar to those of HIRS, but HIRS has more sounding channels.

Baum and Wielicki (1994) presented multilevel cloud-retrieval errors for the HIRS instrument. The effect of opaque lower-cloud contamination at 850 mb on cloud pressure retrieval for a HIRS FOV is shown in Figure 4.2-21 for four two-channel combinations implementing the ratio method. Calculations are performed for a range of P_{uc} where the subscript *uc* represents the upper cloud layer, ranging from 250 to 850 mb and a range of $\varepsilon_{uc}^{i} C_{uc}$ between 0.1 and 1.0. The implementation of either the rms or the ratio methods will result in a single derived cloud pressure for a chosen FOV and channel combination. For the case in which a FOV has two distinct cloud layers, the difference in retrieved minus actual cloud pressure is positive in all cases. A positive difference means that the retrieved upper-cloud height is lower than the actual upper-cloud height. An error in retrieved cloud pressure results in an error in the calculation of $\varepsilon_{uc}^{i} C_{uc}$. For the pressure errors presented in Figure 4.2-21, corresponding $\varepsilon_{uc}^{i} C_{uc}$ errors are shown in Figure 4.2-22 for the same conditions. The retrieved $\varepsilon_{uc}^{i} C_{uc}$ are calculated by using the lowest sounding channel of the pair of channels chosen for the ratio method. The error in $\varepsilon_{uc}^{i} C_{uc}$ is defined to be the retrieved value minus the true value. Because this quantity is positive, the retrieved value will be too high for cases in which there is lower-cloud contamination in a HIRS FOV.

The conclusions from these studies are as follows. The position of the lower cloud layer affects the accuracy of the height estimate of the upper cloud layer. Opaque clouds located near the surface underneath high cirrus have little effect on the retrieved cirrus P_{cld}. As the low-level opaque cloud increases in height above the surface, and thus has a colder cloud-top temperature, the errors in upper-cloud retrieved P_{cld} increase. The errors in cloud pressure and effective cloud amount caused by the presence of a lower overcast, black cloud layer are greatest for the CO_2 slicing techniques that use the lowest sounding channel and least for those channels whose weighting functions peak higher in the atmosphere. Baum and Wielicki (1994) also found that the errors depend upon the temperature lapse rate between the low-level cloud top and the surface. The retrieved upper-cloud pressure bias increases with increased lapse rate between the low cloud and the surface. The choice of the optimal channel selection depends on the type of study being performed. While the HIRS channels whose weighting functions peak between 700 and 1000 hPa minimize random errors, the use of the sounding channels whose weighting functions peak at 300 to 500 hPa minimize bias errors. For a cloud climatology the bias errors are most critical.

4.2.4.7.4. Errors associated with instrument noise. Instrument noise produces two types of error into the cloud-top pressure retrieval. Random instrument noise leads to an rms error and a bias error. The rms error is a variation of retrieved cloud pressure about the retrieved mean cloud pressure, whereas the bias errors were caused by differences between actual mean and retrieved mean cloud pressures. The primary source of bias is limiting effective cloud amount to the range (0,1) and cloud-top pressure to the range between the surface and the tropopause.

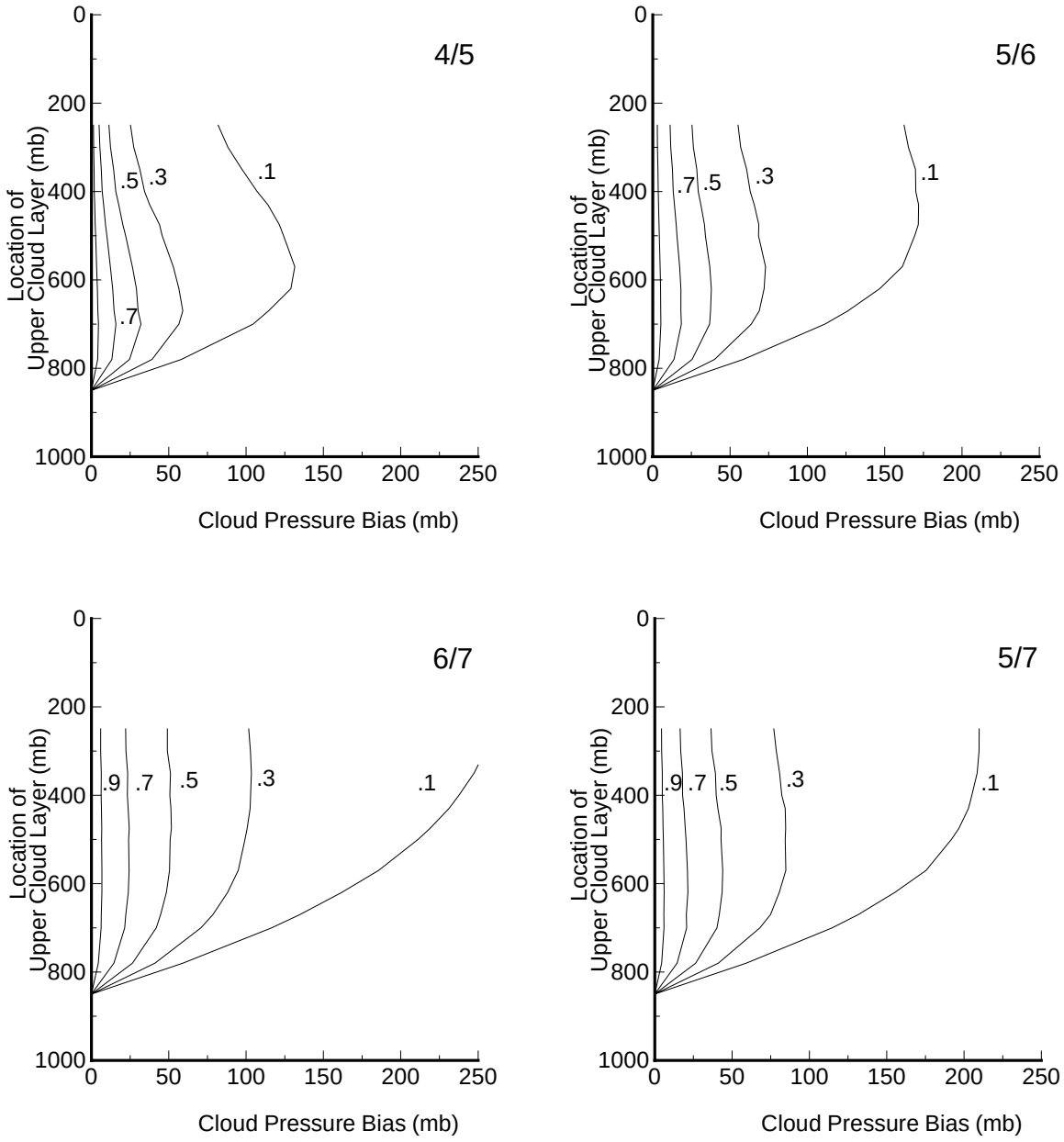

Figure 4.2-21. Multilevel cloud pressure retrieval bias errors (mb) for several $\varepsilon_{uc}C_{uc}$ as a function of the pressure of the upper transmissive cloud layer. Results are presented for the HIRS 4/5, 5/6, 6/7, and 5/7 channel ratio combinations. The opaque lower cloud-top pressure is held constant at 850 mb.

Wielicki and Coakley (1981) examined the rms and bias errors in cloud-top pressure retrieval for single-level clouds. In their study, the instrument noise was assumed to be Gaussian with zero mean and a standard deviation of 0.22 $mWm^{-2}sr^{-1}cm$ for the HIRS 15-μm channels. It is anticipated that the instrument noise should be significantly lower (by more than a factor of 2) for the MODIS instrument. The VAS instrument, by comparison, has a much higher instrument noise of approximately 1.0 mWm^{-2} $sr^{-1}cm$.

The CO_2 slicing technique cannot measure the properties of clouds where the contrast of radiation from cloud-free and cloud-obscured observations is too small for reliable discrimination in the satellite

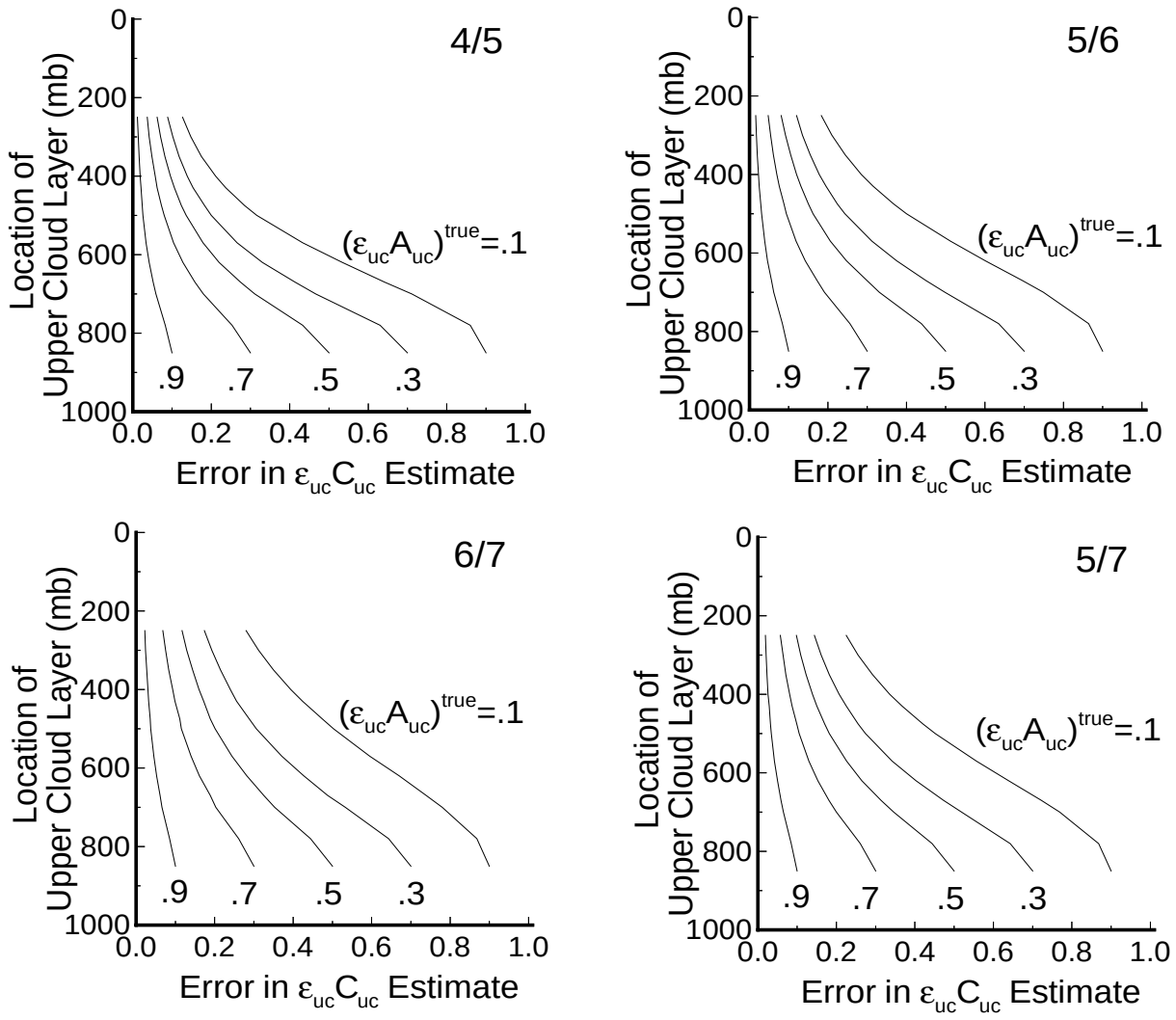

Figure 4.2-22. Upper-cloud effective cloud amount retrieval bias errors for several $\varepsilon_{uc}C_{uc}$ as a function of the pressure of the upper transmissive cloud layer. These results, derived from the pressure biases presented in Figure 4.2-21 are presented for the HIRS 4/5, 5/6, 6/7, and 5/7 channel ratio combinations. The opaque lower cloud-top pressure is held constant at 850 mb.

CO_2 spectral radiances. One could assign a threshold of perhaps 5 or 10 times the instrument noise as a threshold for further calculations, so that if the cloud signal falls below this threshold, the pixel is assumed clear (no clouds are retrievable). This threshold will not allow detection of very thin cirrus, such as subvisual cirrus, or low clouds below approximately 700 hPa.

4.2.4.7.5. Errors caused by uncertainties in temperature profiles and water vapor profiles. For single-level mid- to high-level clouds, the retrieval methods under study must first specify both clear-sky radiances, I_{cs}, and overcast black radiances, $I_{ob}(P_{cld})$, before cloud properties can be retrieved. Temperature errors affect the Planck functions *B(T)* and to a lesser extent the weighting functions *dt/d ln P*. Water vapor errors affect only the weighting functions *dt/d ln P*. Wielicki and Coakley (1981) evaluated errors caused by profile uncertainties by assuming the errors were Gaussian with zero mean. Errors were specified independently for each pressure level. Water vapor errors were specified as a percent of the correct mixing ratio at any level. Temperature error was found to dominate the retrieval error. Errors caused by uncertainties in temperature profiles and water vapor profiles dominated errors caused by instrument

noise for temperature rms errors of greater than or equal to 1.5 K for the HIRS 6/7 channel combination, for example. The errors were similar for all channel combinations. Retrieval errors were linearly proportional to temperature error and were inversely proportional to the cloud signal. For instrument noise, the lowest sounding channels (HIRS 6/7) give the smallest errors (Wielicki and Coakley, 1981).

4.2.4.8. Practical Considerations

4.2.4.8.1. Data dependencies of CO_2 slicing algorithm. The CO_2 slicing algorithm requires calibrated, navigated, co-registered radiances from the channels listed in Table 1. Navigation implies knowledge of the surface terrain, which will be available from other sources such as the Defense Mapping Agency's Digital Chart of the World. Characteristics required of the surface include surface elevation, land/water percentage, and vegetation type. These data sets are described more fully in section 4.1. The MODIS, GOES, or HIRS viewing angles must be known. The NMC global model estimates of surface temperature, pressure, and profiles of temperature and moisture will be used in the calculation of the upper cloud-top height and effective emittance.

4.2.4.9. Strategic Concerns

There are several concerns (or assumptions) in the CO_2 slicing cloud-retrieval method. First, the temperature and humidity estimates will be obtained from the NMC operational product on a fairly coarse horizontal grid (probably about 100 km) at fixed time intervals of 6 or 12 hours. Second, we assume that the frame is likely to have clouds with relatively stable cloud top altitudes, with at least some possibilities of seeing the ground nearby. Under these assumptions, both the clear-sky and cloudy-sky radiance profiles may be precomputed for each 1.25° grid cell once the temperature and humidity data are received and quality checked. This procedure may be performed for each of the potential channels and for the range of viewing zenith angles. If data are available from a simultaneous satellite swath of temperature and humidity retrievals, such as from AIRS/AMSU, then these computations could be performed at more frequent space and time points. Even with AIRS, the temperature and humidity points will be widely spaced with respect to the high-resolution imager data available for cloud retrieval.

We can list a number of sources of difficulty with this algorithm:

1. Temperature inversions induce an ambiguity in $p_{cld.}$
2. Height of cloud should not be far below the peak of the upper channel weighting function for the ratio method.
3. Algorithm does not work when signal/noise ratio becomes too small (a signal less than 10 times the signal noise is a reasonable initial estimate of this threshold).
4. Multichannel retrievals may not produce consistent values of p_{cld} or $\varepsilon_{cld}^{i} C$.
5. Multilevel clouds in a given FOV are not included in the assumptions of this method.
6. Presence of nonuniform cloud in FOV (e.g., some black clouds mixed with thin, low-emittance cloud) will cause ambiguities in p_{cld} and $\varepsilon_{cld}^{i} C$.
7. Algorithm assumes cloud is in a thin layer, so that the retrieval of cloud-top pressure is problematic for an optically thin cloud that has a large geometric thickness.
8. Instrument calibration errors cause some systematic shifts in cloud property retrievals.
9. Instrument spectral bandpass shifts will create errors.
10. Algorithm assumes that the emittances of clouds in any two closely spaced channels in the ratio method have nearly equal values.

11. Algorithm assumes clouds do not scatter in the IR.
12. Weighting functions depend on the input temperature and humidity profiles and upon the assumed mixing ratios of trace gases.
13. The accuracy of the retrieved cloud pressure depends on accuracy of the clear-sky radiance.

These potential error sources have been discussed in previous sections and, although it is important to understand and minimize them, they are generally well-known and accepted in the field of study. The implementation of the algorithm will have exception-handling logic to handle potential problems.

4.2.5. Other Strategies for Detection and Analysis of Multilayered Clouds

4.2.5.1. Overview

Most of the current validation studies being performed from FIRE, ASTEX, TOGA-COARE, etc. are mainly concerned with analyzing clouds that appear in a single layer. Unfortunately, the analysis of overlapping cloud layers remains largely unexplored. Surface observations and satellite imagery show that multilayered cloud systems are commonly found in frontal areas where cirrus overlaps altostratus or stratus cloud. A summary of 12 years (1965–1976) of ship-reported synoptic observations (Hahn et al., 1982), over the North Atlantic Ocean shows that cirrus clouds have a frequency of occurrence between 20% and 45%, depending on season and location. The frequency of stratus co-occurrence with cirrus is often greater than 50% between 30°N and 60°N, also depending upon season and location. In the same latitude band, the probability of finding cirrus over ocean with no other cloud present is usually less than 20%.These findings are supported by Tian and Curry (1989) in a study of cloud overlap statistics performed using Air Force three-dimensional nephanalysis during January 1979 over the North Atlantic Ocean. Given the relatively high probability of finding cirrus with other cloud types and the low probability of finding cirrus alone, we must develop methodologies to infer the vertical cloud structure prevalent over both land and oceans. This work has been initiated using data from the HIRS and AVHRR instruments aboard the National Oceanic and Atmospheric Administration (NOAA) operational satellite platforms (Kidwell 1991).

Another approach we will use for the Version 1 CERES cloud retrieval algorithm is to apply automated feature recognition techniques as described in Subsystem 4.1. Automated artificial intelligence techniques, principally the fuzzy logic cloud classifier, will be applied to the imager data to place the clouds in a larger context than would be gained from application of the algorithms described previously in this document. Another approach to classifying certain cloud types is provided by Phase II of the CLAVR algorithm. CLAVR-II will have some logic designed to type clouds as belonging to low stratus, thin cirrus, deep convective, or middle mixed. The middle mixed category is where cloud types will be placed that do not belong to the low stratus, thin cirrus, or deep convective categories. As new techniques are developed, they will be tested along with the other typing approaches to determine the strengths and weaknesses of each approach.

4.2.5.2. Midlatitude Multiple Layer Cloud Classification

Preliminary work has been initiated on classifying cloud scenes that contain overlapping cloud layers using a fuzzy logic classification system. Data used for the study (Baum et al. 1995) were taken from the First ISCCP Regional Experiment (FIRE) experiment held in Kansas during the fall of 1991. The daytime midlatitude scene classification system currently separates pixel subarrays into the following classes:

1. Water
2. Land
3. Low cloud

4. Mid-level cloud
5. High cloud
6. Multiple cloud layers

Snow is currently not included in this scheme. The training of the classifier was performed using 1-km resolution AVHRR data and has not been modified yet for the lower 4-km resolution GAC data. Future work will concentrate on developing the classification methodology for nighttime imagery, snow/ice covered surfaces and classification over desert regions. Present work concentrates on determining whether the broad cloud classes can be broken into more classes. For instance, we need to determine whether the low cloud class can be split into uniform stratus and stratocumulus classes; whether the mid-level cloud class may be split into altostratus and altocumulus classes, etc. It may also be useful to determine whether a cloud type is deeply convective or precipitating. The textural and spectral features used in Baum et al. (1995) for midlatitude cloud classification are shown in Table 4.1-2.

A description of the features may be found in Volume 4.1, section 4.1.3. This set of features was developed using data collected during the First ISCCP Regional Experiment held in Kansas in the fall of 1991. There was an extensive set of surface observations, rawinsondes, and other ancillary data to aid in scene analysis. This classification system has been applied to clouds embedded in air masses ranging from tropical to subpolar, but has yet to be modified and tested thoroughly to determine how robust the technique is for cloud layers occurring at other locations and during other seasons.

4.2.5.3. Determination of Cloud Height for Overlapping Cloud Layers

Imager pixels are identified as cloudy and clear as per Section 4.1. Uniform cloud layer properties such as temperature, pressure, and height are derived using such techniques as spatial coherence and CO_2 slicing. Imager data swath analysis occurs on several spatial scales. For example, the spatial coherence scheme discussed in Section 4.3 first operates on approximately a 250 km $\times$ 250 km scale, then on a smaller 50 km $\times$ 50 km scale. The HBTM scheme typically operates on groups of pixels on the 64 km $\times$ 64 km scale. The CO_2 slicing technique as used with the HIRS 15-μm data typically operates on each FOV, or about every 40 km (accounting for the distance between individual FOVs). In this section, we discuss a method to assign a cloud pressure for each of up to two cloud layers in each imager pixel from the analysis performed with these varying spatial scales.

When the cloud in an imager pixel is opaque, only one cloud layer is assigned to that pixel. The difficulties arise when cloud layers are transmissive, such as cirrus. Once the well-defined cloud layers have been identified using the methodologies outlined in the previous sections, the task is now to assign cloud pressures for the pixels that have more than one layer of cloud or in which the cloud layer is not opaque. Recall that textural classification occurs for 32×32 or 16×16 pixel arrays, and that the classification suggested by Stowe et al. (1991) operates on 2×2 arrays. In neither case is classification performed on the scale of an individual pixel. If, however, the classification procedures indicate the possibility of there being more than one cloud layer, each pixel within the classification subarray will be tagged as containing overlapping cloud layers. The upper and lower layer cloud-top pressures assigned to each pixel will be derived over a scale ranging from 40 km to 250 km, depending on the algorithm.

Baum et al. (1992) describe a multispectral, multiresolution (MSMR) methodology for analyzing collocated AVHRR and HIRS data. The CO_2 slicing technique called the ratio method (Smith and Platt 1978; Wielicki and Coakley 1981; Menzel et al. 1992) was applied to HIRS 15-μm radiometric data to infer mid- to high-level cirrus cloud pressure and effective emittances, εC. In a subsequent case study analysis of nighttime cirrus overlying a stratus layer over the mid-Atlantic Ocean, Baum et al. (1994) incorporated a spatial coherence technique (Coakley and Bretherton 1982; Coakley 1983) into the MSMR method for the retrieval of stratus cloud-top heights. Further detailed description of the CO_2 slicing and spatial coherence techniques are provided in sections 4.2.2 and 4.2.4 of this document.

Table 4.2-2. Spectral and Textural Features Chosen for Daytime Classification of NOAA-11 and NOAA-12 1-km Radiometric Data (Baum et al. 1995); Descriptions of Features are Provided in Text; for Channel 3, Further Specification is Made Between Measured Radiances (Converted to Brightness Temperature T_{B3}) and Reflectances (ρ_3) Determined by Subtracting Thermal Emission.

Feature	Type
Contrast ρ_1	Textural
Contrast ρ_2	Textural
Contrast T_{B3}	Textural
Contrast ρ_3	Textural
Homogeneity ρ_1	Textural
Mean ρ_3	Textural
Band difference $[\rho_1 - \rho_2]$	Spectral
Band difference $[T_{B3} - T_{B4}]$	Spectral
Band difference $[\rho_2 - \rho_3]$	Spectral
Ratio $[\rho_1/\rho_2]$	Spectral
Ratio $[T_{B3}/T_{B4}]$	Spectral
Ratio $[T_{B4}/T_{B5}]$	Spectral
Ratio $[\rho_1/T_{B4}]$	Spectral
Overlay $\{\rho_1, T_{B3}, T_{B4}]$	Spectral
Low ρ_3	Spectral
High ρ_3	Spectral
Spatial coherence ρ_2	Spectral
Spatial coherence T_{B4}	Spectral

A schematic of the MSMR processing method is shown in Figure 4.2-23. There are three input data streams consisting of satellite data, temperature and relative humidity profiles, and a global geomap as described in Subsystem 4.1, section 4.1.4.1. The geomap provides surface elevation and land/water percentage at 10-minute resolution (approximately 18 km in the midlatitudes). To reduce the remote sensing errors, two modules have been incorporated into the MSMR method. The first module provides meteorological analysis based upon rawinsonde data and/or gridded NMC model analyses. The second module is an automated cloud classification method. The cloud classification process provides additional insight as to whether one or more cloud layers are present in a 32×32 AVHRR array. For the multilayered cloud case study reported in Baum et al. (1995), the cloud heights calculated from application of the MSMR methodology agreed reasonably well with coincident lidar, radar, and aircraft data. For those 32×32 AVHRR arrays that are tagged as containing more than one cloud class, each of the pixels will be tagged as belonging possibly to an overlapping cloud layer. Further resolution of the degree or nature of the overlapping clouds will be resolved by comparing the measured radiances with theoretical calculations as outlined in Subsystem 4.3. This work is in its beginning stages, and much more progress is anticipated between now and the TRMM launch.

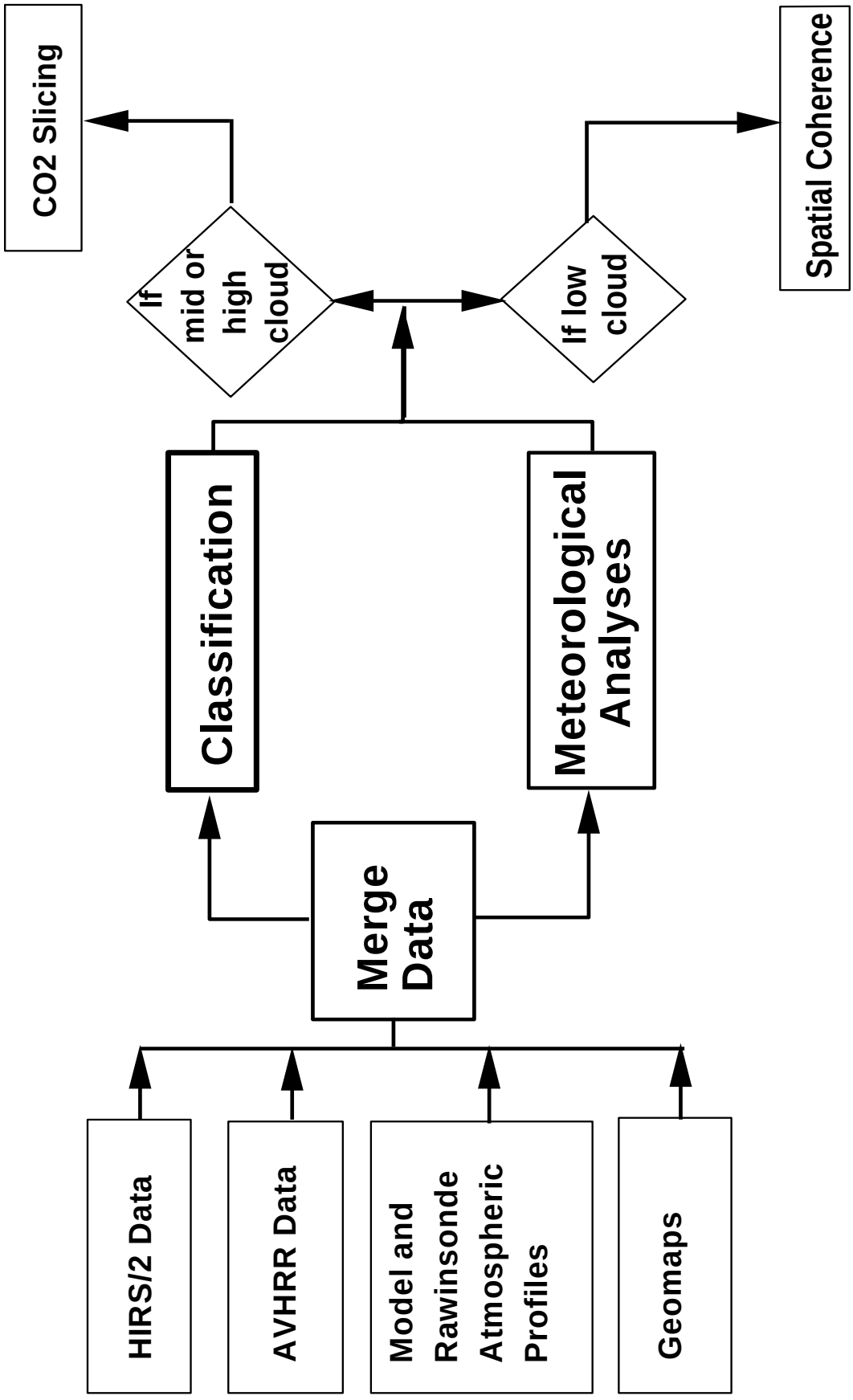

Figure 4.2-23. Schematic of MSMR method that provides framework for analysis of collocated AVHRR and HIRS data. The scheme has been developed to detect and analyze multiple cloud layers

Appendix

Analog Model for Pixel Clustering

The minimum number of points required in a peak of the $\rho(I)$ distribution for the set of points to be characterized as being clustered is established as follows. A Gaussian distribution is taken to be an example of a distribution that is sharply peaked and clearly nonuniform. The null hypothesis is that the points distributed according to a Gaussian distribution are indistinguishable from those distributed according to a uniform distribution. The interval over which the test is applied is divided into three equal parts. For a distribution of points to be classified as being nonuniform or highly concentrated, the number of points within the center interval must satisfy the condition given by

$$N > \frac{M}{3} + \sqrt{2M} \tag{A1}$$

where M is the number of points within the three intervals. In (A1), N is greater than three times the number of points that would be expected in the central interval were the points to be uniformly distributed over the three intervals. If the points are distributed according to a gaussian distribution so that the central interval spanned one standard deviation on either side of the mean and the outer intervals spanned an additional two standard deviations, then the above criteria would be satisfied when

$$erf(y) > \frac{1}{3} erf(3y) + \sqrt{\frac{2erf(3y)}{M}} \tag{A2}$$

where

$$y = \frac{1}{2\sqrt{2}} = 0.354 \tag{A3}$$

The condition is satisfied when $M > 18.03$. Thus, there must be ~20 pixels within three standard deviations on either side of a peak for the peak to satisfy the condition. If there are fewer pixels within the interval, then the number within one standard deviation of the mean, as given by a gaussian distribution, would not be more than three standard deviations above the number expected from a uniform distribution.

References

Arking, A.; and Childs, J. D. 1985: Retrieval of Cloud Cover Parameters From Multispectral Satellite Images. *J. Climat. & Appl. Meteorol.*, vol. 24, pp. 322–333.

Baum, B. A.; Uttal, T.; Poellot, M.; Ackerman, T. P.; Alvarez, J.; Intrieri, J.; Starr, D. O'C; Titlow, J.; Tovinkere, V.; and Clothiaux, E. 1995: Satellite Remote Sensing of Multiple Cloud Layers. *J. Atmos. Sci.*, vol. 52, no. 23, pp. 4210–4230.

Baum, Bryan A.; and Wielicki, Bruce A. 1994: Cirrus Cloud Retrieval Using Infrared Sounding Data —Multilevel Cloud Errors. *J. Appl. Meteorol.*, vol. 33, no. 1, pp. 107–117.

Baum, Bryan A.; Wielicki, Bruce A.; Minnis, Patrick; and Parker, Lindsay 1992: Cloud-Property Retrieval Using Merged HIRS and AVHRR Data. *J. Appl. Meteorol.*, vol. 31, pp. 351–369.

Chahine, M. T. 1974: Remote Sounding of Cloudy Atmospheres. I—The Single Cloud Layer. *J. Atmos. Sci.*, vol. 31, pp. 233–243.

Chang, Fu-Lung; and Coakley, James A., Jr. 1993: Estimating Errors in Fractional Cloud Cover Obtained With Infrared Threshold Methods. *J. Geophys. Res.*, vol. 98, no. D5, pp. 8825–8839.

Coakley, J. A., Jr.; and Bretherton, F. P. 1982: Cloud Cover From High-Resolution Scanner Data—Detecting and Allowing for Partially Filled Fields of View. *J. Geophys. Res.*, vol. 87, pp. 4917–4932.

Coakley, J. A., Jr. 1983: Properties of Multilayered Cloud Systems From Satellite Imagery. *J. Geophys. Res.*, vol. 88, pp. 10818–10828.

Coakley, J. A., Jr.; and Baldwin, D. G. 1984: Towards the Objective Analysis of Clouds From Satellite Imagery Data. *J. Climat. & Appl. Meteorol.*, vol. 23, pp. 1065–1099.

Debois, M.; Seze, G.; and Szejwach, G. 1982: Automatic Classification of Clouds on METEOSAT Imagery—Application to High-Level Clouds. *J. Appl. Meteorol.*, vol. 21, pp. 401–412.

Eyre, J. R. 1991: *A Fast Radiative Transfer Model for Satellite Sounding Systems*. ECMWF Tech. Memo. No. 176.

Eyre, Jonathan R.; and Menzel, W. Paul 1989: Retrieval of Cloud Parameters From Satellite Sounder Data—A Simulation Study. *J. Appl. Meteorol.*, vol. 28, pp. 267–275.

Eyre, Jonathan R.; and Woolf, Harold M. 1988: Transmittance of Atmospheric Gases in the Microwave Region—A Fast Model. *Appl. Opt.*, vol. 27, pp. 3244–3249.

Hahn, C. J. 1982: *Atlas of Simultaneous Occurrence of Different Cloud Types Over the Ocean*. NCAR Tech. Note TN-201.

Jacobowitz, Herbert 1971: Emission, Scattering and Absorption of Radiation in Cirrus Cloud Layers. Ph.D Thesis, Massachusetts Inst. Tech.

Kidwell, K. B. 1991: *NOAA Polar Orbiter Data Users Guide.* NOAA National Climatic Data Center, Satellite Data Services Div.

King, Michael D.; Kaufman, Yoram J.; Menzel, W. Paul; and Tanre, Didier D. 1992: Remote Sensing of Cloud, Aerosol, and Water Vapor Properties From the Moderate Resolution Imaging Spectrometer (MODIS). *IEEE Trans. Geosci. & Remote Sens.*, vol. 30, pp. 2–27.

Lin, X; and Coakley, J. A. 1993: Retrieval of Properties for Semitransparent Clouds From Multispectral Infrared Imagery Data. *J. Geophys. Res.*, vol. 98, pp. 18,501–18,514.

McCleese, D. J.; and Wilson, L. W. 1976: Cloud Top Heights From Temperature Sounding Instruments. *Q. J. R. Meteorol. Soc.*, vol. 102, pp. 781–790.

McCormick, M. P.; Winker, D. M.; Browell, E. V.; Coakley, J. A.; Gardner, C. S.; Hoff, R. M.; Kent, G. S.; Melfi, S. H.; Menzies, R. T.; and Platt, C. M. R. 1993: Scientific Investigations Planned for the Lidar In-Space Technology Experiment (LITE). *Bul. Am. Meteorol. Soc.*, vol. 74, no. 2, pp. 205–214.

McMillin, L. M.; and Fleming, H. E. 1976: Atmospheric Transmittance of an Absorbing Gas—A Computationally Fast and Accurate Transmittance Model for Absorbing Gases With Constant Mixing Ratios in Inhomogeneous Atmospheres. *Appl. Opt.*, vol. 15, pp. 358–363.

Menzel, W. P.; Smith, W. L.; and Stewart, T. R. 1983: Improved Cloud Motion Wind Vector and Altitude Assignment Using VAS. *J. Climat. Appl. Meteorl.*, vol. 22, pp. 377–384.

Menzel, W. P.; Wylie, D. P.; and Strabala, K. L. 1992: Seasonal and Diurnal Changes in Cirrus Clouds as Seen in Four Years of Observations With the VAS. *J. Appl. Meteorol.*, vol. 31, pp. 370–385.

Minnis, P.; and Harrison, E. F. 1984: Diurnal Variability of Regional Cloud and Clear-Sky Radiative Parameters Derived From GOES Data. Part I: Analysis Method. Part II: November 1978 Cloud Distributions. Parts I–III, *J. Climat. & Appl. Meteorol.*, vol. 23, pp. 993–1051.

Minnis, Patrick; Harrison, Edwin F.; and Gibson, Gary G. 1987: Cloud Cover Over the Equatorial Eastern Pacific Derived From July 1983 International Satellite Cloud Climatology Project Data Using a Hybrid Bispectral Threshold Method. *J. Geophys. Res.*, vol. 92, pp. 4051–4073.

Minnis, Patrick; Harrison, Edwin F.; and Heck, Patrick W. 1990: The 27-28 October 1986 FIRE IFO Cirrus Case Study—Cloud Parameter Fields Derived From Satellite Data. *Mon. Weather Rev.*, vol. 118, pp. 2426–2446.

Minnis, Patrick; Heck, Patrick W.; Young, David F.; Fairall, C. W.; and Snider, J. B. 1992: Stratocumulus Cloud Properties Derived From Simultaneous Satellite and Island-Based Instrumentation During FIRE. *J. Appl. Meteorol.*, vol. 31, pp. 317–339.

Minnis, Patrick; Liou, Kuo-Nan; and Takano, Yoshihide 1993: Inference of Cirrus Cloud Properties Using Satellite-Observed Visible and Infrared Radiances. I—Parameterization of Radiance Fields. *J. Atmos. Sci.*, vol. 50, no. 9, pp. 1279–1304.

Minnis, Patrick; Heck Patrick W.; and Young, David F. 1993: Inference of Cirrus Cloud Properties Using Satellite-Observed Visible and Infrared Radiances. II—Verification of Theoretical Cirrus Radiative Properties. *J. Atmos. Sci.*, vol. 50, no. 9, pp. 1305–1322.

Platt, C. M. R. 1983: On the Bispectral Method for Cloud Parameter Determination From Satellite VISSIR Data—Separating Broken and Semitransparent Cloud. *J. Climat. Appl. Meteorol.*, vol. 22, pp. 429–439.

Reynolds, D. W.; and Vonder Haar, T. H. 1977: A Bi-Spectral Method for Cloud Parameter Determination. *Mon. Weather Rev.*, vol. 105, pp. 446–457.

Rossow, W. B.; Mosher, F.; Kinsella, E.; Arking, A.; and Harrison, E. 1985: ISCCP Cloud Algorithm Intercomparison. *J. Climat. & Appl. Meteorol.*, vol. 24, pp. 877–903.

Rossow, William B.; and Garder, Leonid C. 1993: Cloud Detection Using Satellite Measurements of Infrared and Visible Radiances for ISCCP. *J. Climat.*, vol. 6, no. 12, pp. 2341–2369.

Shenk, W. E.; and Salomonson, V. V. 1972: A Simulation Study Exploring the Effects of Sensor Spatial Resolution on Estimates of Cloud Cover From Satellites. *J. Appl. Meteorol.*, vol. 11, pp. 214–220.

Smith, W. L.; and Platt, C. M. R. 1978: Comparison of Satellite-Deduced Cloud Heights With Indications From Radiosonde and Ground-Based Laser Measurements. *J. Appl. Meteorol.*, vol. 17, pp. 1796–1802.

Smith, W. L.; and Frey, R. 1990: On Cloud Altitude Determinations From High Resolution Interferometer Sounder (HIS) Observations. *J. Appl. Meteorol*., vol. 29, pp. 658–662.

Stowe, L. L.; McClain, E. P.; Carey, R.; Pellegrino, P.; and Gutman, G. G. 1991: Global Distribution of Cloud Cover Derived From NOAA/AVHRR Operational Satellite Data. *Adv. Space Res.*, vol. 11, no. 3, pp. 51–54.

Takano, Yoshihide; and Liou, Kuo-Nan 1989: Solar Radiative Transfer in Cirrus Clouds. I— Single-Scattering and Optical Properties of Hexagonal Ice Crystals. *J. Atmos. Sci.*, vol. 46, pp. 3–20.

Tian, Lin; and Curry, Judith A. 1989: Cloud Overlap Statistics. *J. Geophys. Res.*, vol. 94, pp. 9925–9935.

Weinreb, M. P. 1981: *Transmittances for the TIROS Operational Vertical Sounder*. NOAA Tech. Rep. No. NESS-85.

Wielicki, B. A.; and Coakley, J. A., Jr. 1981: Cloud Retrieval Using Infrared Sounder Data—Error Analysis. *J. Appl. Meteorol.*, vol. 20, pp. 157–169.

Wielicki, Bruce A.; and Parker, Lindsay 1992: On the Determination of Cloud Cover From Satellite Sensors—The Effect of Sensor Spatial Resolution. *J. Geophys. Res.*, vol. 97, no. D12, pp. 12799–12823.

Wyle, D. P.; and Menzel, W. P. 1989: Two Years of Cloud Cover Statistics Using VAS. *J. Climat.*, vol. 2, pp. 380–392.